



THÈSE de DOCTORAT
UNIVERSITÉ PIERRE ET MARIE CURIE (PARIS VI)
Spécialité : **Mécanique**

présentée par
Zhen JIAN

pour obtenir le grade de
DOCTEUR de l'UNIVERSITÉ PIERRE ET MARIE CURIE

Sujet de thèse :
Drop impact on solid:
Splashing transition and effect of the surrounding gas

Soutenance effectuée le 16 juin 2014 devant le jury composé de:

Laurent LIMAT

Stéphane VINCENT

Jie LI

José BICO

José-Maria FULLANA

Christophe JOSSERAND

Stéphane ZALESKI

Pascal RAY

Rapporteur

Rapporteur

Examineur

Examineur

Examineur

Directeur de Thèse

Co-directeur de Thèse

Co-directeur de Thèse

À mes chers parents

To my dear parents

致我最敬爱的父母

Acknowledgements

Je tiens tout d'abord à exprimer toute ma gratitude à Christophe Josserand, Stéphane Zaleski et Pascal Ray qui ont encadré mon travail. Au cours de ces années de recherche, ils m'ont non seulement guidé et conseillé, mais également soutenu moralement par leur amical enthousiasme. Je leur suis profondément reconnaissant pour m'avoir toujours fait confiance, tout en pardonnant et corrigeant mes erreurs.

Je remercie vivement les rapporteurs de cette thèse, Laurent Limat et Stéphane Vincent, pour leur lecture détaillée et nombreuses remarques et suggestions de ce manuscrit, de même que pour leur participation au Jury. Je remercie profondément Jie Li, José Bico et José-Maria Fullana qui m'ont fait l'honneur de participer au Jury de soutenance.

Il n'est de recherche scientifique sans échanges, je remercie tous ceux sans qui cette thèse ne serait pas ce qu'elle est : aussi bien par les discussions que j'ai eu la chance d'avoir avec eux, leurs suggestions ou contributions. Je pense ici en particulier à Stéphane Popinet, qui est le créateur du code Gerris avec lequel j'ai réalisé les travaux numériques; Gilou Agbaglah, qui m'a donné beaucoup de conseils au début de ma thèse; Guy-Jean Michon, qui m'a montré le monde expérimental et les résultats expérimentaux du chapitre de cette thèse traitant les impacts sur un liquide très visqueux sont le fruit de son talent et de sa gentillesse; Arnaud Antkowiak et Jérôme Hoepffner, j'ai suivi leurs cours de l'Ecoulements multiphasiques: dynamique des bulles et des gouttes, qui m'a renforcé les connaissances nécessaires pour mes travaux de recherche.

Je remercie chaleureusement Pierre-Yves Lagrée pour les échanges et pour son humour et sa gentillesse, qui est l'actuel directeur de l'équipe FCIH (Fluides Complexes et Instabilités Hydrodynamiques) au sein de laquelle j'ai effectué mes travaux de recherche; Simona Otarasanu, qui m'a encouragé et aidé avec toute sa patience, qui m'a permis

de faire cette thèse dans de bonnes conditions aussi bien matérielles que morales, et l'ensemble des membres de l'Institut Jean Le Rond D'Alembert, où j'ai été fort bien accueilli et entouré.

Je dois de très nombreux conseils aux autres doctorants et jeune chercheurs de l'Institut: Valentina Balbi, Cansu Ozhan, Raja Romani, Federico Bianco, Andrés Léon-Baldelli, Gounséti Paré, Julien Philippi, Marcello Meldi, Etienne Vergnault, Orestis Malaspinas, Xu Hui, Wang Xiaofei, Feng Yongliang, ... l'amicale solidarité qui a régné entre nous fut une aide inestimable.

Les réunions de l'équipe FCIH et du groupement DIGG (Development Informal Gerris Group) sont régulièrement ponctué cette thèse, me permettant ainsi de découvrir différents thèmes de recherche liés au mien, et de présenter mes travaux à une communauté critique, amicale et bienveillante. Je tiens à en remercier les organisateurs.

Je remercie profondément M. Pedro Pereira et Dr. Beatrice Bié qui m'ont soutenue moralement et qui ont pu m'apporter pour franchir les obstacles les plus difficiles durant ma thèse.

Je remercie chaudement mes amis: Dong Quan, Xu Da, Zhang Hui, Chen Chen, Shen Lili, Li Shaoyang, Lu Dabao, Wang Xinyu, Martin Saveski, Hana Susak, Viswanathan Arunachalam, Nazanin Firoozeh, Xu Feng, Chen Li, ... qui m'ont donné un support continu pendant ma thèse à Paris. Un grand merci à Liu Tingting qui m'a soutenu moralement depuis toujours et qui n'est jamais ordinaire.

Enfin, les mots les plus simples étant les plus forts, je ne saurais suffisamment remercier ma famille, et en particulier mon père Benqiang et ma mère Lixin. Malgré mon éloignement depuis de (trop) nombreuses années, leur intelligence, leur confiance, leur soutien sans faille, leur tendresse, leurs enseignements, leur encouragement et leur amour me portent et me guident tous les jours. Merci pour avoir fait de moi ce que je suis aujourd'hui. Vous êtes toujours les meilleurs. Je vous aime ! Un merci particulier à ma cousine Chengcheng, tu as coloré ma vie !

$$(\mathbb{N} \times \mathbb{N})/\mathcal{R} \stackrel{E}{\sim} \lim_{n \rightarrow \infty} (1 + \frac{1}{n})^n \frac{PV}{RT}$$

$$\dot{a} = \sqrt{\frac{W_e \sigma}{\rho L}} \frac{nRT}{V} \frac{F}{a} \sqrt{\frac{1}{\epsilon_0 \mu_0}}$$

Contents

Introduction	10
1 Numerical methodology	25
1.1 Numerical schemes	28
1.1.1 Quadtree/Octree Adaptive Mesh Refinement (AMR)	28
1.1.2 Temporal discretisation	29
1.1.3 Spatial discretisation	31
1.1.4 Volume-of-Fluid (VOF) advection scheme	33
1.1.5 Balanced-force surface tension calculation	34
1.1.6 Height-function curvature calculation	36
1.1.7 Parallelisation	37
1.2 Nondimensionalization	38
1.3 Conclusion	41
2 Validation of the numerical method: meniscus case	43
2.1 Physical description	44
2.2 Results and discussions	47
2.2.1 Dynamics of the contact point	48
2.2.2 Equilibrium interface	50
2.3 Conclusion	53
3 Gas effect in drop impact on a solid substrate	55
3.1 Physical description	56

3.2	Convergence test: analysis of the gas layer	59
3.3	Early stage of the impact	69
3.3.1	Constant density ratio $r = 0.003$	70
3.3.2	Constant viscosity ratio $m = 0.037$ and $m = 0.07$	75
3.4	Frontier between impact outcomes	75
3.5	Conclusion	79
4	Aerodynamic splashing mechanism	81
4.1	Pre-contact dynamics	82
4.1.1	Lubrication approximation in the gas layer	82
4.1.2	Characteristic lengths in the gas layer	85
4.1.3	Ejection of the small jet	91
4.1.4	Lift-up of the small jet	95
4.2	Post-contact dynamics	96
4.2.1	Central bubble entrapment	97
4.2.2	Detachment of the thin liquid sheet	99
4.2.3	Gas entrainment around the contact line	100
4.3	An aerodynamic splashing mechanism	101
4.4	Other effects in the impact dynamics	103
4.4.1	Contact angle effect	103
4.4.1.1	Impact on a totally-nonwetable surface ($\theta = 180^\circ$)	104
4.4.1.2	Impact on a totally-wetable surface ($\theta = 0^\circ$)	105
4.4.1.3	Impact on a partially-wetable surface ($\theta = 30, 60, 120, 150^\circ$)	107
4.4.2	Gas compressibility effect	110
4.5	Conclusion	111
5	Drop impact on a highly-viscous liquid	113
5.1	Physical description	114
5.2	Numerical investigations	117
5.2.1	Wave-like period	118
5.2.2	Solidification period	121
5.2.3	Comparison with an impact on solid	124
5.3	Comparison with the experiments	127

5.4 Conclusion	131
Conclusion and perspectives	132
Appendix	136
Bibliography	142

Introduction

Multiphase flow is important on the planet. Many natural phenomena in our environment involve multiphase flows, rain, volcanic activities, fog, typhoons. Moreover, countless industrial processes deal with multiphase flows, combustion engines, blood flow in human beings, chemical industry [Brennen, 2005, Kolev, 2002].

A multiphase flow can be defined as any fluid flow consisting of more than one phase. A key character of multiphase flows is the presence of interfaces. An interface is a contact surface or a boundary between two phases. A value jump occurs on the interface for many chemical or physical properties, for example, the density, the viscosity. In fluid mechanics, the interface is generally considered as zero-thickness. The precise tracking of the interface is a challenge in academy.

The dynamics of interface is involved in a host of physical problems, such as drop impact. In fluid mechanics, drop impact refers to the physical process of a liquid drop impacting on a target media. The target media could be solid or liquid. Drop impact is present in a large number of technical applications and natural phenomena [Rein, 1993].

In an ink-jet printer, with an electronic charging and deflection system, a continuous ink-jet is broken into micro-droplets charged a controlled voltage, each drop is deflected depending on the variation of voltage, then the drop impacts on the moving paper [Heinzl and Hertz, 1985, Kamphoefner, 1972, Le, 1998] (see Figure 1(a)). From the 1990s, the principle of ink-jet printing is employed into other industrial applications, such as the fabrication of structured components, micro-electrical devices and high-precision electric circuits[Basaran *et al.*, 2013, Sirringhaus *et al.*, 2000]. It introduces a new path to low-cost productions with high precision. Besides, 3D printing is a hotspot of the society and

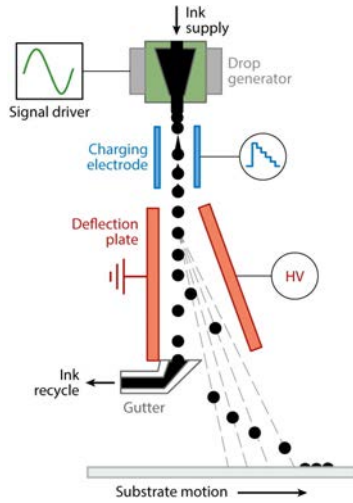
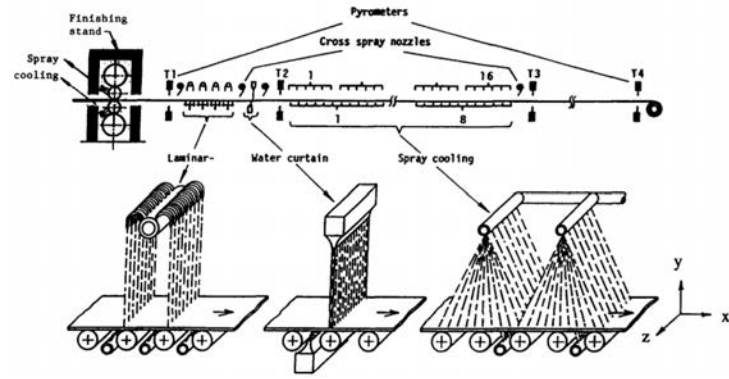
has been applied in many domains [Ho *et al.*, 2009, Nakamura *et al.*, 2008], a hamburger, components of an aircraft, even a house could be fabricated by 3D printings.

In steel and other metal productions, jet-and-spray cooling is employed in the rolling mill system [Chen and Tseng, 1992] and the process of annealing and quenching. Cold water drop-formed curtain or spray impacts on the hot steel to lower its temperature (see Figure 1(b)). Besides, jet spray is also used in cooling process for other hot surfaces, such as electronic devices. Dynamics of drop impact is also involved in surface coating, drying and cleaning. By controlling the outcomes of the drop impact on a target surface, the treated surface can obtain different physical or chemical properties.

In auto-mobile industries, fuel is first atomised then injected into the combustion chamber of gasoline engines [Zhao *et al.*, 1999] and direct-injection diesel engines [Yarin, 2006]. Drop impact is a key factor to understand the fuel atomisation process and the dynamics of micro fuel droplets in combustion chambers. The raindrop impact on the lampshade and the wind-shield is also studied in the vehicle designing engineering.

Besides industrial applications, drop impact is also present in a host of natural phenomena. The increase of the concentration of carbon dioxide in the atmosphere is considered as a principle cause of the global warming. Seas and oceans are also a principle container of the carbon dioxide apart from forests. Air entrainment due to drop impacts on water surfaces (lakes, rivers, seas and oceans) is a principle means of mass transfer between oceans and the atmosphere. Micro-drops, created by raindrops impacting on the ocean surfaces or by impacts between waves, capture air (carbon dioxide) from the atmosphere, keep the carbon dioxide in the ocean. Micro-drops could also evaporate and release the dissolved gas into the atmosphere (see Figure 1(c)). This dynamics is important to the global carbon dioxide equilibrium on the planet and is studied in meteorology and geography [Blanchard and Woodcock, 1957, Coantic, 1980, 1986].

Raindrop impact is also a primary force of soil erosion [Pp *et al.*, 1995]. Soil is transported by the micro-drops created by raindrop impact, it could have an important consequence in agriculture and in landform evolution on the planet. Study of drop impact on plant leaves is also crucial to improve the utilization ratio of liquid pesticides. The fantastic scenario of drop impact also attracts the general public and photographs of drop impact have become a sort of art [Edgerton, 1999].

(a) [Basaran *et al.*, 2013]

(b) [Chen and Tseng, 1992]



(c) photo from Wikipedia

Figure 1: Examples of drop impact. (a) Sketch of a model of the ink-jet printer with an electronic charging and deflection system [Basaran *et al.*, 2013]. (b) Sketch of a jet-and-spray cooling system used on the rolling mill in steel productions [Chen and Tseng, 1992]. (c) Droplet creation caused by impacts between waves, photo taken on Yeu Island by S. Veyrié.

Dynamics of drop impact has drawn attention of the academic research since more than a century. Experimental study can ascend to the end of the 19th century [Worthington, 1876a]. Worthington, a pioneer in drop impact research, did detailed studies on drop impact and solid ball impact on deep liquid pools, with different liquids and with solid

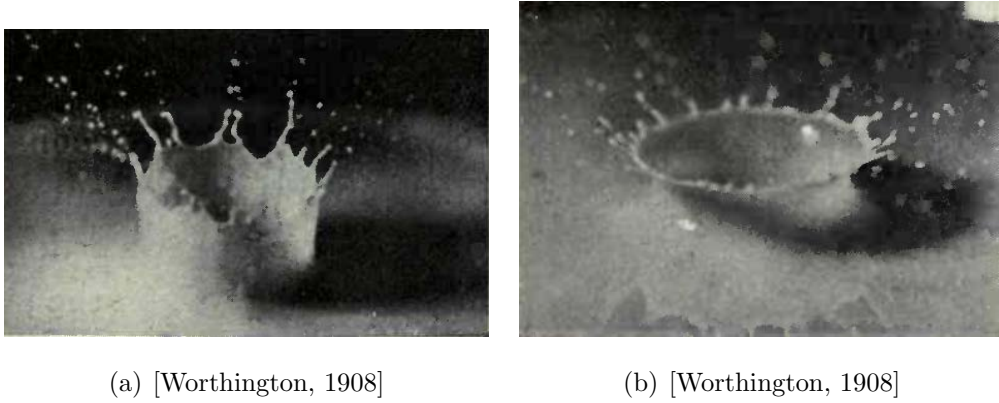


Figure 2: Photographs of Worthington’s splashes [Worthington, 1908]. (a) Water drop impacting onto a water mixed milk basin. (b) Rough surface solid sphere impacting onto a water mixed milk basin.

balls of different surface roughness [Worthington, 1876a,b, 1881, 1882, Worthington and Cole, 1899].

These systematic investigations were published in the book of Worthington [1908], a large number of fantastic illustrations from instantaneous photographs were included (see Figure 2). After impacting on a liquid basin, a corolla-like liquid structure is formed, fingering happens at the rim of the corolla and a crown is formed with some secondary droplets ejected from the end of the liquid fingers. This phenomenon is called a corona splash.

This delicate phenomenon keeps encouraging researchers to explore. However, even after a century of study, the mechanism of drop impact is far from a full comprehension. Referring to impacted objects, drop impacts can be divided into an impact on a solid substrate, on a thin liquid layer and on a deep liquid basin.

Presence of the solid substrate makes the dynamics complicated. Solid, liquid and gas are involved in this dynamics and the outcomes depend on properties of the three phases. Surface tension, surface roughness, surface wettability (contact angle); drop size, impact velocity, liquid density and viscosity; surrounding gas pressure, gas density and viscosity could influence the drop impact. Temperature, heat and mass transfer through the interface could also influence the impact outcome. The impact shows different outcomes on varying these parameters[Marengo *et al.*, 2011, Rioboo *et al.*, 2001].

There is a wide diversity of impact outcomes, of which the denomination is recent and is not always well defined in the literature. Figure 3 shows a panorama of common

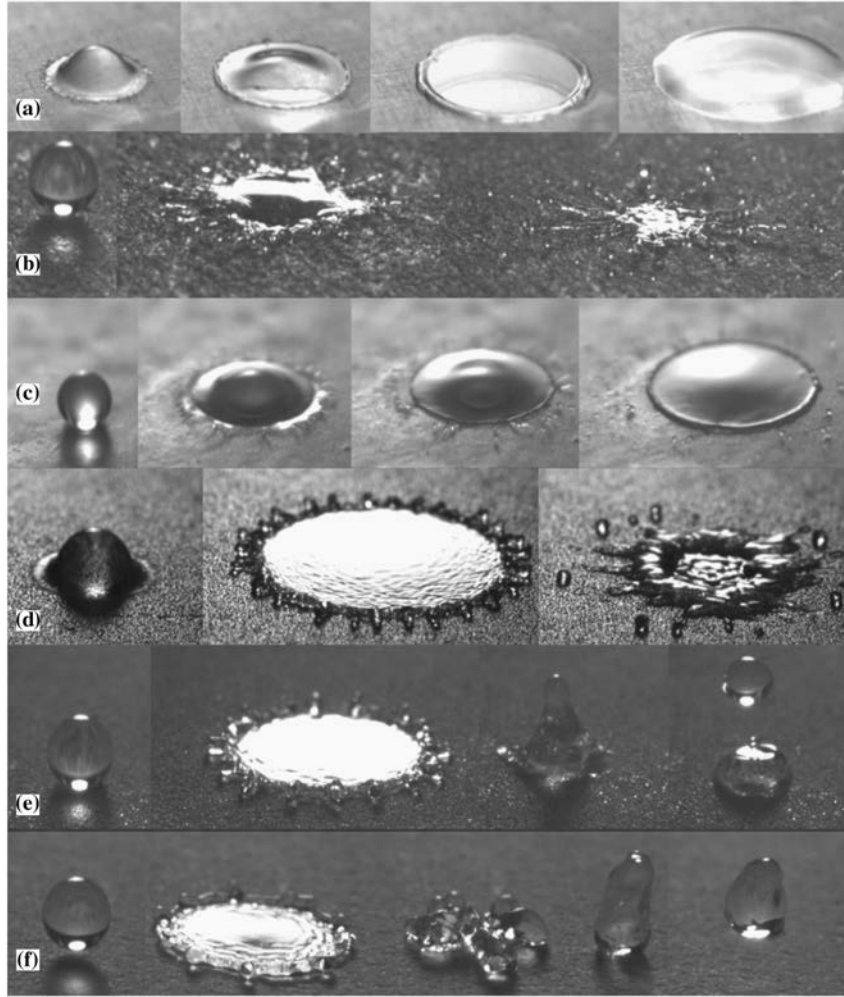


Figure 3: Outcomes of the drop impact [Marengo *et al.*, 2011]. (a) deposition; (b) prompt splash; (c) corona splash; (d) receding breakup; (e) partial rebound; (f) rebound.

impact outcomes proposed by Marengo *et al.* [2011]. With a small impact velocity, the drop spreads on the substrate and forms a pancake-like liquid sheet, namely a deposition. Impact can be violent, the drop is broken into small droplets immediately after the impact and the rest of the drop has an irregular form, namely a prompt splash. Impact can be “gentle”, a thin liquid sheet is ejected and forms a corolla. At the rim of the corolla, liquid fingers are formed and secondary droplets can be ejected from the fingers, namely a corona splash. During the receding process of the impacted drop, the drop can be broken into pieces, namely a receding breakup; or a jet is formed, then a secondary droplet is ejected from the rim of the jet and the rest of the primary drop remains on the substrate, namely a partial rebound; or the entire drop separates from the substrate and moves

towards the opposite direction of the impact, namely a rebound. Although some of these outcomes appear similar to the outcomes of an impact on liquid, the dynamics could be different.

A host of studies have been done on the corona splash. Experiments observed a thin liquid sheet ejection at the early stage of the impact and the sheet ejection is often considered as the origin of a splash [Deegan *et al.*, 2008, Lesser and Field, 1983, Thoroddsen, 2002]. Although the gas interaction during drop impact has been discovered since a long time [Esmailzadeh and Mesler, 1986], the surrounding gas has been normally neglected in the splash mechanism since the density and viscosity ratios between liquid and gas are large. However, some striking results have been recently reported.

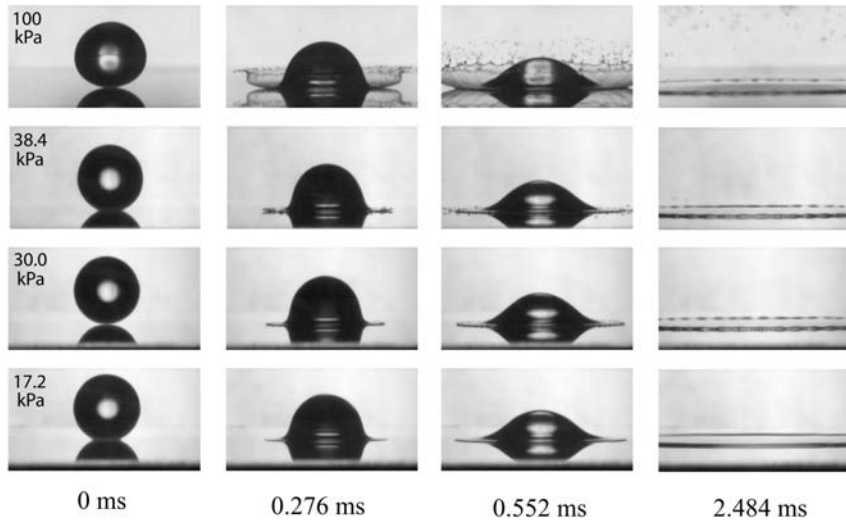


Figure 4: Photographs of an alcohol drop impacting on a smooth dry glass substrate [Xu *et al.*, 2005]. The diameter of drop is $3.4 \pm 0.1 \text{ mm}$ and the impact velocity is $3.74 \pm 0.02 \text{ m/s}$, the surrounding gas pressure varies from an atmospheric pressure (100 kPa) for the top row to one sixth of an atmospheric pressure (17.2 kPa) for the bottom row. In the fourth row, the splash is completely suppressed.

As shown in Figure 4, Xu *et al.* [2005] executed experiments of liquid drops impacting on a smooth dry substrate. The surprising result is that only by changing the surrounding gas pressure, the impact outcome can be completely changed from a splash at an atmospheric pressure to a deposition (a complete suppression of splash) at one sixth of an atmospheric pressure.

We should notice that in the experiments of Xu *et al.* [2005], the geometric length scale of the manipulation is much larger than the mean free path of air molecules, therefore, the gas dynamic viscosity does not vary with the gas pressure; they also measured a nearly constant surface tension. These striking results imply that the surrounding gas is also crucial in the splash formation, which makes the splash mechanism even more complicated.

Moreover, air bubbles were not observed in their experiments. Splashes are probably not related to the air entrapment. They proposed that the gas compressibility is responsible for the gas pressure effect in the impact dynamics. The formation of a splash is due to a competition between two stresses, Σ_G and Σ_L . Σ_G includes the gas pressure applied on the moving liquid sheet which tends to destabilize the rim of the sheet; Σ_L includes the liquid surface tension which tends to keep the liquid sheet intact. Because of a large velocity in the liquid sheet after impact and a small length scale of gas flow near the liquid sheet, they remarked that the gas compressibility should be considered in Σ_G and Σ_G will deflect the liquid sheet and form a splash. But the mechanism of the deflection and of the gas compressibility is not clearly described in their work.

Since the publication of these striking results, several models have been proposed to explain the gas effect, but there is still not a crystal clear understanding of the mechanism of the gas effect in the splash process. When a drop approaches a solid substrate, the gas cushioning effect becomes stronger. The length scale of the gas layer beneath the drop can become small enough as compared to the length scale of the radial axis. The Navier-Stokes equations can be simplified by the lubrication approximation. We should notice that inertial effects are completely neglected in the lubrication approximation, only the gas dynamic viscosity is involved. Whereas, in the experiments of Xu *et al.* [2005], the dynamic viscosity is constant which implies that the lubrication theory can not explain the suppression of splash caused by the gas pressure drop.

Mandre *et al.* [2009] proposed a gas compressibility mechanism. They argued that if the pressure in the gas layer beneath the drop becomes comparable to the ambient pressure before the drop deformation, the compressible effect in the gas layer becomes important. With absence of the surface tension, the interface close to the substrate develops a high curvature and an entrapped bubble is formed by this singularity. With presence of the

surface tension, the liquid does never contact the solid and the gas entrapped in the center becomes compressible.

Schroll *et al.* [2010] investigated the effect of the boundary layer and the vorticity variation caused by the no-slipping and no-flux condition on the solid surface. They considered both liquid and gas incompressible, ignored the gas influence by taking a small gas density. They argued that prior to impact, drop possesses an almost uniform vertical velocity field and the vorticity is nearly null in the entire drop. After impact, the impermeable solid makes the drop to form a radial flow along the solid. The no-slipping condition adjusts this radial flow and forms a viscous boundary layer. Vorticity is created in the liquid close to the solid. In the rapidly extending thin liquid sheet, the azimuthal component of the vorticity may separate the boundary layer from the solid and cause the thin sheet to lift away from the substrate.

Duchemin and Josserand [2011] proposed an aerodynamic instability mechanism. Under the incompressible assumption, they studied the curvature singularity of the interface. The liquid viscosity was neglected in their simulations. As drop approaches the substrate, a high curvature zone appears and a corner-like interface is created without the surface tension, a curvature singularity appears in the corner-like interface. This violent singularity could be a cause of splashing. The singularity can be regularized by the surface tension or the liquid viscosity. By considering the surface tension, they observed a thin liquid sheet ejected and extending along the solid surface with a high velocity, the sheet does not touch the substrate, so called jet-skating on a thin gas film.

Duchemin and Josserand [2012] studied the non-continuum effect in the splash formation. They argued that during the drop impact, the bubble entrapment is often observed and the characteristic length scale of the bubble is close to the gas mean free path, therefore, the non-continuum effect should be considered. The non-continuum effect usually happens for rarefied gases and it is related to compressible fluids. To distinguish the two effects, Duchemin and Josserand [2012] regarded the incompressible assumption and realised the non-continuum effect by imposing a Navier-slip boundary condition on the solid surface. They remarked that their model is valid in the regime of experiments of Xu *et al.* [2005] where the Knudsen number is high enough. They also argued that the non-continuum effect should not be a dominant factor in the splash mechanism.

Mandre and Brenner [2012] investigated both compressibility and non-continuum effects of the surrounding gas. They considered an incompressible inviscid liquid and an isothermal compressible gas beneath the drop. They pointed that the sheet ejection comes from a competition at the contact point between the liquid inertia and the surface tension. When the thin sheet spreads on the air layer, it is parallel to the substrate, there is no splash. A splash only happens after the contact with the solid surface where the sheet can be deflected by the solid-caused viscous force. Since they use a single-value model for the interface, it is impossible to produce the jet and to get a direct observation of the jet formation dynamics.

Besides numerical and theoretical works, experimental investigations are also active.

Air entrapment is studied by Thoroddsen [Thoroddsen *et al.*, 2008, 2003, 2005, 2009]. The air entrapment is observed in drop impacts on liquid and also on solid. Thoroddsen *et al.* [2005] investigated the air bubble entrapped under a drop impacting on a solid surface and the effect of the liquid viscosity on air entrapment. Thoroddsen *et al.* [2009] further investigated the dewetting caused by the air entrapment and argued that capillary waves propagating on the top surface of the drop may cause the merging of air bubbles and dewet the center of the lamella. Mehdi-Nejad *et al.* [2003] made numerical investigations on the air bubble entrapment phenomenon in non-splash cases with different liquids. They argued that the air entrapment could be a cause of the splashing in a liquid/solid impact.

Driscoll *et al.* [2010] studied impacts of relatively high-viscosity liquid drops and reported that the dynamics could be strikingly different comparing to low-viscosity liquid drops observed by Xu *et al.* [2005]. For low-viscosity liquids, Xu *et al.* [2005] proposed that the compressibility of the surrounding gas is important for the formation of a splash and the gas compressibility effect becomes strong around the impact moment, which seems to be confirmed by the experimental data. Whereas, in the high-viscosity splashing regime, the compressibility effect is probably not relevant to the splash. For low-viscosity liquids, the splash (the ejection of a thin liquid sheet) occurs immediately after the drop impact, however, for high-viscosity liquids, the drop will extend smoothly on the substrate for a while then a splash suddenly happens and the angle of the ejection direction is much smaller than low-viscosity liquids (see Figure 5 (a)). They confirmed that the ejection of a thin liquid sheet is the precursor to the splash. For high-viscosity liquids, a central entrapped bubble is also observed but the ejection of thin sheet occurs long after the

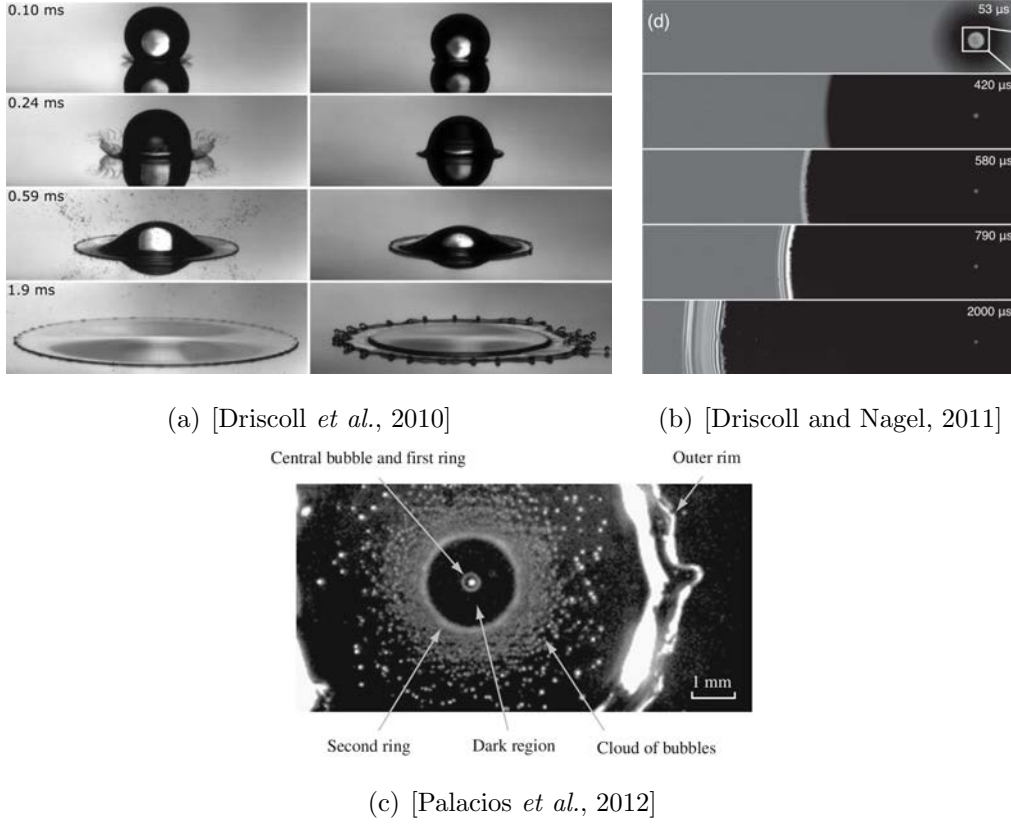


Figure 5: (a) Outcomes of a low- and a high-viscosity silicone oil drop impacting on a dry smooth substrate [Driscoll *et al.*, 2010]. The kinematic viscosity of the left column is 1 cSt , which is close to that of water at ambient temperature; the kinematic viscosity of the right column is 10 cSt . For a high-viscosity liquid, splash occurs much later with a much smaller ejection angle. (b) Sequences of photographs of a viscous liquid drop impact [Driscoll and Nagel, 2011]. The bright spot in the middle at right is the central entrapped bubble. The ejection of liquid sheet occurs in the third panel and is far from the central bubble. (c) Photograph of a spreading drop. Two bubble-rings and a cloud of bubbles are identified by Palacios *et al.* [2012].

collapse of the central bubble, which implies the bubble entrapment is not directly relevant to the splash. Driscoll and Nagel [2011] reported that for a highly-viscous liquid the splash can also be suppressed by lowering the surrounding gas pressure. No significant air layer persists to the splash moment and the drop has already a direct contact with the substrate before the ejection of the thin sheet (see Figure 5 (b)). The gas flow close to the rim of the spreading lamella should be responsible for destabilizing the thin sheet and forming a splash.

Palacios *et al.* [2012] (and Palacios *et al.* [2013]) studied viscous drops impacting on dry smooth surfaces and discovered a ring of micro-bubbles surrounding the central entrapped bubble, a cloud of bubbles and a second ring at the inner limit of the cloud bubbles (see Figure 5 (c)). They investigated the gas entrainment caused by local contacts of the liquid sheet and proposed that the second ring might cause the detachment of the thin film at the early stage of the impact.

With a coupled total internal reflection (TIR) microscopy [Rubinstein *et al.*, 2004] and a novel virtual frame technique (VFT), Kolinski *et al.* [2012] obtained a high resolution in time (it can be 6 ns with ideal conditions) and got the first direct observation of the thin gas layer between the impacting drop and the substrate. They demonstrated that at the very early stage of an impact, the drop skates on a gas layer, but the thin gas layer will become unstable and break into discrete locations which will result to a full wetting of the substrate subsequently. As the impact velocity increases, the thickness and the radial size of the gas layer decrease, but they confirmed the existence of the gas layer even with a high impact velocity in their experimental range.

Thanks to the development of high speed cameras with high resolution, more and more details of the drop impact have been discovered. A better understanding of the splashing mechanism is achieved, however, even the state-of-art high-speed visualization equipment is not able to observe the initial stage of an impact which is crucial to understand the splash formation. The theoretical and numerical methods are indispensable in the study of the drop splashing dynamics.

This Thesis

Motivated by the experimental results of Xu *et al.* [2005], in this thesis, under incompressible assumption, we investigate the drop impact dynamics by direct numerical simulations and try to understand the splashing mechanism, especially the effect of the surrounding gas.

The objectives of this work were the following:

- Validation of the numerical methods used in the code GERRIS.
- Study on the detailed dynamics occurred during the drop impacting on solid by the direct numerical simulations.
- Investigation on the effect of the surrounding gas in the drop impact dynamics, for instance, the inertial and viscous effects.
- Investigation on the contact angle effect in drop impacts.
- Validation of the incompressible assumption in drop impacts and the influence of the gas compressibility effect.
- Modelling of the drop impact on a highly-viscous liquid.
- Numerical and experimental studies on liquid/highly-viscous-liquid impacts and comprehension of the connection between liquid/solid impacts and liquid/liquid impacts.

The manuscript organisation of this thesis is structured as below:

Chapter §1 of the thesis provides a brief introduction of the numerical schemes used in the code GERRIS and the nondimensionalization process in GERRIS is then introduced with an example of the drop impact.

Chapter §2 presents a classical interface issue - the meniscus on a vertical wall in order to validate the numerical schemes used in the code GERRIS. The imposition of a contact angle at the beginning of the simulation introduces a perturbation to the system and a capillary wave is generated by the oscillation of the contact point. The dynamics of the

oscillation is studied and the profile of the equilibrium interface calculated by GERRIS is compared with the analytical solution.

Chapter §3 investigates the gas influence in the dynamics of the drop impact onto a solid substrate under the incompressible assumption. Complex dynamics occurs in the gas layer during the impacting process, the impact outcome differs with different gas properties. Two different splash mechanisms are identified. The drop can first contact the substrate and eject a fast moving liquid sheet, then the sheet is detached from the substrate and forms a “detachment-splash”; Otherwise, a small jet is formed before the contact with the substrate, then the jet is deflected and forms a “jet-splash”, the contact with the substrate occurs before or after the jet deflection. A curved transition frontier between non-splash and splash and a curved transition frontier between detachment-splash and jet-splash are found. The gas inertial effect is not negligible in the splashing mechanism.

In Chapter §4, dynamics of the drop impact process before and after the direct contact with the substrate are systematically studied. According to our investigations, the gas compressibility effect is not crucial in the splashing mechanism. If we regard both the small jet and the thin liquid sheet as an ejecta, the splash originates from the creation and deflection of the ejecta at the very early stage of the impact. An aerodynamic splashing mechanism is proposed to explain the two splashing mechanisms - “detachment-splash” and “jet-splash”. The influence of the contact angle on the impact dynamics is also investigated, a hydrophilic contact angles can eliminate a splash, while a hydrophobic contact angle can promote a splash.

Chapter §5 studies the dynamics of a normal-liquid droplet impacting on a highly-viscous liquid basin. A theoretical model is proposed to deal with the three-phase impacting dynamics. Viscous effect is dominant as compared to inertial and surface-tension effects. By increasing the viscosity of the liquid basin, two regimes are identified: a wave-like regime, where the splash is eliminated and a wave-like interface is formed; a solidification regime, where the splash is formed again and the interface of the basin remains at the initial position and performs as a solid substrate. Experiments of an ethanol drop impacting on a highly-viscous liquid (honey) basin are also presented. The honey basin performed as a solid and the complete suppression of the splash was observed by decreas-

ing the gas pressure as reported for impacts on solid. Comparison between photographs of experiments with snapshots of numerical simulations are demonstrated.

Chapter 1

Numerical methodology

Contents

1.1	Numerical schemes	28
1.1.1	Quadtree/Octree Adaptive Mesh Refinement (AMR)	28
1.1.2	Temporal discretisation	29
1.1.3	Spatial discretisation	31
1.1.4	Volume-of-Fluid (VOF) advection scheme	33
1.1.5	Balanced-force surface tension calculation	34
1.1.6	Height-function curvature calculation	36
1.1.7	Parallelisation	37
1.2	Nondimensionalization	38
1.3	Conclusion	41

Computational Fluid Dynamics (CFD) is an active branch of the fluid mechanics. It studies fluid flows and their effects by solving equations with numerical methods. It has become a powerful and crucial tool in all the researches related to the fluid mechanics. It allows an access to the instantaneous physical details of the fluid flow (such as velocity, pressure and concentration) with a significantly low cost comparing to experiments, especially for cases where experiments become difficult, even impossible to realise.

According to the scale of the computing target, CFD numerical methods can be divided into three branches (Tao [2000]):

- Macro-scale methods. It is based on the continuous fluid assumption and a fundamental model is the Navier–Stokes equations (Ferziger and Perić [2002]).
- Meso-scale methods. It simulates the kinetics of particle-groups and obtains values of macro physical parameters by some averaging techniques. The Direct Simulation of Monte Carlo method (DSMC) (Alexander and Garcia [1997]) and the Lattice-Boltzmann Method (LBM) (Mohamad [2011]) are included.
- Micro-scale methods. It simulates the dynamics of molecules, atoms, etc. and calculates the macro physical parameters by the statistic method. The Molecular Dynamics simulation (MD) (Haile [1997]) is included.

The principle of a CFD numerical method can be listed as blow:

- Modelling of the physical problem and establishing the corresponding governing equations (such as a simplified or modified form of the Navier-Stokes equations and other necessary equations).
- Establishment of the physical geometry of the problem. The optimized computational area is defined as a compromise between the real computational cost and the physical precision.
- Definition of the initial and boundary conditions. A correct definition of conditions is essential to a CFD problem. The conditions generally consist of informations of velocity, pressure, temperature or concentration.
- Temporal and spatial discretisation of the computational area and the mesh generation. The spatial discretisation consists of the Finite Volume Method (FVM) (Versteeg and Malalasekera [2007]), the Finite Element Method (FEM) (Zienkiewicz *et al.* [2005]), the Finite Difference Method (FDM) (Smith [1985]), etc.
- Iterative process to solve the governing equations and convergence criteria. For a system of linear equations, Jacobi method, Gauss–Seidel method, Successive over-relaxation method (Tao [2001]) and the Krylov subspace method (Watkins [2007])

can be employed. A hierarchical discretization method - the Multi-grid method (Hackbusch [2003]) is an efficient iterative method and a large number of algorithms are inspired by this idea.

- Analysis and visualization of the simulation results to validate the CFD models and obtain the physical explanation from the mathematical numerical solutions.

Multiphase CFD problems are of great interest for the industry and the academy. Particularly, as a simple case of multiphase flows, the diphasic flow is widely studied. The diphasic flow can consist of a same fluid in two different phases, two different fluids in a same phase or two different fluids in two different phases. The precise tracking of the interface between two different phases remains difficult, which makes the establishment of an efficient numerical scheme for the diphasic flow a great challenge and also a highly active research subject.

In the literature, three types of efficient schemes are often reported:

- Front Tracking method: it uses a point-group called markers at the interface, where the interface reconstruction is done by connecting the markers with a curve (in two dimensions) or a surface element (in three dimensions) (Chern *et al.* [1986], Shyy *et al.* [1996], Tryggvason *et al.* [2001]).
- Level Set method: it uses a level function of which the level 0 is the interface, it provides a high-precision tracking of the interface but the local mass conservation needs to be carefully guaranteed (Granier *et al.* [1996], Osher and Fedkiw [2001], Osher and Sethian [1988]).
- Volume-of-Fluid method (VOF) : it reconstructs the interface from a volume-fraction occupied by one phase in a mesh cell, it has a good local mass conservation and the high-precision tracking of the interface can be achieved by a local mesh refinement (Gr  tar Tryggvason and Zaleski [2011], Gueyffier *et al.* [1999], Hirt and Nichols [1981]).

In this chapter, we are interested in different schemes such as VOF, CSF (Continuum Surface Force) and HF (Height-Function) used in a diphasic fluid simulation code called

GERRIS, which will be employed in the coming chapters. GERRIS is an Open Source, Free Software program (*The GERRIS Flow Solver* <http://gfs.sf.net>) and is generally a partial differential equation solver for fluid flows. It allows to solve the time-dependent incompressible variable-density flows by Euler, Stokes, Navier-Stokes equations or linear and non-linear shallow-water equations. GERRIS is based on the finite-volume discretisation, uses an adaptive quadtree (octree in three dimensions) mesh generation technique and tracks the interface by a Volume-of-Fluid/Piecewise Linear Interface Calculation method (VOF/PLIC¹) [Li, 1995] with an accurate surface tension calculation. It supports advected/diffused passive tracers to track physical variables. GERRIS supplies portable parallel computations via the MPI library and it has developed special modules for geographic (GfsRiver, GfsOcean) and electro-hydrodynamics (GfsElectroHydro) issues. GERRIS is written in C with an object-oriented style. It is created by Stéphane Popinet and is supported by National Institute of Water and Atmospheric research (NIWA) of New Zealand and Institute Jean Le Rond D'Alembert (DALEMBERT) of France.

1.1 Numerical schemes

The detail of the numerical schemes used in GERRIS is described in the articles of Popinet [2003, 2009]. Here, we just talk about the main idea of the numerical schemes.

1.1.1 Quadtree/Octree Adaptive Mesh Refinement (AMR)

GERRIS employs a hierarchical adaptive mesh refinement through a fully-threaded tree structure. The adaptation process has two strategies: The first strategy is the refining process. Only small cells which satisfy a user-defined criterion will be refined. Several criteria can be introduced such as the adaptation of the gradient or a defined function for a variable. The second strategy is the coarsening process. After each refinement, all cells will be checked. If a cell does not satisfy the refinement criterion (it is over-refined), the cell will be coarsened.

Then, values of variables in the cell center will be updated. For parent cells, values are calculated by the mass-volumetric average of the children cells in order to make a good local conservation of physical variables (velocity for instance). For children cells, values

¹CIAM in French.

are calculated by a linear interpolation from their parent cells, which ensures a good local conservation of velocity. A projection step is implemented to avoid the numerical oscillation of vorticity and guarantee the incompressible assumption. Besides, a fractional time-step is introduced to reduce the computing cost.

1.1.2 Temporal discretisation

The diphasic, variable-density Navier-Stokes equations for an incompressible flow with the surface tension can be written as:

$$\rho(\partial_t \mathbf{u} + \mathbf{u} \cdot \nabla \mathbf{u}) = -\nabla p + \nabla \cdot (2\mu \mathbb{D}) + \gamma \kappa \delta_s \mathbf{n} + \mathbf{F}_{ext} \quad (1.1)$$

$$\partial_t \rho + \nabla \cdot (\rho \mathbf{u}) = 0 \quad (1.2)$$

$$\nabla \cdot \mathbf{u} = 0 \quad (1.3)$$

where $\rho \equiv \rho(\mathbf{x}, t)$ is the fluid density, $\mathbf{u} = (u, v, w)$ the fluid velocity, p the pressure, $\mu \equiv \mu(\mathbf{x}, t)$ the fluid viscosity, \mathbb{D} the deformation tensor defined as $D_{ij} \equiv (\partial_i u_j + \partial_j u_i)/2$, γ the surface tension, κ the mean curvature of the interface and \mathbf{n} the normal vector to the interface. The distribution function δ_s is a delta function which insures the surface tension γ is only on the interface. The force \mathbf{F}_{ext} represents the external forces applied on the system (for example, the gravitational force $\rho \mathbf{g}$).

A volume-fraction $c(\mathbf{x}, t)$ is introduced and the density and viscosity of the system are defined as :

$$\rho(c) = c\rho_1 + (1 - c)\rho_2,$$

$$\mu(c) = c\mu_1 + (1 - c)\mu_2,$$

where ρ_1 , ρ_2 and μ_1 , μ_2 are the density and viscosity of the fluid 1 and the fluid 2 respectively.

A staggered temporal discretisation of the volume-fraction, the density and the pressure produces a formally second-order accurate temporal discretisation of equations (1.1-1.3) at step n :

$$\begin{aligned} \rho_{n+\frac{1}{2}} \left[\frac{\mathbf{u}_{n+1} - \mathbf{u}_n}{\Delta t} + \mathbf{u}_{n+\frac{1}{2}} \cdot \nabla \mathbf{u}_{n+\frac{1}{2}} \right] &= -\nabla p_{n+\frac{1}{2}} + \nabla \cdot \left[\mu_{n+\frac{1}{2}} (\mathbb{D}_n + \mathbb{D}_{n+1}) \right] \\ &+ (\gamma \kappa \delta_s \mathbf{n})_{n+\frac{1}{2}} + \mathbf{F}_{ext} \end{aligned} \quad (1.4)$$

$$\frac{c_{n+\frac{1}{2}} - c_{n-\frac{1}{2}}}{\Delta t} + \nabla \cdot (c_n \mathbf{u}_n) = 0 \quad (1.5)$$

$$\nabla \cdot \mathbf{u}_n = 0 \quad (1.6)$$

This system is simplified by introducing the velocity decomposition of Hodge[Schwarz, 1995]

$$\mathbf{u}_\star = \mathbf{u}_{n+1} + \frac{\Delta t}{\rho_{n+\frac{1}{2}}} \nabla p_{n+\frac{1}{2}} \quad (1.7)$$

with

$$\nabla \cdot \mathbf{u}_{n+1} = 0 \quad (1.8)$$

Then, the system (1.4-1.6) becomes [Chorin, 1969]

$$\rho_{n+\frac{1}{2}} \left[\frac{\mathbf{u}_\star - \mathbf{u}_n}{\Delta t} + \mathbf{u}_{n+\frac{1}{2}} \cdot \nabla \mathbf{u}_{n+\frac{1}{2}} \right] = \nabla \cdot \left[\mu_{n+\frac{1}{2}} (\mathbb{D}_n + \mathbb{D}_\star) \right] + (\gamma \kappa \delta_s \mathbf{n})_{n+\frac{1}{2}} + \mathbf{F}_{ext} \quad (1.9)$$

$$\frac{c_{n+\frac{1}{2}} - c_{n-\frac{1}{2}}}{\Delta t} + \nabla \cdot (c_n \mathbf{u}_n) = 0 \quad (1.10)$$

$$\mathbf{u}_{n+1} = \mathbf{u}_\star - \frac{\Delta t}{\rho_{n+\frac{1}{2}}} \nabla p_{n+\frac{1}{2}} \quad (1.11)$$

$$\nabla \cdot \mathbf{u}_{n+1} = 0 \quad (1.12)$$

which requires solving a Poisson equation

$$\nabla \cdot \left[\frac{\Delta t}{\rho_{n+\frac{1}{2}}} \nabla p_{n+\frac{1}{2}} \right] = \nabla \cdot \mathbf{u}_\star \quad (1.13)$$

Then, the discretised momentum equation (1.9) is reorganised as

$$\begin{aligned} \frac{\rho_{n+\frac{1}{2}}}{\Delta t} \mathbf{u}_\star - \nabla \cdot \left[\mu_{n+\frac{1}{2}} \mathbb{D}_\star \right] &= \nabla \cdot \left[\mu_{n+\frac{1}{2}} \mathbb{D}_n \right] + \rho_{n+\frac{1}{2}} \left[\frac{\mathbf{u}_n}{\Delta t} - \mathbf{u}_{n+\frac{1}{2}} \cdot \nabla \mathbf{u}_{n+\frac{1}{2}} \right] \\ &+ (\gamma \kappa \delta_s \mathbf{n})_{n+\frac{1}{2}} + \mathbf{F}_{ext} \end{aligned} \quad (1.14)$$

where the right-hand-side term depends only on the values at the step n and $n + 1/2$, which is a Helmholtz-type equation and is solved using a variant of the multilevel Poisson solver. The Crank–Nicholson discretisation [Crank and Nicolson, 1947] of the viscous terms is implemented and it is formally second-order accurate and unconditionally stable. The velocity advection term $\mathbf{u}_{n+\frac{1}{2}} \cdot \nabla \mathbf{u}_{n+\frac{1}{2}}$ is estimated by the Bell–Colella–Glaz second-order unsplit upwind scheme [Bell *et al.*, 1989] and this scheme is stable for a CFL number² smaller than 1.

1.1.3 Spatial discretisation

The computational area is discretised in an orthogonal way using square (cubic in three dimensions) finite-volume organised hierarchically by a tree-structure called quadtree in two dimensions (octree in three dimensions).

Each finite volume is defined as a cell. Each cell could be the parent of up to four children (eight in three dimensions). The cell level is defined by starting from zero for the root cell and by adding one each time when a group of four children is added. Each cell has a direct neighbour at the same level in each direction (four in two dimensions, six in three dimensions). Each of these neighbours is accessible through a cell face. A mixed cell is also defined which has two fluid phases or is cut by a solid boundary. An example of spatial discretisation and the corresponding tree-structure representation is given in Figure 1.1.

To simplify the calculations (for instance, the gradient and the flux calculation) at the cell boundaries, several constraints are introduced in GERRIS:

- The difference of level between direct-neighbour cells can not be bigger than 1;
- The difference of level between diagonal-neighbour cells can not be bigger than 1;
- All the cells directly neighbouring a mixed cell must be at the same level.

All the physical variables (for example velocity, pressure and passive tracers) are collocated in the cell center (square center in two dimensions and cube center in three di-

²The CFL condition proposed by Courant *et al.* [1928, 1967] is a necessary but not sufficient condition of stability for solving certain partial differential equations. It can be described that the dependent physical domain must be contained in the numerical domain in a certain time. The general form of the CFL condition for a n-dimensional problem can be expressed as $C = \Delta t \sum_{i=1}^n \frac{u_{x_i}}{\Delta x_i} \leq C_{max}$.

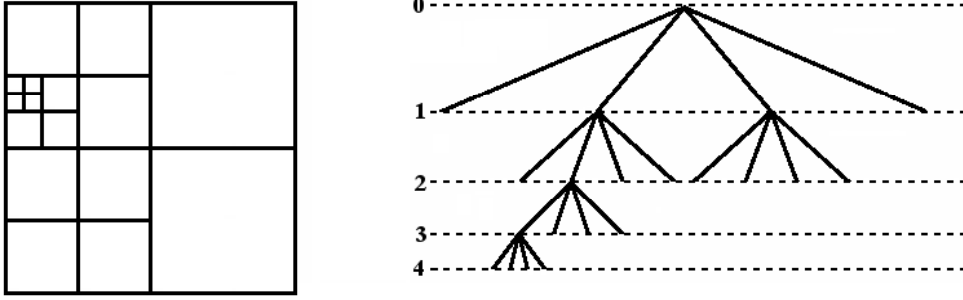


Figure 1.1: Example of two-dimensional quadtree spatial discretisation (left) and the corresponding tree-structure representation (right) [Popinet, 2003].

mensions) and they are interpreted as volume-averaged values in the corresponding finite volume. A collocated variable arrangement makes momentum conservation simpler on dealing with adaptive mesh. It also simplifies the implementation of the Crank–Nicholson discretisation of the viscous terms.

An approximate projection method of spatial discretisation [Almgren *et al.*, 2000] is implemented for the pressure correction equation (1.11) and the associated divergence in the Poisson equation (1.13) in order to avoid the classical decoupling between the pressure and velocity field caused by a collocated mesh.

At the first step, an auxiliary cell-centred velocity field \mathbf{u}_*^c is computed by equation (1.14). Then, an auxiliary face-centred velocity field \mathbf{u}_*^f is calculated by averaging the cell-centred values on all the faces of the orthogonal discretisation volumes. When the faces are on the boundary between different refinement levels of the quadtree (octree in three dimensions) mesh, an averaging process is performed to guarantee the consistency of the corresponding volume fluxes.

The divergence of the auxiliary velocity field of the right-hand-side of equation (1.13) is calculated for each control volume by a finite-volume approximation

$$\nabla \cdot \mathbf{u}_* = \frac{1}{\delta} \sum_f \mathbf{u}_*^f \cdot \mathbf{n}^f \quad (1.15)$$

where \mathbf{n}^f is the unit normal vector to the face and δ is the length scale of the control volume.

After solving equation (1.13), a pressure correction is applied to the face-centred auxiliary field

$$\mathbf{u}_{n+1}^f = \mathbf{u}_\star^f - \frac{\Delta t}{\rho_{n+\frac{1}{2}}^f} \nabla^f p_{n+\frac{1}{2}} \quad (1.16)$$

where ∇^f is a face-centred gradient operator and the resulting face-centred velocity field \mathbf{u}_{n+1}^f is non-divergent with its construction.

The cell-centred velocity field at time $n + 1$ is calculated by adding a cell-centred pressure correction

$$\mathbf{u}_{n+1}^c = \mathbf{u}_\star^c - \left| \frac{\Delta t}{\rho_{n+\frac{1}{2}}^f} \nabla^f p_{n+\frac{1}{2}} \right|^c \quad (1.17)$$

where the $|\cdot|^c$ operator denotes the average over all the faces delimiting the control volume.

The resulting cell-centred velocity field \mathbf{u}_{n+1}^c is approximately divergence-free with the above corrections.

1.1.4 Volume-of-Fluid (VOF) advection scheme

A piecewise linear Volume-of-Fluid (VOF) geometrical scheme based on quadtree (octree in three dimensions) spatial discretisation is used to solve the advection equation (1.10). The interface is reconstructed in each cell by a line (a plane in three dimensions) (see Figure 1.2) described by the equation

$$\mathbf{m} \cdot \mathbf{x} = \alpha \quad (1.18)$$

where \mathbf{m} is the local normal to the interface and \mathbf{x} is the position vector.

As \mathbf{m} and the local volume fraction c are known, α is determined by ensuring that the volume of fluid in the cell is equal to c . This volume can be calculated by considering the relative positioning of the line (the plane in three dimensions) in the cell which leads to the matched linear and quadratic (cubic in three dimensions) functions of α . A Mixed-Youngs-Centred (MYC) scheme [Aulisa *et al.*, 2007] is employed for interface normal estimation where a 3×3 ($3 \times 3 \times 3$ in three dimensions) regular Cartesian stencil is used.

Once the interface is reconstructed, the interface advection and geometrical flux need to be calculated. As shown in Figure 1.3, the total volume which will be fluxed to the right-hand neighbour in the cell C is delimited with a dashed line C_a and the fraction

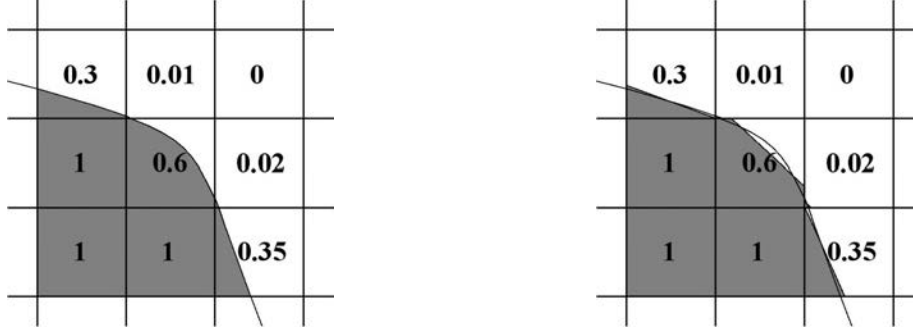


Figure 1.2: Left: Cells cut by the interface and its associated volume fraction field. Right: Reconstruction with piecewise linear interface [Agbaglah, 2011].

of this volume occupied by the phase 1 is indicated by the dark grey triangle. The area of this triangle is an estimation of the volume flux $\phi^{i+\frac{1}{2},j}$. For this advection, GERRIS uses a piecewise linear interface calculation scheme [Li, 1995], also known as least-square fit and split Lagrangian-Eulerian advection scheme [Scardovelli and Zaleski, 2003]. This geometrical approach is efficient and simple to implement with a Cartesian (or orthogonal) discretisation elements using a quadtree (octree in three dimensions) spatial discretisation.

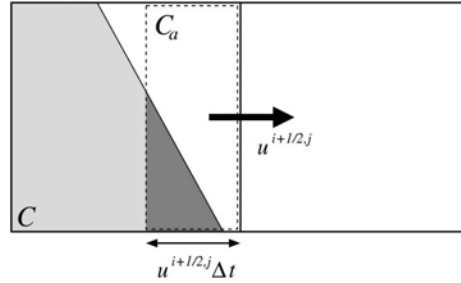


Figure 1.3: Geometrical flux estimation [Popinet, 2009].

A general form of this advection scheme with a quadtree (octree in three dimensions) discretisation is illustrated in Figure 1.4. In this case, cell C is a coarse cell, so the fluxes are computed independently for the top- (C^t) and bottom-halves (C^b). Once this is done, flux calculation in each half-cell is identical to the standard case (Figure 1.3).

1.1.5 Balanced-force surface tension calculation

To get an accurate estimation of the surface tension term $(\gamma \kappa \delta_s \mathbf{n})_{n+\frac{1}{2}}$ in the discretised momentum equation (1.9) is one of the most difficult part of a VOF method in surface-tension-driven flows. A Continuum-Surface-Force (CSF) approach [Brackbill

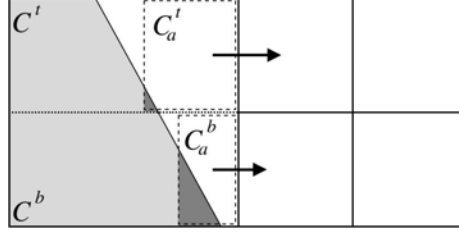


Figure 1.4: General case for geometrical flux computation on a quadtree discretisation [Popinet, 2009].

et al., 1992] for VOF method proposed an approximation as blow:

$$\gamma \kappa \delta_s \mathbf{n} \approx \gamma \kappa \nabla \tilde{c} \quad (1.19)$$

$$\kappa \approx \nabla \cdot \tilde{n} \quad \text{with} \quad \tilde{n} \equiv \frac{\nabla \tilde{c}}{|\nabla \tilde{c}|} \quad (1.20)$$

where ∇ is a finite difference operator, \tilde{c} is a spatially-filtered volume fraction field and $|\cdot|$ is a norm operator. Harvie *et al.* [2006], Lafaurie *et al.* [1994], Popinet and Zaleski [1999] reported that problematic parasitic currents are created by this approximation in the case of the theoretical equilibrium of a stationary droplet. To solve this problem, it is reported by Francois *et al.* [2006], Renardy and Renardy [2002] that in this case, the discretised momentum equation can be reduced to

$$-\nabla p_{n+\frac{1}{2}} + \gamma \kappa (\delta_s \mathbf{n})_{n+\frac{1}{2}} = 0 \quad (1.21)$$

with the CSF approximation, it can be expressed equivalently as

$$-\nabla p_{n+\frac{1}{2}} + \gamma \kappa (\nabla c)_{n+\frac{1}{2}} = 0 \quad (1.22)$$

If two conditions are satisfied:

- Discrete approximations of gradient operators in equation (1.22) are compatible;
- The estimated curvature κ is constant.

then the exact discrete equilibrium between surface tension and pressure gradient is regained by

$$p_{n+\frac{1}{2}} = \gamma \kappa c_{n+\frac{1}{2}} + \text{arbitrary constant} \quad (1.23)$$

Since GERRIS implements a collocated scheme, the gradient of cell-centred pressure is calculated by averaging the gradients of face-centred pressure as indicated in equation

(1.17). To satisfy the first condition, an implementation as below is executed before the projection steps:

first, the surface-tension force is applied to the auxiliary face-centred velocity field \mathbf{u}_*^f as

$$\mathbf{u}_*^f = \tilde{\mathbf{u}}_*^f + \frac{\Delta t \gamma \kappa_{n+\frac{1}{2}}^f}{\rho \left(c_{n+\frac{1}{2}}^f \right)} \nabla^f c_{n+\frac{1}{2}} \quad (1.24)$$

then the corresponding cell-centred surface-tension force is applied to \mathbf{u}_*^c as

$$\mathbf{u}_*^c = \tilde{\mathbf{u}}_*^c + \left| \frac{\Delta t \gamma \kappa_{n+\frac{1}{2}}^f}{\rho \left(c_{n+\frac{1}{2}}^f \right)} \nabla^f \right|^c c_{n+\frac{1}{2}} \quad (1.25)$$

1.1.6 Height-function curvature calculation

To satisfy the second condition, a high-accuracy Height-Function (HF) curvature calculation method is implemented in GERRIS. The standard HF scheme on two-dimension Cartesian grids can be listed in three steps:

1. Find a $3 \times N$ (or $N \times 3$) stencil centred on the cell to calculate the curvature. Here, the interface orientation is calculated in order to choose a stencil well aligned with the normal direction to the interface.

2. Sum the volume fractions in each column (or line) to obtain a discrete approximation of the interface height $y = h(x)$ (or $x = h(y)$).

3. Use finite difference approximation of the derivatives of the discretised height-function to compute the curvature

$$\kappa = \frac{h''}{(1 + h'^2)^{3/2}} \bigg|_{x=0 \text{ (ou } y=0)} \quad (1.26)$$

To calculate the curvature of under-resolved interfaces (of which the curvature radius becomes comparable to the mesh size), a parabola-fitted curvature algorithm is employed in GERRIS. In general, the interface can be fitted by a parabola (elliptic paraboloid in three dimensions) on minimising

$$\mathbb{F}(a_i) \equiv \sum_{i \leq j \leq n} [z'_j - f(a_i, x'_j)]^2 \quad (1.27)$$

with

$$f(a_i, x) \equiv \begin{cases} a_0 x^2 + a_1 x + a_2 & \text{in two dimensions} \\ a_0 x^2 + a_1 y^2 + a_2 xy + a_3 x + a_4 y + a_5 & \text{in three dimensions} \end{cases} \quad (1.28)$$

Then, from equation (1.26), the mean curvature κ can be estimated as

$$\kappa \equiv \begin{cases} \frac{2a_0}{(1+a_1^2)^{3/2}} & \text{in two dimensions} \\ 2 \cdot \frac{a_0(1+a_4^2) + a_1(1+a_3^2) - a_2a_3a_4}{(1+a_1^2+a_4^2)^{3/2}} & \text{in three dimensions} \end{cases} \quad (1.29)$$

1.1.7 Parallelisation

The increasing computing complexity and the great demand for massive high-performance computing have made the compatibility to parallel computation an indispensability for a modern CFD code, GERRIS provides a portable parallel support using the MPI library. It uses a MPI domain decomposition approach to synchronise at domain boundaries and a dynamic load-balancing technique to maintain a good parallel efficiency. A special visualisation tool - **GfsView** is developed to realise the parallel on-the-fly or offline visualisation. With an adaptive quadtree (octree in three dimensions) mesh, the parallelisation can be easily implemented in the square (cubic in three dimensions) cells or a group of cells in each level (see Figure 1.5).

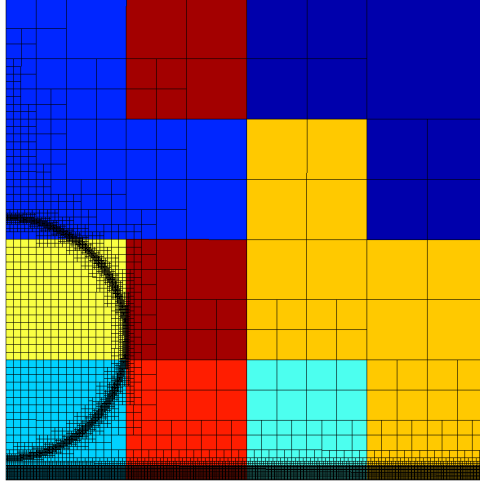


Figure 1.5: Example of parallelisation with the adaptive quadtree mesh in a drop impact case. Black lines shows the adaptive mesh arrangement. The interface and the zone close to the substrate are refined in a high level to obtain a high-precision computation of the interface and the gas dynamics above the substrate. Processors (indicated by different colours) are balanced according to the instant computing load.

1.2 Nondimensionalization

Dimensional analysis which introduces dimensionless numbers is often employed in fluid mechanics. In GERRIS, the only constraint of the unit system is coherence. Here, we introduce the nondimensionalization process with the drop impact process. If the only external force \mathbf{F}_{ext} is the gravitational force $\rho\mathbf{g}$, the Navier-Stokes equations (1.1) can be written as:

$$\rho \frac{d\mathbf{u}}{dt} = -\nabla p + \mu \Delta \mathbf{u} + \rho \mathbf{g} + \gamma \kappa \delta_s \mathbf{n} \quad (1.30)$$

A liquid drop of diameter D , density ρ_l and viscosity μ_l falls from a height h with an initial velocity U_0 and the gravity g , on a surface. The surrounding gas has a density ρ_g , a viscosity μ_g and a gas/liquid surface tension γ where the interface curvature is κ . The size of the computational area is L .

A symbol ‘*’ is superscribed on the nondimensionalized variables to distinguish from the original ones³.

We take the initial velocity U_0 , the liquid density ρ_l and a length scale \mathbb{X} ($\mathbb{X} = D$ or L for instance) as the characteristic quantities, yield:

$$\rho^* = \frac{\rho}{\rho_l}, u^* = \frac{u}{U_0}, D^* = \frac{D}{\mathbb{X}}, x^* = \frac{x}{\mathbb{X}}, t^* \simeq t \cdot \frac{U_0}{\mathbb{X}} = \frac{t}{\tau}, \kappa^* = \mathbb{X} \kappa$$

and for operators:

$$\frac{d}{dt} = \frac{d}{dt^*} \cdot \frac{dt^*}{dt} \sim \frac{1}{\tau} \frac{d}{dt^*}, \nabla \sim \frac{\partial}{\partial x} = \frac{\partial x^*}{\partial x} \cdot \frac{\partial}{\partial x^*} \sim \frac{1}{\mathbb{X}} \nabla^*, \Delta \sim \frac{\partial^2}{\partial x^2} = \frac{\partial}{\partial x} \left(\frac{\partial}{\partial x} \right) \sim \frac{1}{\mathbb{X}^2} \Delta^*$$

Considering the agreement of magnitude of unit between two sides of equation (1.30), the delta function δ_s should be to reduce a volume quantity into a surface one, then:

$$\delta_s \sim \frac{\partial}{\partial x} = \frac{1}{\mathbb{X}} \cdot \frac{\partial}{\partial x^*} \sim \frac{1}{\mathbb{X}} \delta_s^*$$

Substituting all formulas into equation (1.30), gives:

$$\rho^* \frac{du^*}{dt^*} = -\frac{1}{\rho_l U_0^2} \nabla^* p + \frac{\mu}{\rho_l U_0 \mathbb{X}} \cdot \Delta^* u^* + \rho^* \cdot \frac{\mathbb{X}}{U_0^2} g + \frac{\gamma}{\rho_l U_0^2 \mathbb{X}} \cdot \kappa^* \delta_s^* n \quad (1.31)$$

Comparing to the Navier-Stokes equations (1.30), if we define

$$g^* = \frac{\mathbb{X}}{U_0^2} g, p^* = \frac{p}{\rho_l U_0^2}$$

³For the convenience of readability, in the coming chapters, the superscript ‘*’ of dimensionless variables is dropped except special conventions.

and Reynolds number $Re = \rho_l U_0 \mathbb{X} / \mu_l$ and Weber number $We = \rho_l U_0^2 \mathbb{X} / \gamma$, the coefficient of the viscosity term can be written as :

$$\frac{\mu}{\rho_l U_0 \mathbb{X}} = \frac{1}{Re} \cdot \frac{\mu}{\mu_l} = \frac{1}{Re} \cdot \mu^{**} = \mu^*,$$

and the coefficient of the surface tension term:

$$\frac{\gamma}{\rho_l U_0^2 \mathbb{X}} = \frac{1}{We} = \gamma^*$$

Then we obtain the dimensionless Navier-Stokes equations:

$$\rho^* \frac{d\mathbf{u}^*}{dt^*} = -\nabla^* p^* + \frac{1}{Re} \cdot \mu^{**} \Delta^* \mathbf{u}^* + \rho^* \mathbf{g}^* + \frac{1}{We} \cdot \kappa^* \delta_s^* \mathbf{n} \quad (1.32)$$

where the nondimensionlized variables are shown in Table 1.1.

Table 1.1: U_0 -based dimensionless formulas

ρ^*	u^*	t^*	p^*	μ^*	g^*	γ^*	L^*	D^*
$\frac{\rho}{\rho_l}$	$\frac{u}{U_0}$	$\frac{U_0}{D} t$	$\frac{p}{\rho_l U_0^2}$	$\frac{1}{Re} \cdot \mu^{**}$	$\frac{\mathbb{X}}{U_0^2} g$	$\frac{1}{We}$	$\frac{L}{\mathbb{X}}$	$\frac{D}{\mathbb{X}}$

We can also nondimensionlize equation (1.30) by the gravity g instead of the initial velocity U_0 , then the dimensionless Navier-Stokes equations are:

$$\rho^* \frac{d\mathbf{u}^*}{dt^*} = -\nabla^* p^* + \frac{1}{Re} \cdot \mu^{**} \Delta^* \mathbf{u}^* + \rho^* + \frac{1}{We} \cdot \kappa^* \delta_s^* \mathbf{n} \quad (1.33)$$

where the nondimensionlized variables are shown in Table 1.2.

Table 1.2: g -based dimensionless formulas

ρ^*	u^*	t^*	p^*	μ^*	g^*	γ^*	L^*	D^*
$\frac{\rho}{\rho_l}$	$\frac{u}{\sqrt{g\mathbb{X}}}$	$\sqrt{\frac{g}{\mathbb{X}}} t$	$\frac{p}{\rho_l g \mathbb{X}}$	$\frac{1}{Re} \cdot \mu^{**}$	1	$\frac{1}{We}$	$\frac{L}{\mathbb{X}}$	$\frac{D}{\mathbb{X}}$

For a diphasic system, we introduce two dimensionless numbers:

(i) the density ratio r :

$$r = \frac{\rho_g}{\rho_l} \quad (1.34)$$

(ii) the viscosity ratio m :

$$m = \frac{\mu_g}{\mu_l} \quad (1.35)$$

Then the dimensionless density and viscosity are:

$$\rho^* = \begin{cases} 1 & \text{if } liquid \\ r & \text{if } gas \end{cases}, \quad \mu^{**} = \begin{cases} 1 & \text{if } liquid \\ m & \text{if } gas \end{cases}.$$

Now we can calculate all necessary dimensionless variables for a simulation. We take a water drop of diameter $D = 3 \text{ mm} = 3 \times 10^{-3} \text{ m}$ with an initial velocity of $U_0 = 3 \text{ m} \cdot \text{s}^{-1}$ and a gravity of $g = 9.8 \text{ m} \cdot \text{s}^{-2}$ as example. At the Standard Atmospheric Pressure (SAP $1.01325 \times 10^5 \text{ Pa}$) and the ambient temperature (20°C), physical properties of water and air are shown in Table 1.3:

Table 1.3: Physical properties of water and air

	density $\rho \text{ (kg} \cdot \text{m}^{-3})$	viscosity $\mu \text{ (Pa} \cdot \text{s)}$	surface tension $\gamma \text{ (N} \cdot \text{m}^{-1})$
water	998.2	1.002×10^{-3}	7.28×10^{-2}
air	1.204	1.983×10^{-5}	

With the formulas in Table 1.1, we obtain the dimensionless variables (see Table 1.4).

Table 1.4: U_0 -based nondimensionlization

ρ_l^*	ρ_g^*	γ^*	D^*
$\frac{\rho_l}{\rho_l} = 1$	$r \cdot \rho_l^* \approx 1.21 \times 10^{-3}$	$\frac{1}{We} \approx 2.70 \times 10^{-3}$	$\frac{D}{D} = 1$
μ_l^*	μ_g^*	U_0^*	g^*
$\frac{1}{Re} \approx 1.12 \times 10^{-4}$	$m \cdot \mu_l^* \approx 2.21 \times 10^{-6}$	$\frac{U_0}{U_0} = 1$	$\frac{D}{U_0^2} g \approx 3.27 \times 10^{-3}$

As shown in Table 1.4, the dimensionless gravity g^* is small as compared to U_0^* . If the initial position of the drop is close to the substrate, the variation of velocity due to the gravitational force is negligible since the velocity is large and the time before impact is small. Then, the gravity g^* can be neglected in simulations.

1.3 Conclusion

In this chapter, we first give a brief introduction of the numerical schemes used in the code GERRIS. GERRIS is in general a solver for incompressible multiphase flows, it provides solutions for Navier-Stokes-type equations and it has developed special modules for geographic (GfsRiver, GfsOcean) and electro-hydrodynamics (GfsElectroHydro) issues. A staggered temporal discretization is used and it ensures a formally second-order accuracy. The velocity is discretized by a Hodge decomposition and the pressure is calculated by solving a multi-level Poisson equation. A collocated finite-volume spatial discretization is employed with an orthogonal tree-structure mesh arrangement. As one of the highlights in GERRIS, the adaptive quadtree (octree) mesh ensures an efficient computation with a high precision and a low computing cost. The interface advection is calculated by a piecewise linear Volume-of-Fluid (VOF) geometrical scheme. A height-function scheme is used to calculate the curvature and a balanced-force scheme ensures an accurate computation of the surface tension. GERRIS also provides the parallel computation via MPI and has successful applications in clusters and supercomputers in practice. A visualisation tool - GfsView is developed to realise the on-the-fly or offline visualisation for serial or parallel computations.

In the second part, we introduce the nondimensionalization process in GERRIS with an example of the drop impact. Since GERRIS has a coherent unit system, all coherent unit-systems are acceptable which is a convenience for industrial computations.

Chapter 2

Validation of the numerical method: meniscus case

Contents

2.1	Physical description	44
2.2	Results and discussions	47
2.2.1	Dynamics of the contact point	48
2.2.2	Equilibrium interface	50
2.3	Conclusion	53

Meniscus is a common phenomenon which is present in wall-related dynamics such as drop impacts, surface coating processing. Rich physical factors are involved in this dynamics, surface tension, gravity, interface, triple-phase contact line and contact angle and an analytical solution exists for the profile of the equilibrium interface. The triple-phase contact line is the intersection of the fluid/fluid interface (usually gas/liquid) to the solid boundaries and the contact angle is the angle measured in the liquid, where a liquid/gas interface meets a solid surface.

In an equilibrium system (for example, a liquid drop at rest on a solid surface, see Figure 2.1), the contact line is stationary and forces come to a balance. Considering the force balance projected on the solid surface, projected capillary forces obeys the Young's

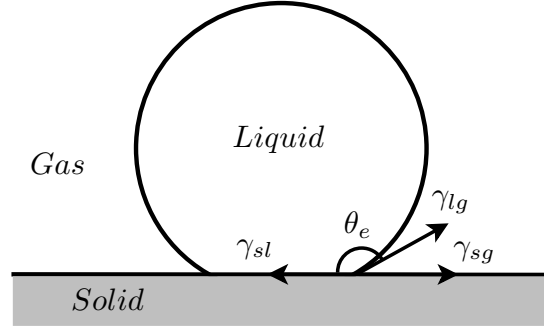


Figure 2.1: Typical triple-phase system - A sessile drop. A liquid drop is at rest on a solid surface with a surrounding gas. A triple-phase contact line (Two points in two dimensions and a circle in three dimensions) is present associated with a contact angle θ_e . γ_{lg} , γ_{sg} and γ_{sl} are capillary forces between different phases.

relation at the contact point:

$$\gamma_{lg} \cos \theta_e = \gamma_{sg} - \gamma_{sl} \quad (2.1)$$

where θ_e is the static contact angle, γ_{lg} , γ_{sg} and γ_{sl} are capillary forces by unity (surface tension) of the liquid-gas, solid-gas, solid-liquid interfaces at the contact point.

The static contact angle is a physical property of the triple-phase system and the Young's formula indicates the relation between contact angle and surface tension: $\cos \theta_e = (\gamma_{sg} - \gamma_{sl}) / \gamma_{lg}$.

In this chapter, we validate the numerical schemes used in GERRIS by the meniscus case. The dynamics of the contact point and the profile of the equilibrium interface are studied.

2.1 Physical description

The water surface is nearly flat in a cup of water; but if we look closely at the water area near the wall, the water surface appears a curved profile. The surface deformation is caused by capillary forces. This phenomenon of surface deformation is called a meniscus, which is a result of the equilibrium between capillary forces and the gravity.

For the meniscus on a vertical wall, we suppose the liquid surface is half-infinity large. The meniscus profile depends on the wettability of the wall. On a hydrophilic substrate, the surface ascends from the flat surface and forms a contact angle $\theta_e < 90^\circ$

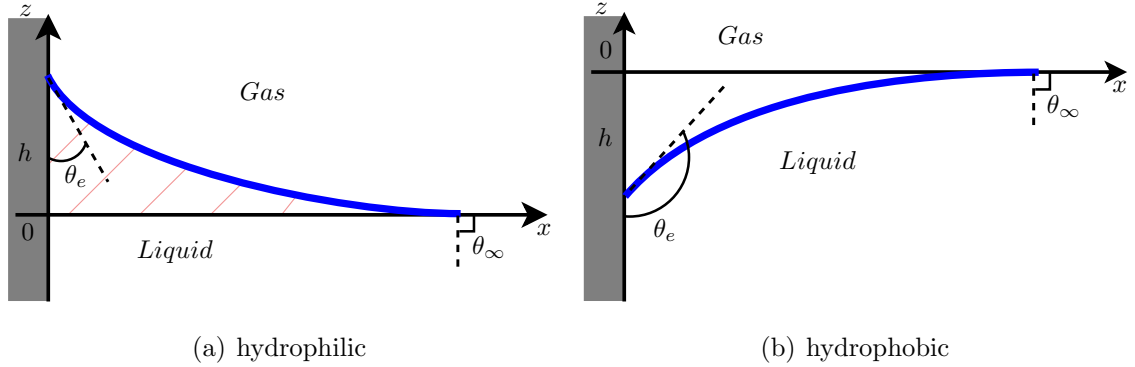


Figure 2.2: Meniscus on a vertical wall (a) in a hydrophilic case ($\theta_e < 90^\circ$) and (b) in a hydrophobic case ($\theta_e > 90^\circ$). The blue curve shows the equilibrium interface, h is the maximum height of interface, θ_e is the static contact angle. When x position is far away from the wall ($x \rightarrow +\infty$), meniscus will be eliminated and the interface returns flat ($\theta_\infty \rightarrow 90^\circ$).

(see Figure 2.2(a)); on a hydrophobic substrate, the surface descends and form a contact angle $\theta_e > 90^\circ$ (see Figure 2.2(b)).

To get the equilibrium interface profile, we study a point (x, z) on the interface (note $f = z(x)$). At the equilibrium state, the point (x, z) has a balance between the capillary force and the gravity.

Note the gas pressure at infinity is P_0 . At the point (x, z) , the liquid-side pressure caused by the gravity is $P_0 - \rho_l g z$ and the gas-side pressure caused by the surface tension is $P_0 - \gamma \kappa(z)$. The interface is at equilibrium, thus the pressures of two sides of the interface come to balance:

$$P_0 - \rho_l g z = P_0 - \gamma \kappa(z) \quad (2.2)$$

where P_0 is the gas pressure, ρ_l is the liquid density, g is the gravity, γ is the coefficient of surface tension and $\kappa(z)$ is the curvature at the point (x, z) .

Then, the interface $f = z(x)$ obeys:

$$z = l_c^2 \kappa(z) \quad (2.3)$$

where l_c is the capillary length:

$$l_c = \sqrt{\frac{\gamma}{\rho_l g}} \quad (2.4)$$

In Cartesian coordinates, the curvature $\kappa(z)$ can be calculated as:

$$\kappa(z) = -\frac{z''}{(1 + (z')^2)^{\frac{3}{2}}} \quad (2.5)$$

Substituting equation (2.5) into equation (2.3) gives:

$$z = -l_c^2 \frac{z''}{(1 + (z')^2)^{\frac{3}{2}}} \quad (2.6)$$

To solve the equation (2.6), we have two boundary conditions: on the wall ($x = 0$), z takes the maximum value h and when x -position is far away from the wall, the interface returns flat, z approaches 0:

$$\begin{cases} z = h, & x = 0 \\ z \rightarrow 0, & x \rightarrow +\infty \end{cases}$$

By integrating equation (2.6), we can obtain the profile of the equilibrium interface in an implicit form:

$$x = l_c \cdot \operatorname{acosh} \frac{2l_c}{z} - \sqrt{4l_c^2 - z^2} + x_0 \quad (2.7)$$

[De Gennes *et al.*, 2005].

The constant x_0 is obtained by the boundary condition $x = 0, z = h$:

$$x_0 = \sqrt{4l_c^2 - h^2} - l_c \cdot \operatorname{acosh} \frac{2l_c}{h} \quad (2.8)$$

To calculate the maximum height of the equilibrium interface h , we suppose the surface tension is uniform and continuous on the interface and consider the horizontal force balance in the liquid between the wall and the positive infinity (see the shaded part in Figure 2.2(a)). On the wall, the liquid bears the capillary force and the hydraulic force; At the positive infinity, there is only the capillary force. They are in balance :

$$\gamma \sin \theta_e + \int_0^h \rho g z \, dz = \gamma \quad (2.9)$$

Then, the maximum height of the equilibrium interface h :

$$h = \sqrt{2} l_c \sqrt{1 - \sin \theta_e} \quad (2.10)$$

Now the profile of the equilibrium interface is determined by equations (2.7),(2.8),(2.10).

2.2 Results and discussions

In the case of water and air, for a contact angle $\theta_e = 30^\circ$, the characteristic lengths of meniscus: the capillary length $l_c = \sqrt{\frac{\gamma}{\rho_l g}} \sim 3 \times 10^{-3} \text{ m}$ and the maximum height of the equilibrium interface $h = \sqrt{2}l_c\sqrt{1 - \sin\theta_e} \sim 3 \times 10^{-3} \text{ m}$. In general, the characteristic length of meniscus is of the order of 10^{-3} m for water and air.

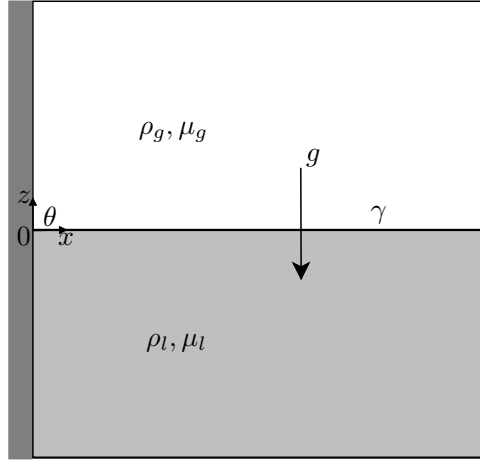


Figure 2.3: Calculation domain. A liquid of density ρ_l , viscosity μ_l and a gas of density ρ_g , viscosity μ_g form an initial horizontal interface with a surface tension γ . The gravity g applies in the whole domain. The left side is a solid wall and a contact angle θ_e will be imposed at the beginning of the simulation $t = 0$; a symmetry condition is applied on the right side. The interface is initially at $z = 0$.

As shown in Figure 2.3, to eliminate the boundary effect to the meniscus, we take a relatively large domain comparing to the order of magnitude of the characteristic meniscus length. The left side of the domain is a solid wall and a contact angle θ_e will be imposed at the beginning of the simulation. The domain can be considered as the half of a liquid basin, the symmetry condition is applied on the right side of the domain, which results null normal derivatives for scalar fields and for the tangential component of vector fields, and null normal component of vector fields.

The interface will come to equilibrium as a result of the balance between the gravity and the capillary forces. The imposition of a contact angle at the beginning is a strong perturbation to the system, a capillary wave will be formed and propagate on the interface. To accelerate the attenuation of the capillary wave, large viscosities are used. Six

static contact angles ($\theta_e = 30^\circ, 45^\circ, 60^\circ, 120^\circ, 135^\circ, 150^\circ$) have been calculated. Values of physical variables used in simulations are shown in Table 2.1.

Table 2.1: Values of physical variables used in simulations.

ρ_l	ρ_g	μ_l	μ_g	γ	g
1000	1	0.01	0.001	0.0712	9.8

2.2.1 Dynamics of the contact point

The imposition of a contact angle at the triple-phase contact point perturbs the initial system. The contact point oscillates along the wall and generates a capillary wave on the initially horizontal interface.

Figure 2.4 shows dynamics of the contact point. At the beginning of the simulation, the contact point deviates from zero ($z = 0$) rapidly ($t < 0.1$) and arrives at a height larger than the maximum equilibrium height (see insets of Figure 2.4). The contact point is not stable, the competition between capillary forces and the gravity makes it oscillate and a capillary wave propagates on the interface. Under the viscous dissipation effect, the amplitude of oscillation decreases, subsequently, the capillary wave is completely attenuated and the contact point arrives at the equilibrium position determined by equation (2.10). The time to arrive at the equilibrium interface varies with the contact angle. It takes longer for an angle close to 90° (which means $|\theta_e - 90^\circ|$ is small). For two supplementary angles ¹ such as $\theta_e = 60^\circ, 120^\circ$, the behaviour is different: For a hydrophobic angle ($\theta_e > 90^\circ$), the first maximum deviation (first peak) is the largest and the maximum deviation (the amplitude of peaks) decreases with time, the envelope-line of the peaks is monotonic; whereas, for a hydrophilic angle ($\theta_e < 90^\circ$), the largest deviation is the second peak, then the envelope-line turns to be monotonic (see Figure 2.4 (c,d)).

For a hydrophilic case ($\theta_e < 90^\circ$), as the value of θ_e increases, the vertical component of the capillary force decreases, the deviation from the initial position is weakened and the amplitude of oscillation decreases too, whereas the time necessary to arrive at the equilibrium position increases (see Figure 2.5). As shown in the low panels of Figure 2.5,

¹The sum of the two angles is 180° .

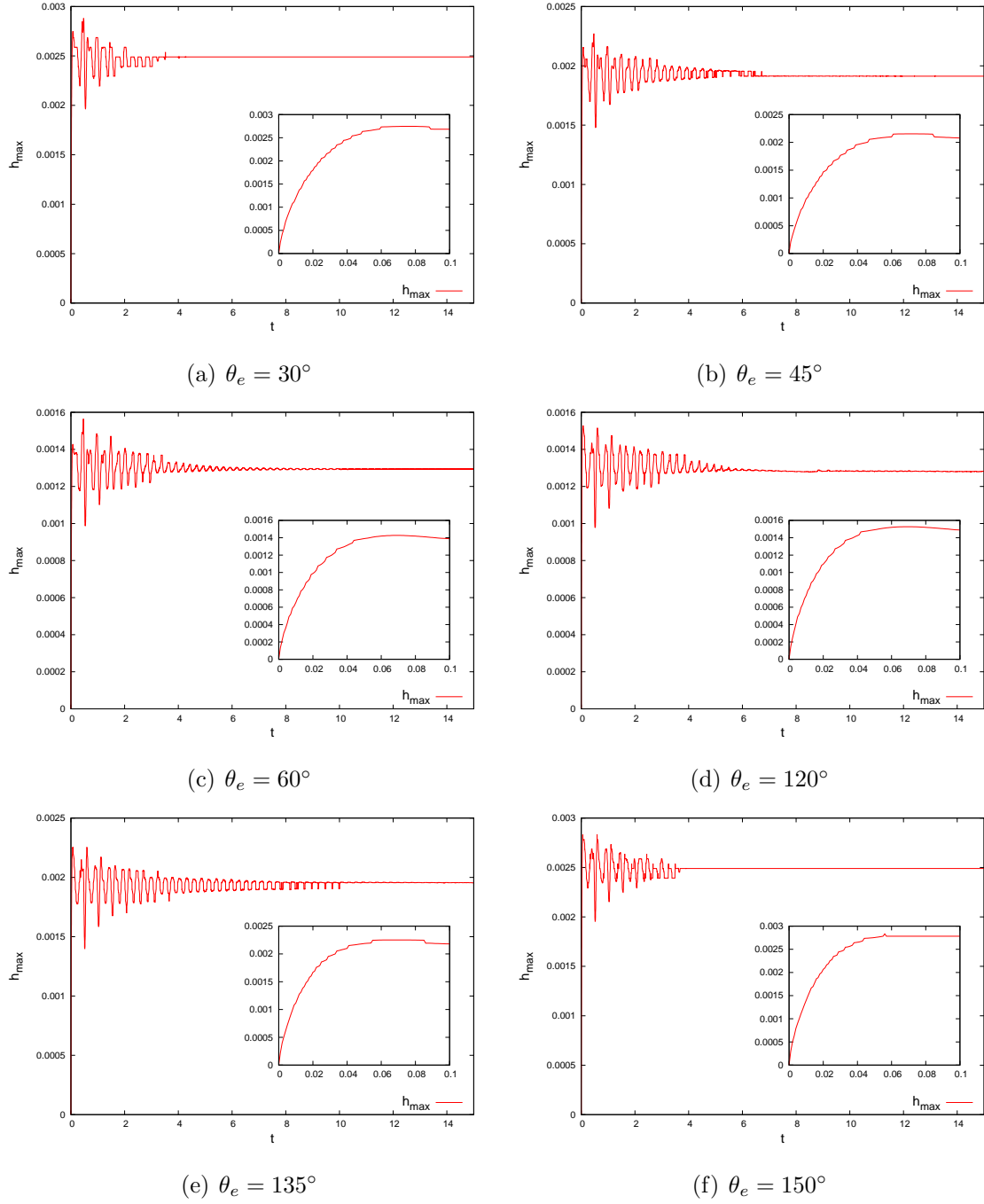


Figure 2.4: Maximum height of interface h_{\max} (height of the triple-phase contact point) as a function of time t for different contact angles: (a) $\theta_e = 30^\circ$, (b) $\theta_e = 45^\circ$, (c) $\theta_e = 60^\circ$, (d) $\theta_e = 120^\circ$, (e) $\theta_e = 135^\circ$, (f) $\theta_e = 150^\circ$. Inset shows a zoom of the evolution of h_{\max} at the beginning of the simulation ($t \leq 0.1$). h_{\max} is the height compared to the initial interface position $z = 0$ and for a contact angle $\theta_e > 90^\circ$, h_{\max} takes its absolute value.

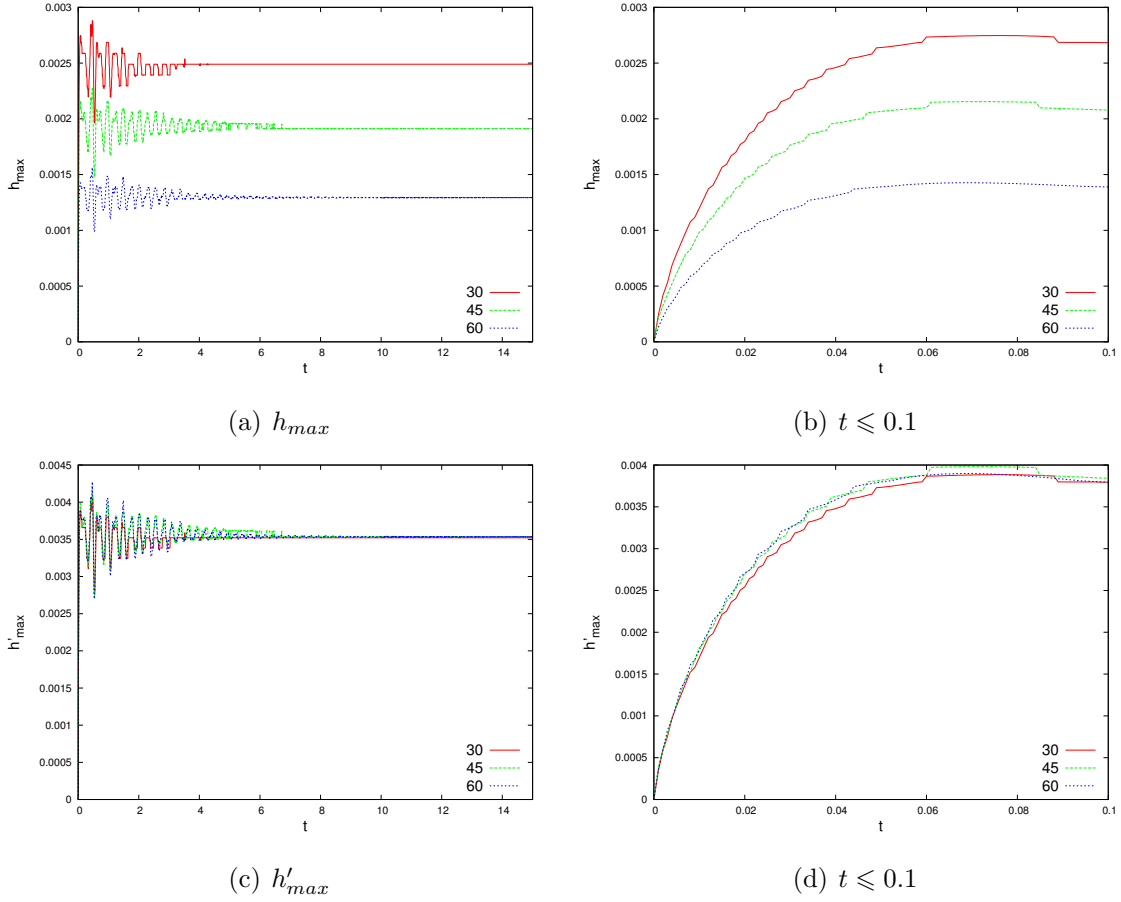


Figure 2.5: Comparison of the maximum height of interface h_{max} (height of the triple-phase contact point) for $\theta_e = 30^\circ, 45^\circ, 60^\circ$. h'_{max} is the value of h_{max} rescaled by $\sqrt{1 - \sin(\frac{\theta_e}{180}\pi)}$. Right panels are a zoom of the evolution of h_{max} (h'_{max}) at the beginning of the simulation ($t \leq 0.1$).

if we rescale the h_{max} by $\sqrt{1 - \sin(\frac{\theta_e}{180}\pi)}$ (which represents the contact angle effect to the maximum height of the equilibrium interface in equation (2.10)), the dynamics of the contact point shows a self-similarity.

2.2.2 Equilibrium interface

As a matter of mass conservation, the interface deviates from the initial position ($z = 0$). To simplify the comparison, we set the lowest (highest for hydrophobic cases) position of the equilibrium interface as the plane $z = 0$.

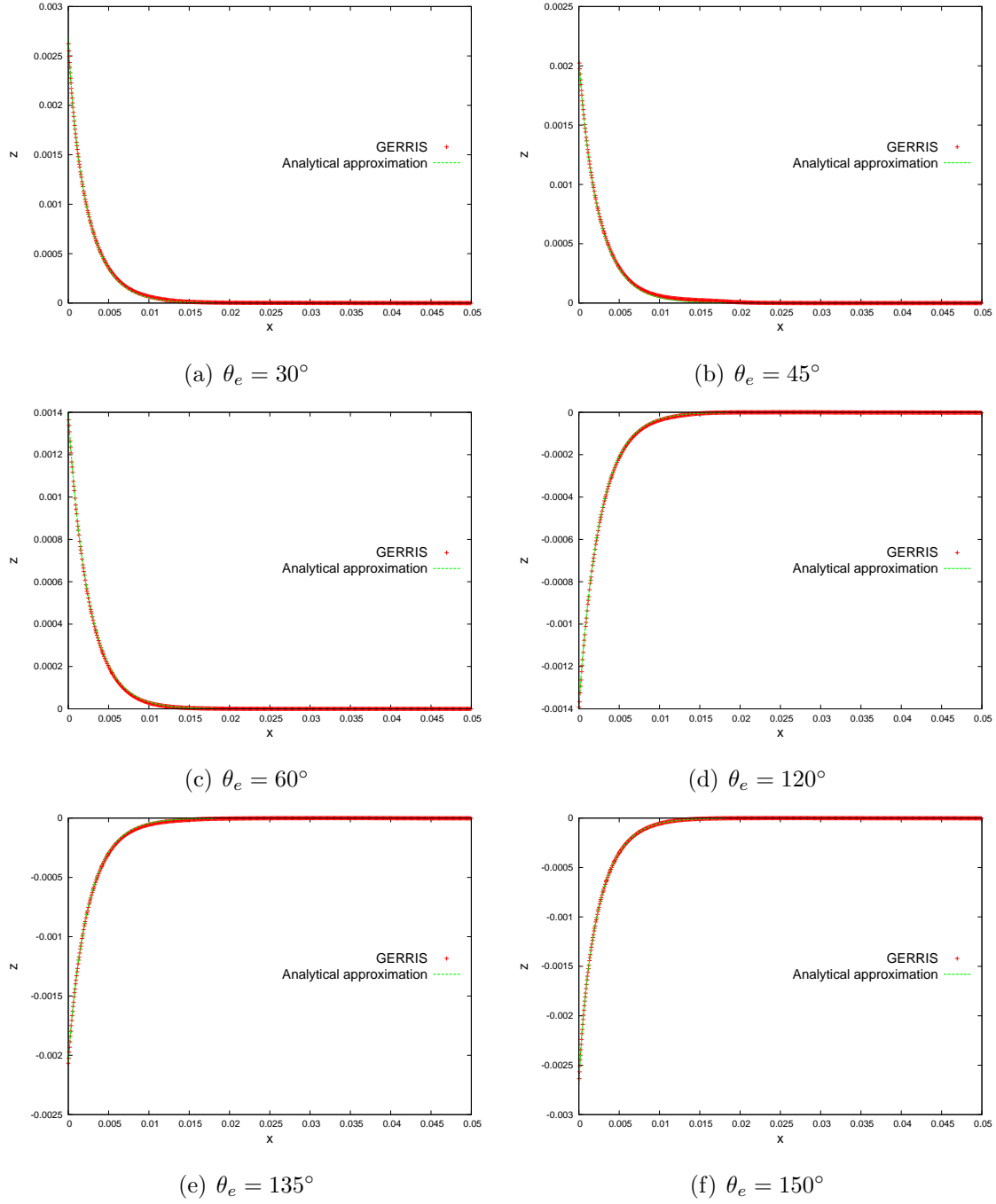


Figure 2.6: Comparison of the equilibrium interface profile between simulations and the analytical solution given by equation (2.7) at (a) $\theta_e = 30^\circ$, (b) $\theta_e = 45^\circ$, (c) $\theta_e = 60^\circ$, (d) $\theta_e = 120^\circ$, (e) $\theta_e = 135^\circ$, (f) $\theta_e = 150^\circ$. The plane $z = 0$ is set to the lowest (highest for hydrophobic cases) position of the equilibrium interface.

Figure 2.6 shows the comparison of the equilibrium interface profile between simulations and the analytical solution determined by equation (2.7). A good agreement is found.

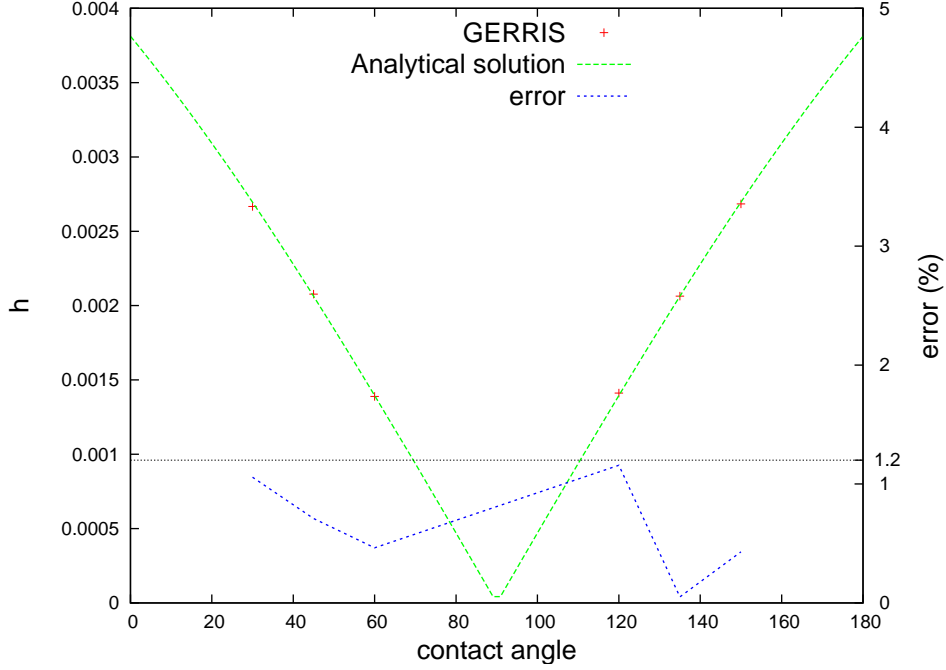


Figure 2.7: Symbols, green dashed line and left vertical axis: Maximum height of the equilibrium interface h as a function of the contact angle θ_e . Symbols denotes simulation results h_g , green line denotes h_a calculated by equation (2.10) $h = \sqrt{2}l_c\sqrt{1 - \sin\theta_e}$. Blue dashed line and right vertical axis: error ε of the simulation results compared to the analytical solution as a function of the contact angle θ_e . The horizontal line indicates the error value 1.2%.

We note the maximum height of the equilibrium interface h calculated by simulations as h_g and h calculated by equation (2.10) as h_a , and define the error of simulations as:

$$\varepsilon = 100 \frac{|h_a - h_g|}{h_a} \% \quad (2.11)$$

Figure 2.7 shows the comparison of the maximum height of the equilibrium interface h between numerical simulations and the analytical solution. The error is smaller than 1.2%. The simulations agrees quite well with the analytical solution. Figure 2.8 shows snapshots of the equilibrium interface with the adaptive mesh arrangement. The interface, especially the meniscus area, is well tracked by the adaptive mesh.

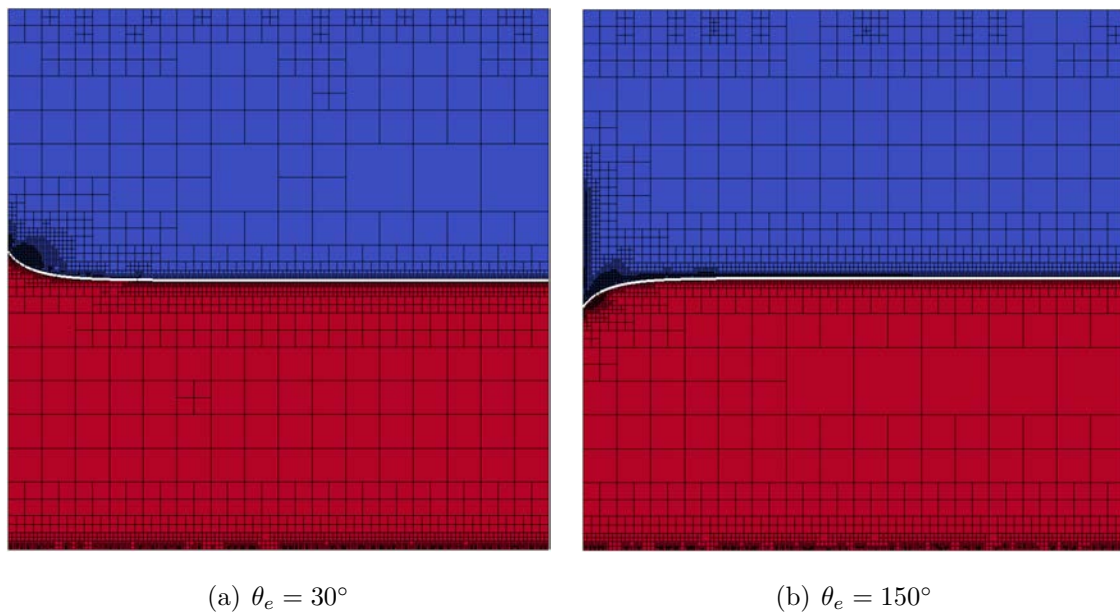


Figure 2.8: Snapshots of the equilibrium interface and the adaptive mesh arrangement at (a) $\theta_e = 30^\circ$, (b) $\theta_e = 150^\circ$. The interface, especially the meniscus area, is well tracked by the adaptive mesh. Colours represent different phases: White is the interface, blue is the gas phase and red is the liquid phase.

2.3 Conclusion

In this chapter, a classical interface issue - the meniscus on a vertical wall is studied to validate the numerical schemes used in the code GERRIS. The imposition of a contact angle at the beginning of the simulation introduces a perturbation to the system and the triple-phase contact point starts to oscillate. A capillary wave is generated by the oscillation of the contact point. The dynamics of the oscillation shows a self-similarity. A stronger oscillation is observed for a contact angle away from the threshold value 90° (which means the deviation $\Delta\theta = |\theta - 90^\circ|$ is bigger), but it takes less time to come to the equilibrium state.

The profile of the equilibrium interface is obtained from a force balance analysis. The error of the maximum height of the equilibrium interface is small and the equilibrium interface calculated by GERRIS agrees well with the analytical solution. The interface is well tracked by the adaptive quadtree mesh.

The code GERRIS shows a good performance in the computation of multiphase flows and it will be used to calculate a more complicated physical dynamics - the drop impact issue in the coming chapters.

Chapter

3

Gas effect in drop impact on a solid substrate

Contents

3.1 Physical description	56
3.2 Convergence test: analysis of the gas layer	59
3.3 Early stage of the impact	69
3.3.1 Constant density ratio $r = 0.003$	70
3.3.2 Constant viscosity ratio $m = 0.037$ and $m = 0.07$	75
3.4 Frontier between impact outcomes	75
3.5 Conclusion	79

Drop impact on a solid substrate involves liquid, solid and gas, any physical properties of the three phases could possibly influence the dynamics. Since more than a century, efforts have been taken in this fascinating phenomenon. More and more details of the dynamics have been discovered by experiments; theoretical and numerical investigations have been done to understand the splashing mechanism.

In the literature, the surrounding gas has been normally neglected because of the large density and viscosity ratio between liquid and gas. However, some striking experimental results have been recently reported [Xu *et al.*, 2005]. They discovered that only by decreasing the surrounding gas pressure, the splash can be completely suppressed and turned to a deposition even without the undulation of the liquid sheet. It implies the crucial effect of gas in the dynamics of drop impacts.

Since these striking discoveries, several models involving gas compressibility or gas non-continuum effect have been proposed to explain the role of gas. But the direct connection between compressibility, non-continuum effect and the splash mechanism is not clearly explained and there is still no clear understanding of the mechanism.

In this chapter, we make the direct numerical simulation of the drop impact onto a solid surface under the incompressible assumption and investigate the gas influence during the drop impact dynamics.

3.1 Physical description

The physical process of a drop impact on a solid substrate can be described as: a liquid droplet falls from a certain height, accelerates under the gravitational effect, approaches a solid substrate then impacts on the substrate with an impact velocity. It can show different behaviours (deposition, splashing, rebounding) under different impact conditions (for instance, the viscosity, the surrounding gas pressure or the roughness of the solid surface).

Considering the role of the gravitational effect, the impact process can be divided into two regimes:

First regime, from the starting position until the drop approaches the substrate. It is a gravity-driven motion. During this period, several forces (such as the gas viscous force, the gravity) apply on the drop, but the gravity is the only thrust of falling and it is dominant. The drop is accelerated from rest (or an initial velocity) by the gravity and the shape of the drop could be deformed from a sphere as a result of the gas viscous effect.

Second regime, subsequent to the first regime until the drop impacts on the substrate. In this regime, the drop has already a large velocity and it is close to the substrate. The duration of this regime is short and the gas effect becomes important. Apparently, the drop is decelerated and the acceleration effect of the gravity becomes subordinate. The variation of the drop velocity is no longer due to the gravity. A high deformation of the drop is observed and some complex interactions between the drop, the surrounding gas and the substrate occur. The time scale of these dynamics, which could originate the splashing, is very small and it could be of the order of several nanoseconds.

To measure the gravitational effect during the drop impact, a dimensionless number called Froude number is introduced. Its definition is the ratio between the inertia and the gravitational force and it can be expressed as

$$Fr = \frac{U^2}{gD} \sim \frac{H}{D} \quad (3.1)$$

where U is the drop velocity, g is the gravity, D is the drop diameter and H is the height from the starting position to the substrate. In the experiments of Xu *et al.* [2005], when the drop approaches the substrate (the second regime of the drop impact), the drop has a large velocity, the Froude number is large. The liquid inertia is dominant compared to the gravitational force. Since we are interested in the gas effect during the drop impact which is more important in the second regime, the gravity can be neglected during this high deformation regime and the shape deformation during the first regime is not considered either.

Now, the physical problem can be defined as: a circular drop falls from a small height h with a large initial velocity U_0 and the gravity is not considered. The drop will not be accelerated as a result of the absence of gravity¹. The solid surface is dry, flat, rigid, without roughness and a contact angle is defined. Liquid and gas are both considered incompressible.

The calculation domain is shown in Figure 3.1. The problem is solved axisymmetrically, a semi circular drop is placed along the left boarder ($r = 0$, which is the symmetry axis). The bottom boarder ($z = 0$) is considered as a solid substrate and a typical partially-wettable surface is considered with a contact angle $\theta = 90^\circ$.

Although a large initial velocity is imposed to replace the gravity acceleration regime and the drop is close to the substrate, the drop should be high enough in order to avoid the influence of the substrate at the beginning and show the entire dynamics of the interaction between the drop and the substrate. To determine the initial height h of the drop, we take four different values of h ($h = 0.05D, 0.1D, 0.25D, 0.5D$, where D is the drop diameter) and study the convergence of the interface height h_{r0} on the symmetry axis ($r = 0$).

With absence of the surrounding gas, the drop will contact the substrate at $t_{th} = h/U_0$. Figure 3.2 shows the temporal evolution of the interface height h_{r0} . For each h , the

¹Deceleration and deformation of the bottom part of the drop is observed in simulations when gravity is neglected during the high deformation regime. It is caused by the cushioning effect of the surrounding gas, which is a proof of the gas effect to the drop impact.

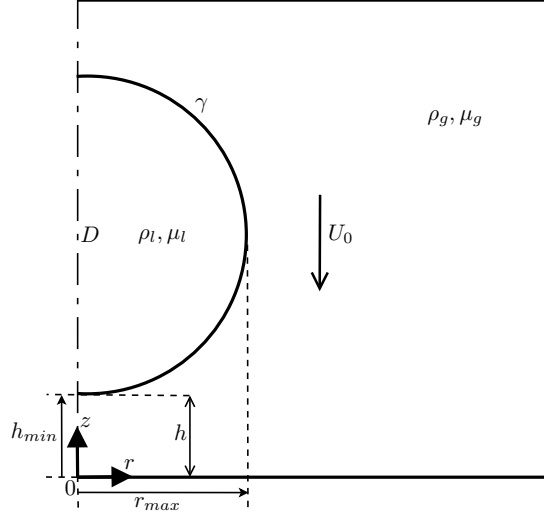


Figure 3.1: Calculation domain. The domain is constituted of a square. A semi circular drop of diameter D , density ρ_l and viscosity μ_l falls from a height h with an initial velocity U_0 , surrounding gas has a density ρ_g , a viscosity μ_g and a surface tension γ . The bottom boarder ($z = 0$) is considered as a solid substrate and a contact angle $\theta = 90^\circ$ is defined. h_{min} is the smallest height between the interface and the substrate and r_{max} is the largest radius of the liquid area.

moment of contact t_{th} is different, we rescale the time as $\tilde{t} = t - t_{th}$. The initial height h only influences the bottom interface of the drop. For $h = 0.05D$, the height of the bottom interface h_{r0} has an evident difference from h_{r0} of $h = 0.1D, 0.25D, 0.5D$ at the early stage of the impact (see Figure 3.2 (c), $\tilde{t} = [0, 0.3]$), the drop is too close to the substrate at the beginning, therefore, we take $h = 0.1D$ in further simulations.

Values of nondimensionlized physical parameters used in simulations ² are shown in Table 3.1. r is the density ratio $r = \rho_g/\rho_l$ and m is the viscosity ratio $m = \mu_g/\mu_l$. If we compare it with the example of a water drop of diameter $D = 3 \text{ mm}$ with an initial velocity of $U_0 = 3 \text{ m} \cdot \text{s}^{-1}$ (Table 1.4 in the section §1.2), the viscosity is 10 times larger than the real one. Large viscosities are used to enforce the gas effect and get a better vision of the gas layer ³. The Reynolds number $Re = 1000$ and the Weber number $We = 370$ in our simulations.

²An example of the GERRIS parameter file is presented in Appendix.

³The thickness of the gas layer is proportional to the gas viscosity, a detailed discussion is presented in the section §4.1.2.

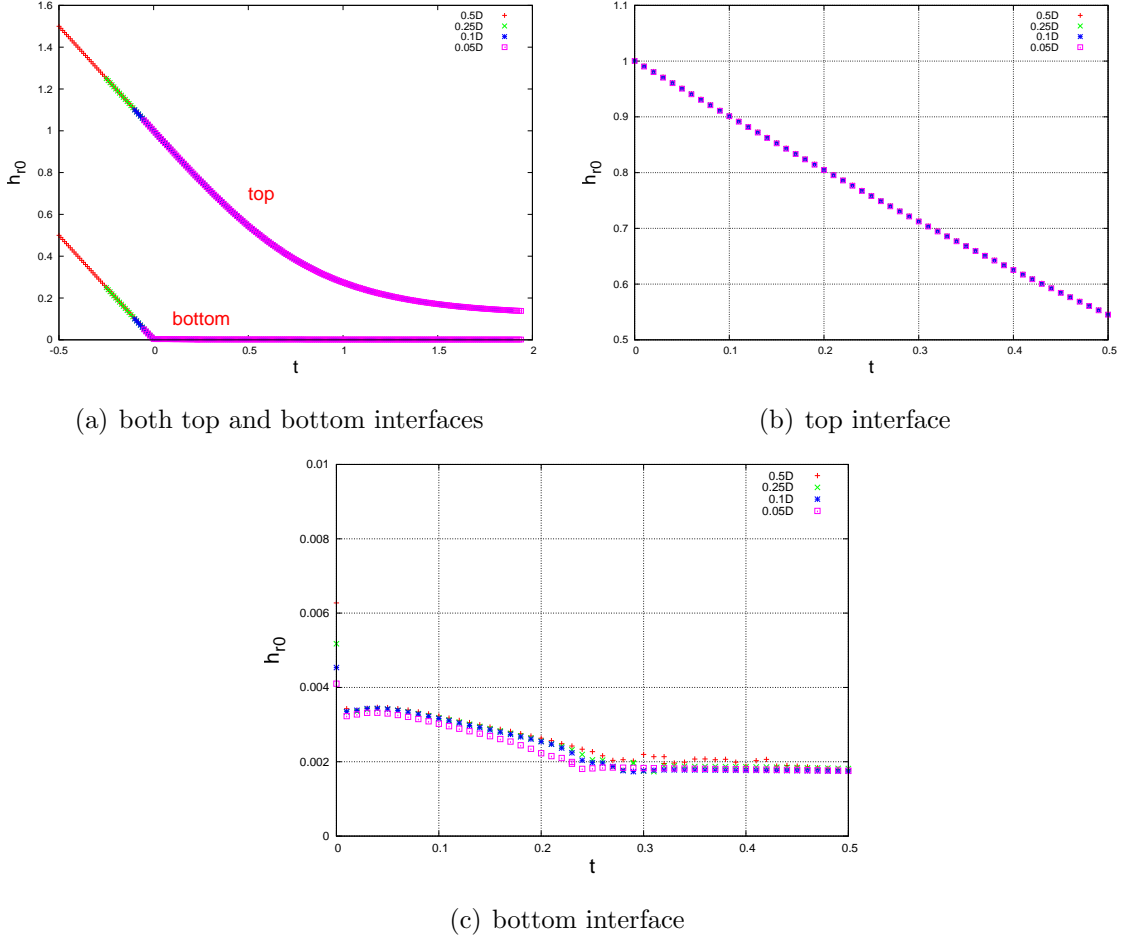


Figure 3.2: Interface height on the symmetry axis ($r = 0$) h_{r0} as a function of the rescaled time $\tilde{t} = t - h/U_0$ for $h = 0.05D, 0.1D, 0.25D, 0.5D$. In (a), the top and bottom curve correspond to the top and bottom interface respectively, (b) and (c) is a zoom of the top and bottom interface respectively.

Table 3.1: Values of nondimensionlized physical parameters in simulations

ρ_l^*	ρ_g^*	μ_l^*	μ_g^*	γ^*	U_0^*	D^*	h^*
1	r	0.001	$0.001m$	2.70×10^{-3}	1	1	0.1

3.2 Convergence test: analysis of the gas layer

In GERRIS, the adaptivity is applied in time and space by criteria defined by users, mesh amount and mesh refinement are controlled by a parameter called “refinement level n ”. As a characteristic of the quadtree mesh arrangement, for a refinement level n , the

maximum mesh amount is 4^n ⁴ and the smallest mesh size is $L/2^n$, where L is the length of the calculation domain. In the next, we use the refinement level n to describe the mesh arrangement.

Here, a convergence test is done to insure the accuracy of our computation. The case with a density ratio $r = 0.001$ and a viscosity ratio $m = 0.1$ is used. The convergence of the smallest height h_{r0} between the interface and the substrate on the symmetry axis $r = 0$ is investigated.

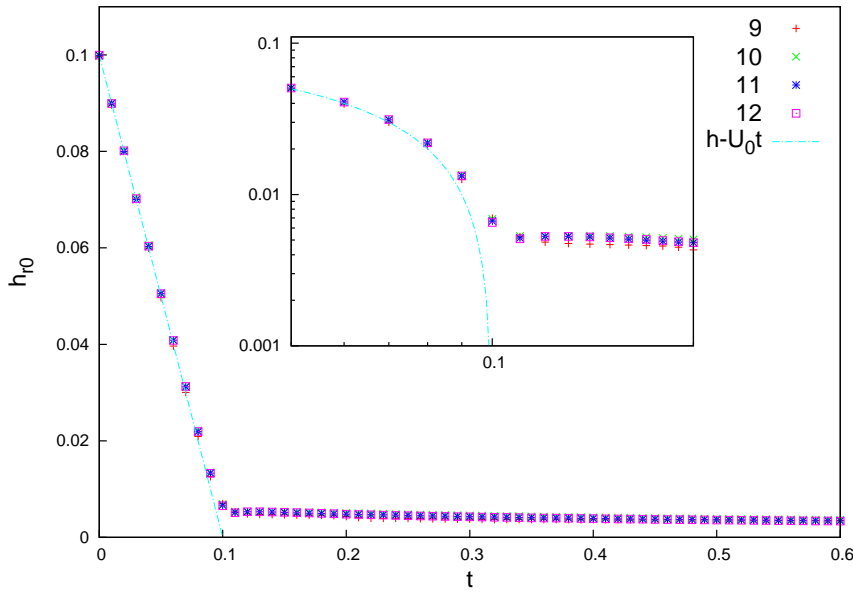


Figure 3.3: The smallest height h_{r0} between the interface and the substrate on the symmetry axis $r = 0$ as a function of time t for a refinement level $n = 9, 10, 11, 12$. The dash line represents the linear law of the drop movement without the gas effect : $h_{r0}(t) = h - U_0 t$. The intersection between the dash line and the axis t indicates the theoretical contact time $t_{th} = h/U_0 = 0.1$ with absence of the surrounding gas. Inset shows a zoom around the theoretical contact time t_{th} in a logarithmic scale.

As shown in Figure 3.3, the drop falls with a constant velocity at the beginning, the smallest height h_{r0} obeys a linear law $h_{r0}(t) = h - U_0 t$ (see dash line in Figure 3.3). When the drop approaches the substrate, it is decelerated by the gas and h_{r0} deviates from the linear law (see inset of Figure 3.3). If the gas effect is not considered, the drop will contact the substrate at $t_{th} = h/U_0 = 0.1$. After the moment $t = 0.1$, h_{r0} becomes almost constant. It implies that a gas layer exists between the drop and the substrate, or

⁴With the adaptivity, the real mesh amount is much smaller than 4^n .

an amount of gas is entrapped under the drop and a bubble is formed, h_{r0} represents the height of the bubble. The difference between different refinement levels is quite small (see inset of Figure 3.3), with a refinement level $n = 11$, a good accuracy of the computation can be guaranteed ⁵.

Figure 3.4 shows the real computing time cost for a dimensionless computing interval $\Delta t^* = 0.6$. The time cost increases exponentially. For a drop of diameter 3 mm with an initial velocity $3 \text{ m} \cdot \text{s}^{-1}$, to compute the dynamics in $\Delta t = \Delta t^* \cdot D/U = 0.6 \text{ ms}$, it takes 408470 s about 5 days for a refinement level $n = 12$. It is too expensive. The time cost of $n = 11$ is acceptable with a good computing accuracy. Therefore, the refinement level $n = 11$ is chosen for further computations.

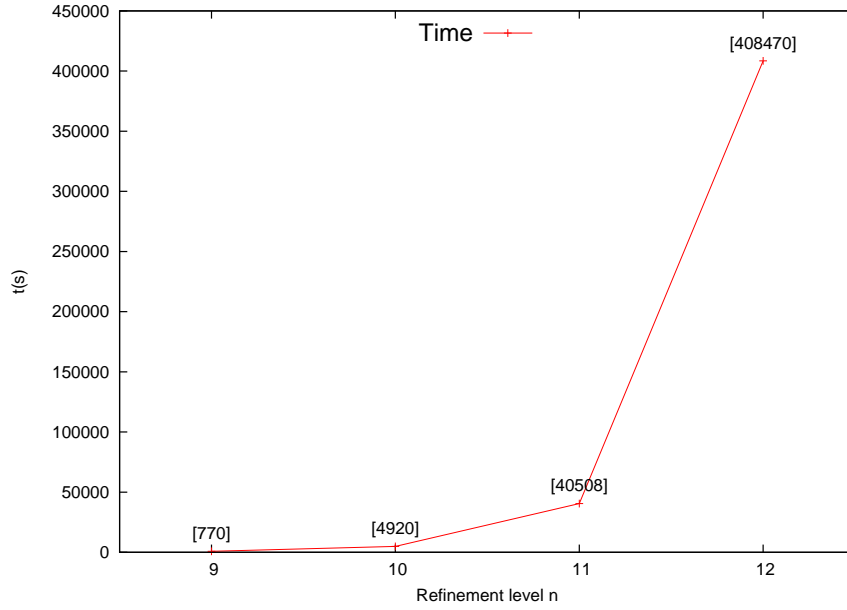


Figure 3.4: Real computing time cost (in s) for a dimensionless computing interval $t = 0.6$ at refinement level $n = 9, 10, 11, 12$.

Moreover, we also compare a more general smallest height h_{min} , which is measured between the interface and the substrate in the entire calculation domain (as defined in Figure 3.1). Figures 3.5 and 3.6 show the temporal evolution of the h_{min} -point. When the drop is far from the substrate, the h_{min} -point remains in the center of the drop (on the symmetry axis $r = 0$, see Figure 3.6), it coincides with the h_{r0} -point and obeys the

⁵The ideal convergence test is to verify the convergence for each density and viscosity ratio, whereas, it is too costly. Here, with the test of $r = 0.001$ and $m = 0.1$, we consider the convergence and accuracy are guaranteed in general.

same linear law $h(t) = h - U_0 t$ (see dash line in Figure 3.5). As the drop approaches the substrate, h_{min} deviates from the linear law and a gradually strengthened deceleration effect caused by the gas layer is observed.

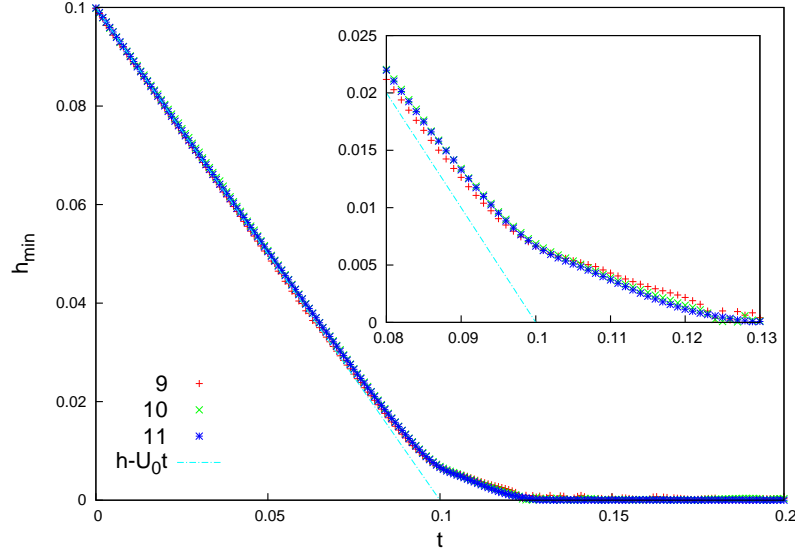


Figure 3.5: The smallest height h_{min} between the interface and the substrate in the entire calculation domain as a function of time t for a refinement level $n = 9, 10, 11$. Inset shows a zoom around the theoretical contact time t_{th} and indicates the deviation of the h_{min} -point from the linear law $h(t) = h - U_0 t$ (dash line). A gradually strengthened deceleration effect caused by the gas layer is observed.

It should be noticed that the deviation of h_{min} occurs earlier than h_{r0} and a change of slope is observed, which implies that the r -coordinate of the h_{min} -point is changed as confirmed in Figure 3.6, the h_{min} -point deviates from the center and moves towards the outside. Then, the drop contacts with the substrate, which makes $h_{min} = 0$ (see Figure 3.5) and the distribution of the r -coordinate of the h_{min} -point turns to be chaotic (see Figure 3.6).

Figure 3.6 shows that at the beginning of the simulation, some h_{min} -points are not on the symmetry axis for a refinement level $n = 9, 10$. It could not occur in the real dynamics. The temporal evolution of the h_{min} -point further proves the necessity of a refinement level $n = 11$.

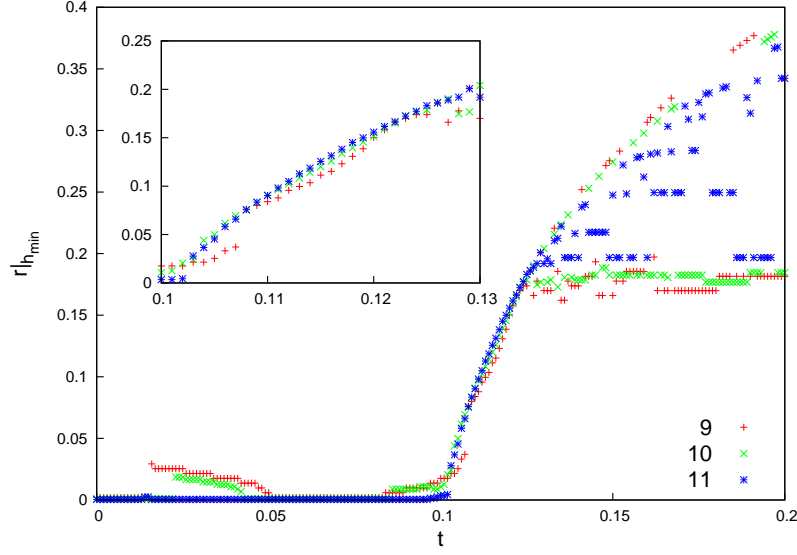


Figure 3.6: r -coordinate of the h_{min} -point as a function of time t for a refinement level $n = 9, 10, 11$. Inset shows a zoom around the theoretical contact time t_{th} and indicates the h_{min} -point deviates from the center of the drop to the outside before the contact with the substrate; it implies that during this period, an entrapped bubble is formed and the interaction between the drop and the gas layer could originate a splash.

If we continue the discussion of the regime-division in the section §3.1 and look into details of the early stage of the impact process, it can be divided into four stages (see Figure 3.7):

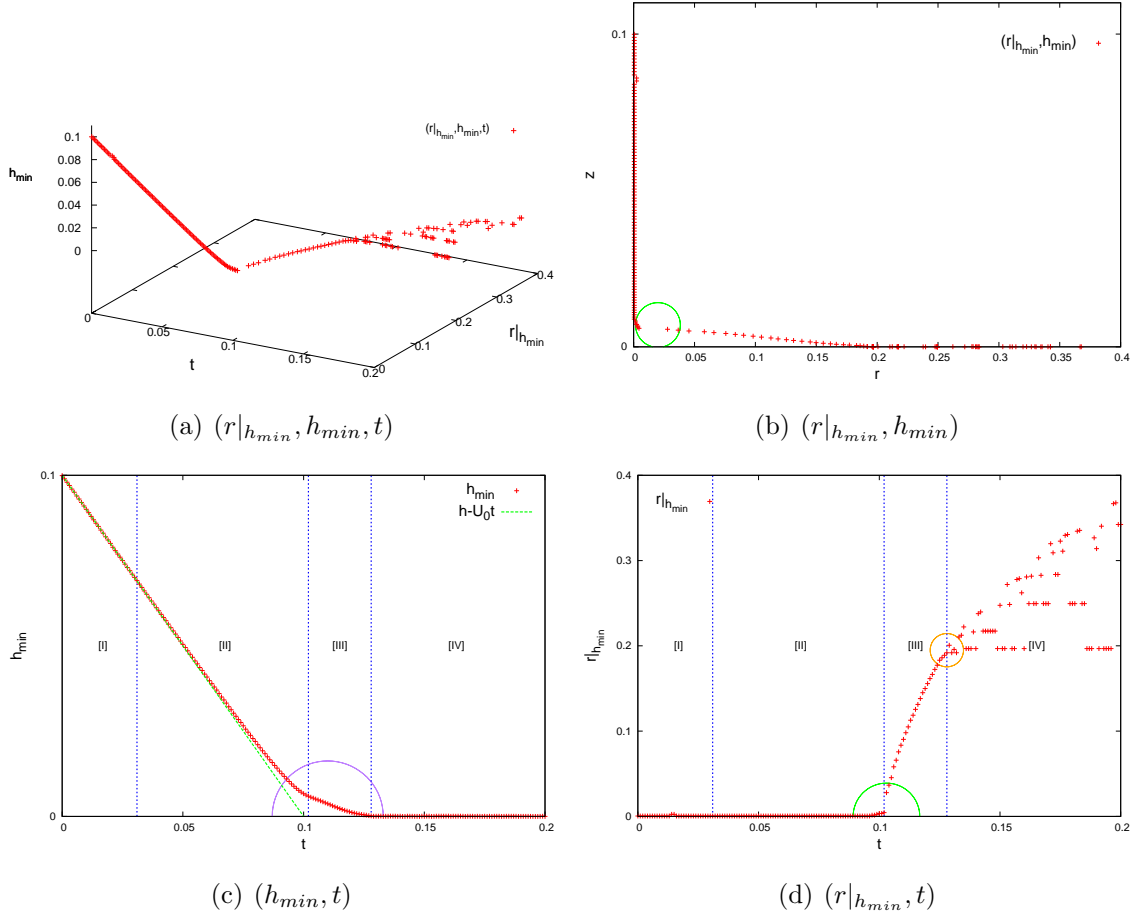
[I] **Linear movement** : the drop is “far” enough from the substrate, without the gravity, it falls with a constant velocity (this initial large velocity is due to the gravitational acceleration from the beginning). The gas viscous effect and the liquid inertial effect are not important in this stage, the velocity shield in the drop can be considered uniform and the deformation of the drop is negligible. The drop keeps the shape of a circle (a sphere in three dimensions).

[II] **Central deformation** : the drop starts to “feel” the existence of the substrate and is decelerated by the gas cushioning effect. The bottom part of the drop starts to deform from a circle, but the h_{min} -point remains at the center-bottom of the drop.

[III] **Dimple formation** : the drop further approaches the substrate, the gas cushioning effect becomes stronger. The bottom part of the drop continues to be decelerated and it will first arrive at a stagnation point (The vertical component of the velocity comes to zero). With further descending of the drop, the curvature of the bottom part

of the interface reverses, the h_{min} -point moves towards the outside (a position jump is observed as highlighted by a green circle in Figure 3.7 (b)). A corner-like interface is observed and a dimple is formed (see Figure 3.7 (e)). Around the theoretical contact time $t_{th} = h/U_0 = 0.1$, a slope change of the (h_{min}, t) curve (as highlighted by a purple circle in Figure 3.7(c)) and a value jump of the r-coordinate of the h_{min} -point (as highlighted by a green circle in Figure 3.7(d)) are observed, which corresponds to the formation of the dimple.

[IV] **Direct contact** : eventually, the drop contacts with the substrate, a part of gas is trapped under the drop and forms a bubble. As the upper part of the drop continues to fall, the contact point expands towards the outside and the wetted area of the solid surface extends. Figure 3.7 (f) shows a snapshot of the interface in this stage. The drop has a direct contact with the surface, a central entrapped bubble is formed and a series of small bubbles (local contacts) are also observed.



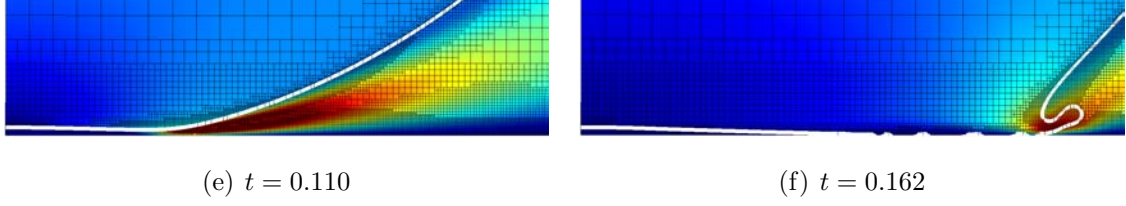


Figure 3.7: h_{min} -point evolution during the drop impact. (a) h_{min} -point position as a function of time, $(r|_{h_{min}}, h_{min}, t)$; (b) h_{min} -point distribution, $(r|_{h_{min}}, h_{min})$; (c) temporal evolution of h_{min} , (h_{min}, t) ; (d) temporal evolution of r-coordinate of the h_{min} -point, $(r|_{h_{min}}, t)$; (e) snapshot of the dimple - stage *III*; (f) snapshot of stage *IV*. In the snapshots, white curve represents the interface, black lines shows the adaptive mesh arrangement, the zone along the interface and around the strong velocity gradient (vorticity) are well refined and the color gradient represents the magnitude of the velocity.

Here, we make two important remarks:

Definition of contact

According to the simulation results, the drop will eventually contact with the solid surface. It is a numerical observation.

In the real physical mechanics, in a microscopic view, the contact process can be described as:

A liquid drop approaches a solid substrate, the physical distance between liquid molecules and solid molecules δ_p decreases. Gas evacuates from the area between the liquid and the solid, the quantity of gas molecules in this area decreases. Subsequently, the distance δ_p becomes comparable to the gas mean free path, there is few gas molecule between the drop and the substrate. When the distance δ_p comes to the molecular length scale, physical and chemical interactions between liquid molecules and solid molecules (such as the Van der Waals force) become important. There should be a threshold δ_{pt} , when δ_p is close to δ_{pt} , the molecules of two materials becomes so close that macroscopically we observe a direct contact between the liquid drop and the solid substrate.

δ_{pt} is probably a function of the properties of both liquid and solid materials. At the Standard Atmospheric Pressure (SAP $1.01325 \times 10^5 \text{ Pa}$) and the ambient temperature (20°C), the mean free path of the dry air is $65 \text{ nm} = 6.5 \times 10^{-8} \text{ m}$ [Jennings, 1988], the average distance between two water molecules is $2.8 \text{ \AA} = 2.8 \times 10^{-10} \text{ m}$ and the average

distance between two glass molecules is of the order of 10^{-10} m ⁶. Therefore, the threshold value δ_{pt} is of the order of $10^{-8} \sim 10^{-10} \text{ m}$ for a water drop impacting on a glass substrate.

In the numerical simulations, as a limit of the computing capacity, the refinement level is limited ($n = 11$ in our simulations)⁷ and the smallest size of a cell Δx has a certain value. When the drop approaches the solid surface, the distance between the interface and the solid boundary δ_n (both h_{r0} and h_{min} are examples of δ_n) decreases. From a moment, the interface will enter into the last gas cell above the solid boundary ($\delta_n \leq \Delta x$). There should be also a threshold δ_{nt} , when δ_n is smaller or equal to δ_{nt} , the gas percentage in a cell becomes very small. In the next step of the computation, the code will treat the cell as a full liquid cell. Apparently, the liquid drop contacts with the solid surface.

δ_{nt} is probably also a function of the properties of both liquid and solid materials (such as the liquid density, the liquid viscosity and the contact angle and the surface tension)⁸. In our simulations, the smallest size of a cell $\Delta x \approx 1 \times 10^{-3}$. For a drop of diameter $3 \times 10^{-3} \text{ m}$, it corresponds to a real length of the order of $1 \times 10^{-6} \text{ m}$. If we suppose $\delta_{nt} \sim 0.1\Delta x$, $\delta_{nt} \approx 1 \times 10^{-7} \text{ m}$.

It should be mentioned that, with the limit of numerical computations, δ_{nt} is not exactly equal to δ_{pt} . But the dynamics observed in numerical simulations should be similar to the real physical process and the characteristics of the mechanics are invariant. In order to reduce the influence of this issue, we fix our refinement level at $n = 11$, keep both liquid and solid properties constant in all simulations and focus on the gas effect. It should make both δ_{pt} and δ_{nt} constant in all simulations and have no influence in the mechanism investigation.

Chaotic distribution

A chaotic distribution of the r-coordinate of the h_{min} -point is observed (see Figure 3.6 and Figure 3.7 (a,d)). The existence of a series of small bubbles explains this phenomenon. As shown in Figure 3.7(f), after the first contact between the drop and the substrate, the

⁶The average distance between two glass molecules varies a lot according to the types of glass, it is close to 0.2 nm in the paper of Muller *et al.* [1993].

⁷The refinement level can be raised to any number if the computer is powerful enough. But there is a physical limit. If the corresponding physical length is smaller than the average distance between solid molecules or smaller than δ_{pt} , the simulations become physically meaningless.

⁸The mathematical accuracy of the simulation code can also play a role.

wetted area is not developed to a continuous zone but several discrete contacts are formed. As the contact line advances, some gas will be trapped, forms a small bubble and a new contact area. Subsequently, a series of small bubbles are formed. Since the algorithm to find the h_{min} -point will find several points satisfying the h_{min} -rule and only one point is taken at a moment, the multi-contact causes the chaotic distribution.

There is rich information in the chaotic area (see Figure 3.8). The start position of the chaotic region indicates the beginning of the direct contact. Two envelope-lines of the chaotic region demonstrate that the lower horizontal line indicates the radius of the central entrapped bubble r_b (see blue dash line in Figure 3.8) and the higher curve indicates the radius of the extreme contact point away from the center (or the radius of the wetted area r_w) (see green dash line in Figure 3.8). It is observed that the central entrapped bubble remains stationary after contact ($r_b = \text{constant}$). The difference between the two envelope-lines at a certain moment is equal to the size of the wetted area.

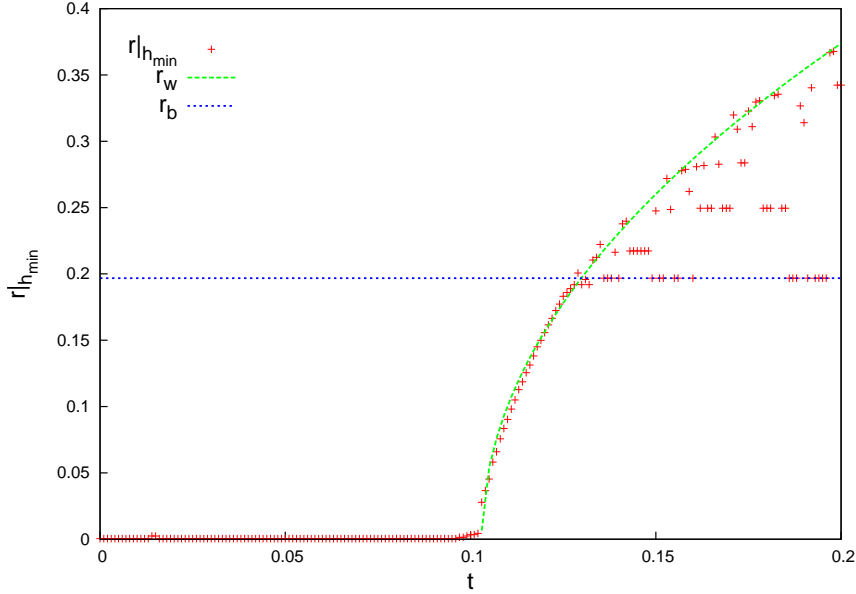


Figure 3.8: Envelope-lines of the h_{min} -point. Symbols denote the temporal evolution of the r -coordinate of the h_{min} -point, the horizontal blue dash line r_b is the radius of the central entrapped bubble and the green dash curve r_w is the radius of the wetted area.

A liquid drop falls towards a solid substrate, if we do not consider the gas effect, the drop will contact the substrate at $t_{th} = h/U_0$. We rescale the time as $\tilde{t} = t - t_{th}$ and suppose the substrate is virtual and the drop can penetrate into the solid. At the moment

\tilde{t} , the drop penetrates into the solid with a distance $U\tilde{t}$ and the intersection between the drop interface and the solid surface (considered as a virtual wetted radius) is $r_v = \sqrt{DU\tilde{t}}$.

In reality, drop stays above the substrate, as a matter of mass conservation, the part of liquid “penetrated” into the solid needs to evacuate towards the outside. The radius of the wetted area r_w is proportional to r_v :

$$r_w = C \cdot r_v = C\sqrt{DU\tilde{t}} \quad (3.2)$$

For a liquid drop impacting on a liquid basin, Josserand and Zaleski [2003] has found the same law for the horizontal length scale r_K of base of jet from the origin: $r_K = C\sqrt{DU\tilde{t}}$ where C is a numerical constant. In our numerical practice, we find C is equal to 1.2.

In our simulations, the rescaled time system $\tilde{t} = t - t_{th}$ corresponds to stage [III] and [IV]. But as a result of the gas cushioning effect, the contact time is not equal to $t_{th} = h/U_0$. We consider the starting zero point at the moment t_d where the dimple starts to form, which means h_{min} point starts to deviate from the center. Then the time is rescaled as $\tilde{t} = t - t_d$. Figure 3.8 indicates that t_d is in the regime of $t = [0.102, 0.103]$ and we take $t_d = 0.103$.

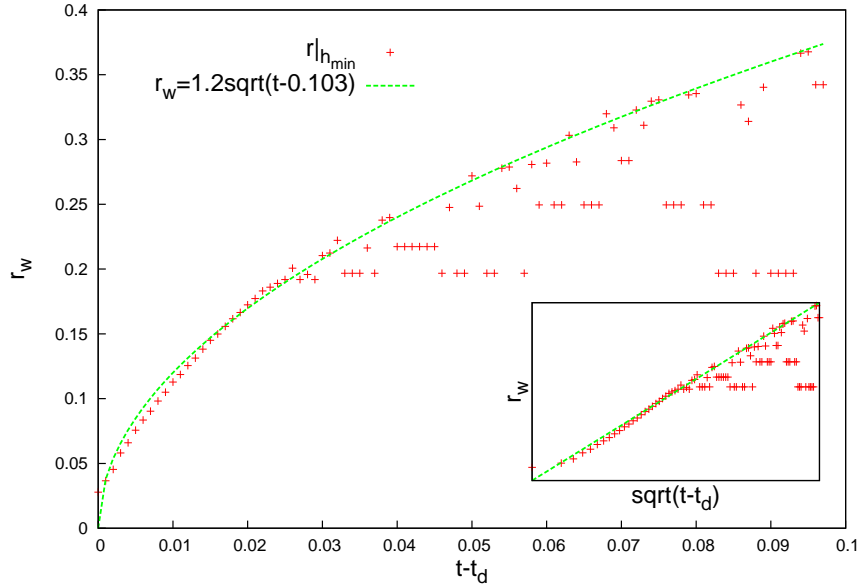


Figure 3.9: Radius of the wetted area r_w as a function of time. Time is rescaled by the dimple-formation time t_d , $\tilde{t} = t - t_d$. Inset shows the relation between r_w and $\sqrt{\tilde{t}}$. Symbols denote the temporal evolution of the r -coordinate of the h_{min} -point, dash curve is determined by the law $r_w = 1.2\sqrt{DU\tilde{t}}$.

Figure 3.9 shows the comparison between simulation results and the law of $r_w = 1.2\sqrt{DUt}$. A good agreement is found. The radius of the wetted area r_w obeys the same law as in a liquid/liquid impact. It implies that some connection possibly exists in the splashing mechanism for both liquid/liquid and liquid/solid impacts.

3.3 Early stage of the impact

The dynamics at the early stage of the impact determines the outcome. With the state-of-art high speed camera, more details of the dynamics are discovered, but the time and space precision is still not high enough to catch the dynamics at the very early stage of the impact. To investigate the gas effect in the early stage of the drop impact, three series of cases are studied with a corresponding time distinction of $1 \times 10^{-7} \text{ s}$ ⁹: case (I), we fix the density ratio $r = \rho_g/\rho_l = 0.003$ and vary the viscosity ratio $m = \mu_g/\mu_l = 0.01, 0.035, 0.04, 0.06, 0.07, 0.15$; case (II), we fix the viscosity ratio $m = 0.037$ and vary the density ratio $r = 0.0005, 0.001, 0.0015, 0.004$; case (III), we fix the viscosity ratio $m = 0.07$ and vary the density ratio $r = 0.0005, 0.001, 0.0015, 0.004$ (see Figure 3.10).

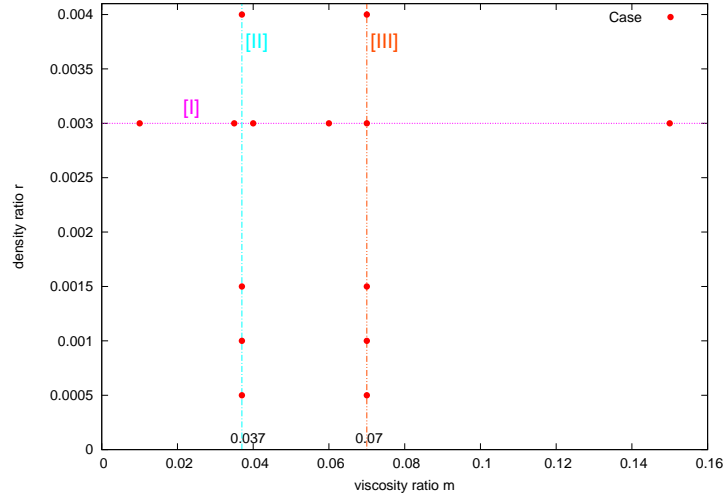


Figure 3.10: Case study: case (I) constant density ratio $r = 0.003$, case (II) constant viscosity ratio $m = 0.037$ and case (III) constant viscosity ratio $m = 0.07$.

⁹In the experiments of Kolinski *et al.* [2012], theoretically they can achieve an ideal temporal distinction of the order of 10^{-6} s and it is the highest time precision in experiments currently. In simulations, we take a time distinction of $\Delta t^* = 10^{-4}$. As shown in Table 1.1, $t = \frac{D}{U_0} t^*$, for a water drop of diameter $D = 3 \text{ mm}$ with an initial velocity of $U_0 = 3 \text{ m} \cdot \text{s}^{-1}$, the corresponding time distinction is $\Delta t = 10^{-7} \text{ s}$.

3.3.1 Constant density ratio $r = 0.003$

In simulations, three different outcomes are observed: for a small viscosity ratio $m = 0.01, 0.035$, drop spreads on the substrate and remains on it without splash; for a medium viscosity ratio $m = 0.04, 0.06$, drop first contacts and spreads on the substrate, then a part of the liquid film is detached from the substrate and a jet is formed and developed to a splash, we define this type of splash as a “**detachment-splash**”; for a large viscosity ratio $m = 0.07, 0.15$, a small jet is already formed before the contact with the substrate (which will be developed to a splash) and the drop then contacts the substrate, we define this type of splash as a “**jet-splash**”.

A drop falls from a height $h = 0.1D = 0.1$ with a velocity $U_0 = 1$. As the gravity is already ignored, with absence of gas, the drop will contact the substrate at the theoretical contact time $t_{th} = h/U_0 = 0.1$. At the theoretical contact time t_{th} , the drop is close to the substrate, but the gas cushioning effect delays its contact even for a small viscosity ratio. The drop remains almost circular, a slight deformation is only observed in the bottom part of the drop. A more viscous gas enforces the gas deceleration effect and a larger local deformation of the interface is produced. The gas under the drop evacuates fast towards the outside (see Figure 3.11).

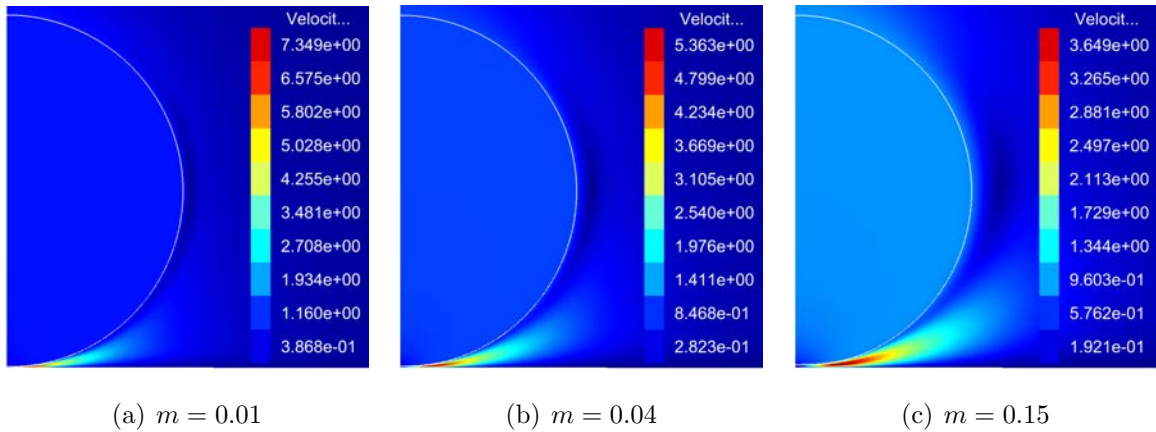


Figure 3.11: Snapshots at the theoretical contact time $t_{th} = 0.1$ for different outcomes: (a) non-splash, $m = 0.01$; (b) detachment-splash, $m = 0.04$; (c) jet-splash, $m = 0.15$. Colour gradient represents the magnitude of the velocity.

When the drop approaches the substrate, the pressure in the gas layer increases. The bottom central part of the drop is decelerated from a high impact velocity to rest. As the drop continues to descend, a dimple is formed and the bottom part of the drop develops

a horizontal velocity. The size of the dimple increases with the gas viscosity. The gas continues to evacuate at a high velocity (see Figure 3.12).

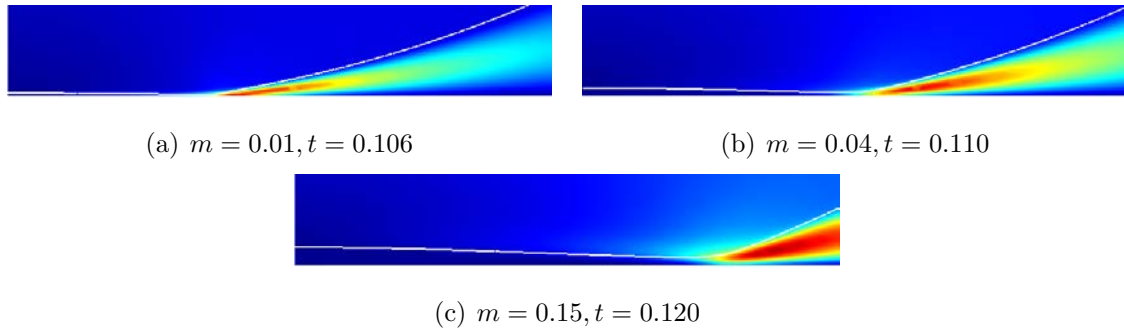


Figure 3.12: Snapshots of the dimple for different outcomes: (a) non-splash, $m = 0.01$; (b) detachment-splash, $m = 0.04$; (c) jet-splash, $m = 0.15$. Colour gradient represents the magnitude of the velocity.

For a deposition (non-splash) or a detachment-splash, the drop contacts with the substrate and simultaneously a thin liquid sheet is ejected towards the outside with a large velocity; for a jet-splash, a thin liquid sheet is already ejected with a large velocity before the contact with the substrate (see Figure 3.13).

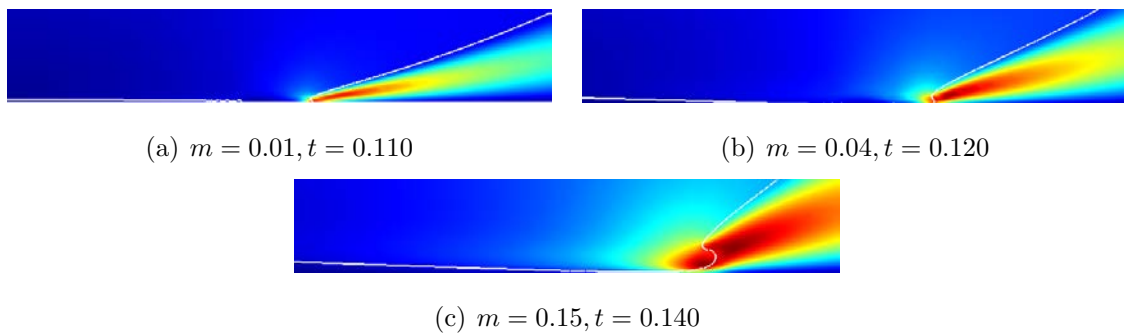


Figure 3.13: Snapshots of the drop “contact” with the substrate for different outcomes: (a) non-splash, $m = 0.01$; (b) detachment-splash, $m = 0.04$; (c) jet-splash, $m = 0.15$ (The contact has not yet occurred). Colour gradient represents the magnitude of the velocity.

For a deposition, the sheet remains on the solid surface; for a detachment-splash, the sheet detaches from the surface and forms a jet; for a jet-splash, the drop eventually contacts with the substrate and a series of small bubbles are observed. In all three outcomes, a central entrapped bubble always exists (see Figure 3.14).

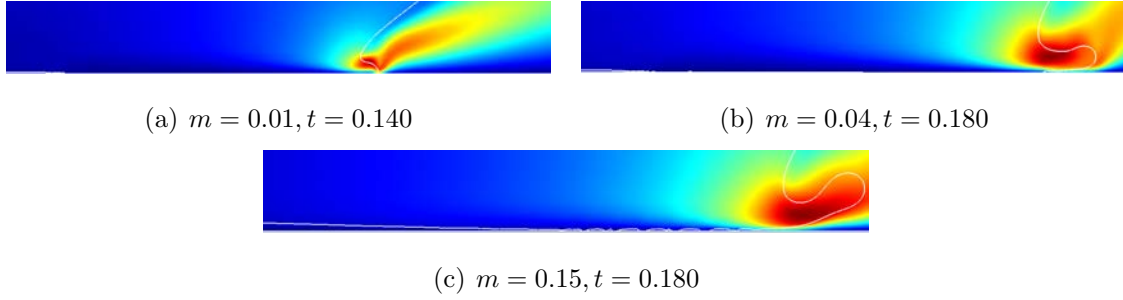


Figure 3.14: Snapshots of the sheet development for different outcomes: (a) non-splash, $m = 0.01$; (b) detachment-splash, $m = 0.04$; (c) jet-splash, $m = 0.15$. Colour gradient represents the magnitude of the velocity.

In a deposition case, drop remains on the substrate and the sheet extends fast; under no-slip boundary condition, a velocity boundary layer is formed in the liquid sheet close to the solid. In splash cases, the velocity is nearly uniform in the jet (Figure 3.15).

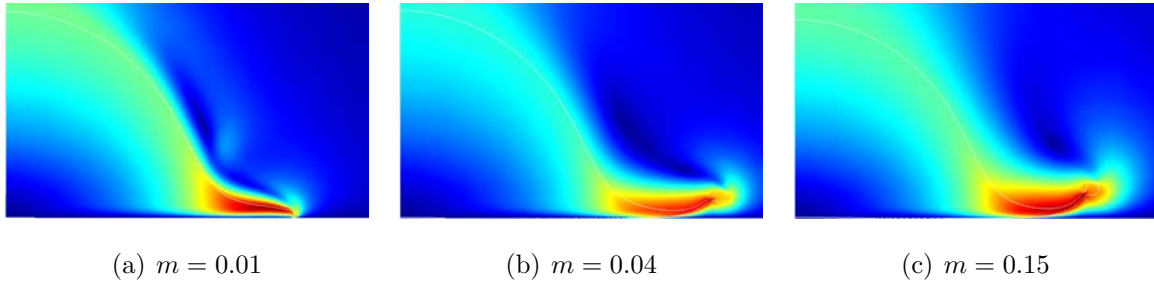


Figure 3.15: Snapshots of a fully developed moment $t = 0.5$ for different outcomes: (a) non-splash, $m = 0.01$; (b) detachment-splash, $m = 0.04$; (c) jet-splash, $m = 0.15$. Colour gradient represents the magnitude of the velocity.

Figure 3.16 shows the temporal evolution of the interface profile for three outcomes. The upper part of the interface has nearly the same variation and keeps almost circular in three outcomes. Figure 3.17 shows a zoom of the interface close to the substrate. By increasing the gas viscosity, the contact with the substrate is delayed, the size of the dimple increases. As a consequence, the radius of the central entrapped bubble is bigger for a larger gas viscosity but the shape of the bubble does not change during the drop impact. At the early stage of the impact, the variation of gas properties has already originated different outcomes. In the case of a deposition or a detachment-splash, the profile of the thin liquid sheet is different. For the deposition, the rim of the liquid sheet is flat and the upper interface of the sheet is nearly parallel to the solid surface; whereas,

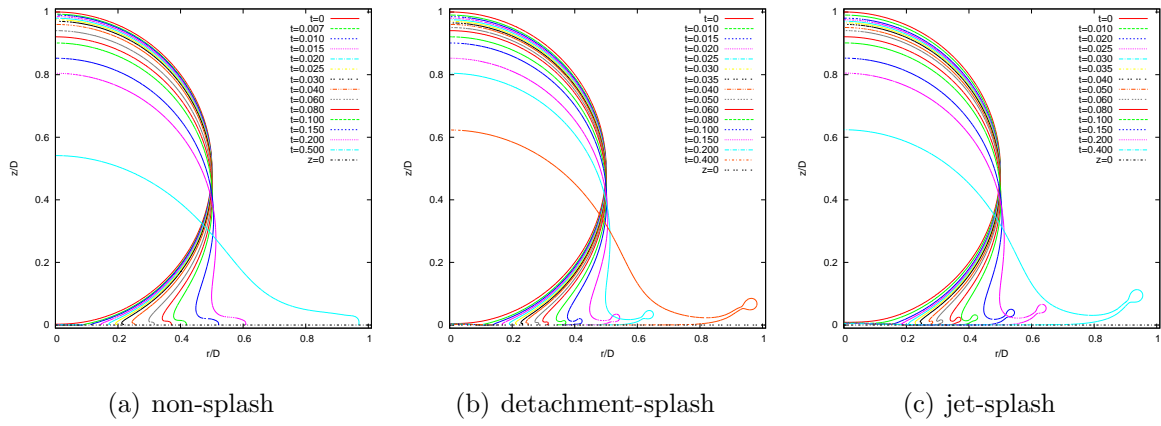


Figure 3.16: Interface evolution: (a) non-splash, $m = 0.01$; (b) detachment-splash, $m = 0.04$; (c) jet-splash, $m = 0.15$. The time is rescaled as $t = t - t_{th} = t - 0.1$. The line $z = 0$ represents the solid substrate.

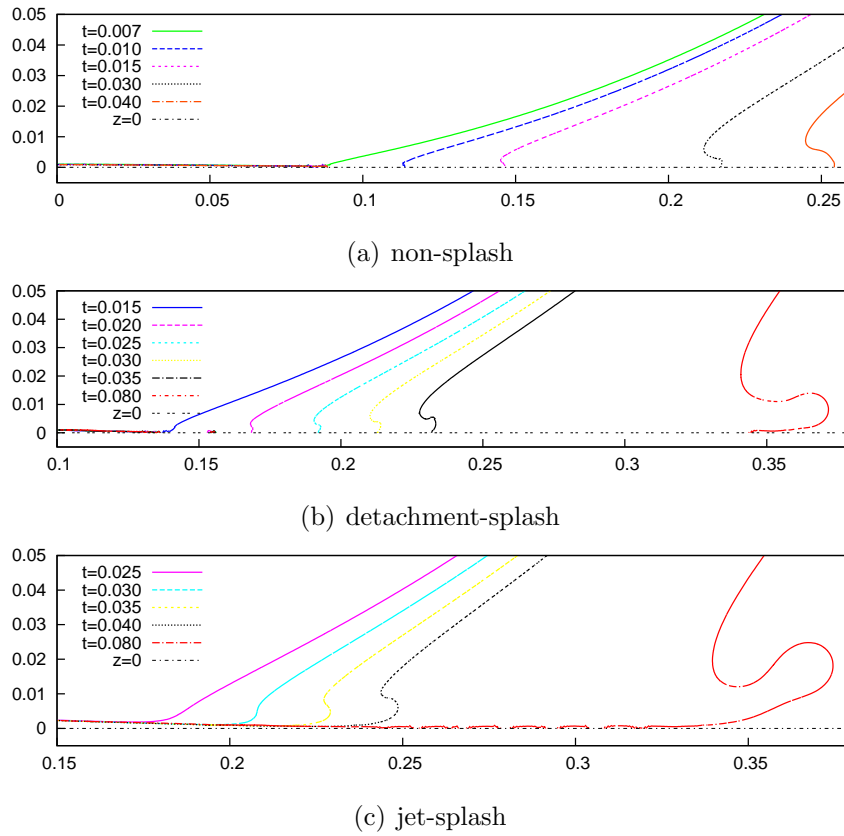


Figure 3.17: Evolution of the interface close to the substrate: (a) non-splash, $m = 0.01$; (b) detachment-splash, $m = 0.04$; (c) jet-splash, $m = 0.15$. The time is rescaled as $t = t - t_{th} = t - 0.1$. The line $z = 0$ represents the solid substrate.

for the detachment-splash, a salient is observed at the rim of the sheet, which can be considered as the detachment of the rim of the sheet, or the ejection of a secondary jet. The deflection of the jet occurs fast and is stronger for a bigger viscosity even in a shorter time interval after the contact (see the interface at $t = 0.080$ in Figure 3.17 (b) and (c)). The gas viscous effect play an important role in the impact dynamics.

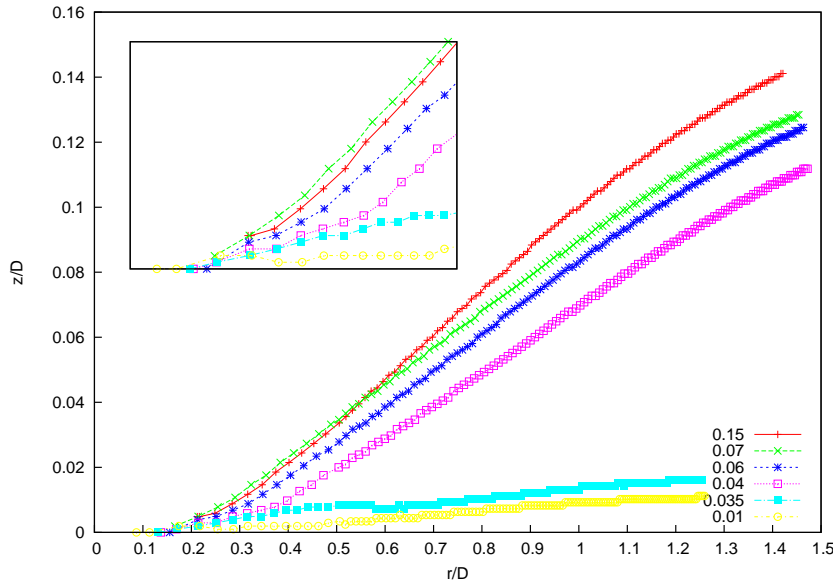


Figure 3.18: Position evolution of the rim of the thin liquid sheet for different viscosity ratios $m = 0.01, 0.035, 0.04, 0.06, 0.07, 0.15$ at a constant density ratio $r = 0.003$. Inset is a zoom near the zero point.

Figure 3.18 shows the position evolution of the rim of the thin liquid sheet, an evident difference between the deposition and the splash is observed. For deposition cases ($m = 0.01, 0.035$), the sheet remains on the substrate, the non-null position of the rim results from the thickness of the sheet. For splash cases ($m = 0.04, 0.06, 0.07, 0.15$), a larger gas viscosity produces a higher jet. From the inset of Figure 3.18 we should notice that transition between the deposition (symbols ‘solid square’ in the figure, $m = 0.035$) and the splash (symbols ‘hollow square’ in the figure, $m = 0.04$) is mild at the beginning of the impact. For a detachment-splash, the height of the rim starts from zero (symbols ‘hollow square’ and ‘star’ in the figure, $m = 0.04, 0.06$). For a jet-splash, the height of the rim does not start from zero, which implies the jet is formed before the contact; the rim starts from a higher position as gas viscosity increases, which implies the gas layer becomes thicker (symbols ‘cross’ and ‘plus’ in the figure, $m = 0.07, 0.15$).

3.3.2 Constant viscosity ratio $m = 0.037$ and $m = 0.07$

For a small viscosity ratio $m = 0.037$, two different outcomes are observed: for small density ratios $r = 0.0005, 0.001$, there is no splash, drop extends on the substrate; for large density ratios $r = 0.0015, 0.004$, a detachment-splash is observed. The height of rim decreases by decreasing the density ratio r and an evident transition from non-splash to detachment-splash is observed (see Figure 3.19(a)).

For a big viscosity ratio $m = 0.07$, the splash always forms and two different types are observed. For small density ratios $r = 0.0005, 0.001$, it is a detachment-splash; for large density ratios $r = 0.0015, 0.004$, it turns to be a jet-splash. As shown in Figure 3.19(b), the height of the rim decreases by lowering the density ratio. A similar variation of the position of the rim is found, the difference between the two types of splash is not evident.

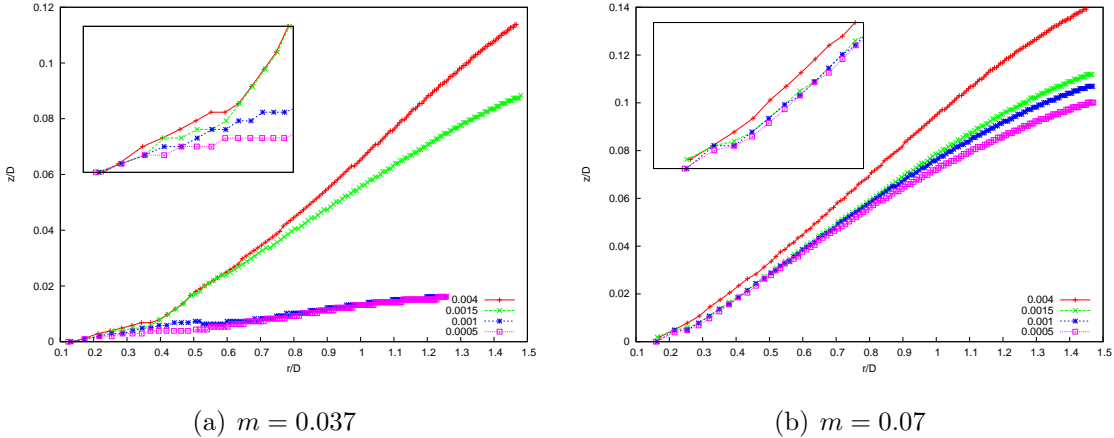


Figure 3.19: Position evolution of the rim of the thin liquid sheet on varying the density ratio $r = 0.0005, 0.001, 0.0015, 0.004$ with a constant viscosity ratio: (a) $m = 0.037$ and (b) $m = 0.07$. Inset is a zoom near the zero point.

3.4 Frontier between impact outcomes

The results in the section §3.3 indicates the existence of frontiers between different outcomes. Two dimensionless numbers have been introduced to measure the gas effect: the density ratio $r = \rho_g/\rho_l$ and the viscosity ratio $m = \mu_g/\mu_l$. A series of simulations have been done on varying the two ratios only. As the liquid properties keep constant in simulations, we have a constant Reynolds number $Re = 1000$ and a constant Weber number $We = 370$.

Gas inertia is not considered in the lubrication theory, only the gas viscous effect is taken into account, therefore, the frontier predicted by the lubrication approximation should be straight and have no variation by changing the gas density. However, a curved frontier between non-splash and splash is found (see Figure 3.20), which indicates that gas inertia also influences the impact outcomes. We should notice that the frontier remains almost straight in a large scale (see top panel of Figure 3.20), the gas viscous effect is probably dominant in the impact dynamics as described by the lubrication approximation, however, for a small density ratio, the gas inertial effect becomes no longer negligible and needs to be involved in the theory of splashing (see bottom panel of Figure 3.20).

In the splash regime, two different splash mechanisms are identified: the detachment-splash and the jet-splash. As shown in the bottom panel of Figure 3.21, the frontier is also curved and the deviation from a straight line is larger than the frontier between non-splash and splash, which implies the gas inertial effect plays a more important role in the transition between different splashes.

It can be concluded that both inertial effect and viscous effect influence the drop impact dynamics. The gas viscous effect is probably dominant and the lubrication approximation is valid in a large scale. With the decrease of the gas density, the inertial effect becomes relatively important in the impact dynamics. Our results agrees with the experimental observation reported by Xu *et al.* [2005]. In their works, splash can be completely suppressed by decreasing the pressure of the surrounding gas. In this process, the gas dynamic viscosity μ is constant, only the gas density ρ varies. The suppression of the splash can be at least partially attributed to the decline of the gas inertial effect due to the decrease of the gas pressure.

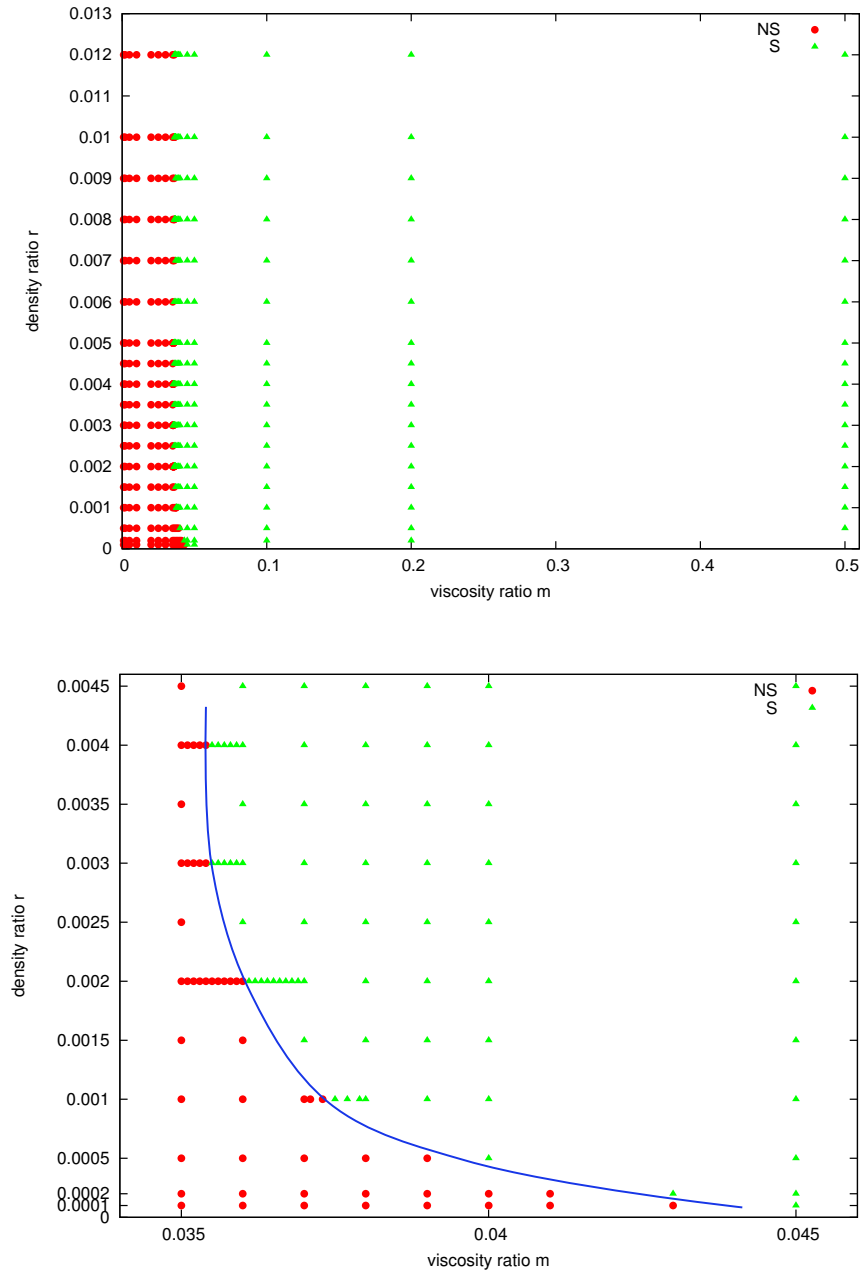


Figure 3.20: Frontier between non-splash and splash. The bottom panel is a zoom of the curved part of the frontier. NS represents non-splash and S represents splash.

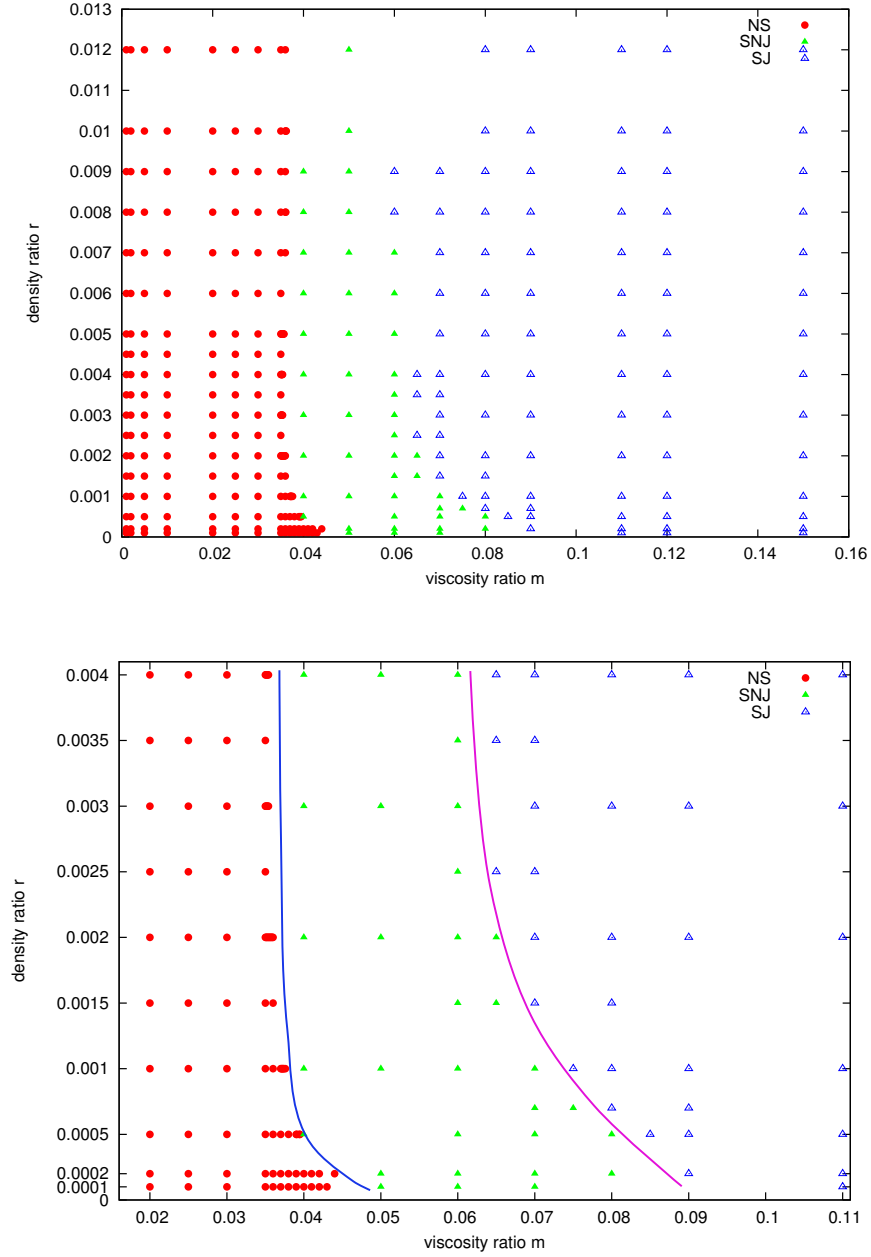


Figure 3.21: Frontier between impact outcomes. The bottom panel is a zoom of the curved part of the frontier. NS represents non-splash, SNJ represents detachment-splash and SJ represents jet-splash.

3.5 Conclusion

In this chapter, we investigated the gas influence in the dynamics of the drop impact onto a solid substrate under the incompressible assumption. The gravity is neglected and the properties of the liquid and the solid are invariant in simulations. The Reynolds number $Re = 1000$ and the Weber number $We = 370$.

Complex dynamics occurs in the gas layer during the impacting process. As the drop approaches the substrate, the gas cushioning effect increases, the bottom part of the drop is decelerated to rest, a dimple is formed and an amount of gas is entrapped subsequently. From that moment, the impact outcome differs with different gas properties. For a small gas density and viscosity, the drop remains on the substrate and forms a shape of poached egg; for a large gas density and viscosity, a splash is formed. Two different splash mechanisms are identified. The drop can first contact the substrate and eject a fast moving liquid sheet, then the sheet is detached from the substrate and forms a “detachment-splash”; Otherwise, a small jet is formed before the contact with the substrate, then the jet is deflected and forms a “jet-splash”, the contact with the substrate occurs before or after the jet deflection.

The lubrication theory involves only the gas viscosity, however, according to our investigations, the transition between non-splash and splash depends not only on the gas viscosity but also the gas density. The transition between detachment-splash and jet-splash performs a similar behaviour. The gas inertial effect is not negligible in the splashing mechanism.

Aerodynamic splashing mechanism

Contents

4.1	Pre-contact dynamics	82
4.1.1	Lubrication approximation in the gas layer	82
4.1.2	Characteristic lengths in the gas layer	85
4.1.3	Ejection of the small jet	91
4.1.4	Lift-up of the small jet	95
4.2	Post-contact dynamics	96
4.2.1	Central bubble entrapment	97
4.2.2	Detachment of the thin liquid sheet	99
4.2.3	Gas entrainment around the contact line	100
4.3	An aerodynamic splashing mechanism	101
4.4	Other effects in the impact dynamics	103
4.4.1	Contact angle effect	103
4.4.1.1	Impact on a totally-nonwetable surface ($\theta = 180^\circ$)	104
4.4.1.2	Impact on a totally-wetable surface ($\theta = 0^\circ$)	105
4.4.1.3	Impact on a partially-wetable surface ($\theta = 30, 60, 120, 150^\circ$)	107
4.4.2	Gas compressibility effect	110
4.5	Conclusion	111

In Chapter §3, two different types of splash were identified as the detachment-splash and the jet-splash. For a detachment-splash, dynamics after the contact with the substrate such as the ejection of thin liquid sheet and the detachment of the sheet are crucial; for a jet-splash, dynamics before the contact such as the creation of the small jet and the lift-up of the jet (instead of retouching the substrate) are important.

In this chapter, under incompressible assumption, we study dynamics before and after contact in the gas layer and propose an aerodynamic splash mechanism. Other effects in the impact dynamics (the contact angle effect, the gas compressibility effect) are also investigated.

4.1 Pre-contact dynamics

Complex dynamics occurs in the gas layer before the contact with the substrate. In this section, we first discuss the lubrication theory, then investigate the dynamics before contact.

4.1.1 Lubrication approximation in the gas layer

For an incompressible Newtonian fluid, if external forces (such as gravity) and surface tension are ignored, Navier-Stokes equations can be written as:

$$\rho \left(\frac{\partial \mathbf{u}}{\partial t} + \mathbf{u} \cdot \nabla \mathbf{u} \right) = -\nabla p + \mu \nabla^2 \mathbf{u} \quad (4.1)$$

$$\nabla \cdot \mathbf{u} = 0 \quad (4.2)$$

where ρ is the fluid density, \mathbf{u} the fluid velocity, p the pressure and μ the fluid viscosity.

In our case of drop impact (see Figure 4.1), the gas cushioning effect is weak at the beginning, the variation of the velocity in the drop is small, the velocity field is almost uniform and keeps the initial velocity U in the vertical direction, therefore, the non linear effect of the liquid inertia (the term $\rho \mathbf{u} \cdot \nabla \mathbf{u}$) can be neglected. The Reynolds number $Re = 1000$, then the viscous effect (the term $\mu \nabla^2 \mathbf{u}$) can also be neglected as compared to the inertial forces, yields:

$$\rho_l \frac{\partial \mathbf{u}_l}{\partial t} = -\nabla p_l \quad (4.3)$$

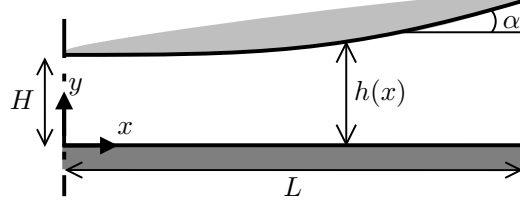


Figure 4.1: Lubrication approximation domain. H is the vertical length scale and L is the horizontal length scale, $H \ll L$. The angle between the interface and the substrate α is small. $h(x)$ is the interface profile of the bottom part of the drop.

The interface $y = h(x)$ is a free surface with absence of the surface tension, then the kinematic boundary condition gives:

$$v_l = \frac{\partial h}{\partial t} + u_l \frac{\partial h}{\partial x}$$

It can be approximated as

$$(u_l, v_l)|_{y=h} = (0, \frac{\partial h}{\partial t}) \quad (4.4)$$

when the drop is “far” from the substrate.

In the gas layer, when the drop approaches the substrate, the thickness of the gas layer decreases and its length scale becomes relatively small as compared to the drop diameter (see Figure 4.1). As a fact of mass conservation and incompressibility, u can be estimated as $L/H \cdot v$, then $u \gg v$ and u is at least of the order of magnitude of the initial velocity U of the drop. We can introduce the lubrication approximation to describe the dynamics in the gas layer.

In two dimensions, note $\mathbf{u} = (u, v)$, rewrite equation (4.1) as:

$$\frac{\partial u}{\partial t} + u \frac{\partial u}{\partial x} + v \frac{\partial u}{\partial y} = -\frac{1}{\rho} \frac{\partial p}{\partial x} + \frac{\mu}{\rho} \left(\frac{\partial^2 u}{\partial x^2} + \frac{\partial^2 u}{\partial y^2} \right) \quad (4.5)$$

$$\frac{\partial v}{\partial t} + u \frac{\partial v}{\partial x} + v \frac{\partial v}{\partial y} = -\frac{1}{\rho} \frac{\partial p}{\partial y} + \frac{\mu}{\rho} \left(\frac{\partial^2 v}{\partial x^2} + \frac{\partial^2 v}{\partial y^2} \right) \quad (4.6)$$

We rescale each variable

$$\bar{x} = \frac{x}{L}, \quad \bar{y} = \frac{y}{H}, \quad \bar{u} = \frac{u}{U}, \quad \bar{v} = \frac{L}{H} \frac{v}{U}, \quad \bar{t} = \frac{U}{L} t, \quad \bar{\rho} = \frac{\rho}{\rho_0}, \quad \bar{\mu} = \frac{\mu}{\mu_0}, \quad \bar{p} = \frac{p}{p_0},$$

introduce a Reynolds number of the gas layer $Re_H = \frac{\rho_0 U H}{\mu_0}$ ¹ and a length scaling factor $\epsilon = \frac{H}{L}$, substitute all rescaled variables into equations (4.5) and (4.6) gives:

$$\epsilon Re_H \left(\frac{\partial \bar{u}}{\partial \bar{t}} + \bar{u} \frac{\partial \bar{u}}{\partial \bar{x}} + \bar{v} \frac{\partial \bar{u}}{\partial \bar{y}} \right) = -\frac{p_0 H^2}{\mu_0 U L} \cdot \frac{1}{\bar{\rho}} \frac{\partial \bar{p}}{\partial \bar{x}} + \epsilon^2 \frac{\bar{\mu}}{\bar{\rho}} \frac{\partial^2 \bar{u}}{\partial \bar{x}^2} + \frac{\bar{\mu}}{\bar{\rho}} \frac{\partial^2 \bar{u}}{\partial \bar{y}^2} \quad (4.7)$$

$$\epsilon Re_H \cdot \epsilon^2 \left(\frac{\partial \bar{v}}{\partial \bar{t}} + \bar{u} \frac{\partial \bar{v}}{\partial \bar{x}} + \bar{v} \frac{\partial \bar{v}}{\partial \bar{y}} \right) = -\frac{p_0 H^2}{\mu_0 U L} \cdot \frac{1}{\bar{\rho}} \frac{\partial \bar{p}}{\partial \bar{y}} + \epsilon^4 \frac{\bar{\mu}}{\bar{\rho}} \frac{\partial^2 \bar{v}}{\partial \bar{x}^2} + \epsilon^2 \frac{\bar{\mu}}{\bar{\rho}} \frac{\partial^2 \bar{v}}{\partial \bar{y}^2} \quad (4.8)$$

The fundamental assumption of the lubrication theory makes $\epsilon \ll 1$ and $\epsilon Re_H \ll 1$ ², all the terms with ϵRe_H , ϵ^2 and ϵ^4 can be neglected:

$$-\frac{p_0 H^2}{\mu_0 U L} \cdot \frac{1}{\bar{\rho}} \frac{\partial \bar{p}}{\partial \bar{x}} + \frac{\bar{\mu}}{\bar{\rho}} \frac{\partial^2 \bar{u}}{\partial \bar{y}^2} = 0 \quad (4.9)$$

$$-\frac{p_0 H^2}{\mu_0 U L} \cdot \frac{1}{\bar{\rho}} \frac{\partial \bar{p}}{\partial \bar{y}} = 0 \quad (4.10)$$

By transferring to original variables, we obtain:

$$-\frac{\partial p}{\partial x} + \mu \frac{\partial^2 u}{\partial y^2} = 0 \quad (4.11)$$

$$-\frac{\partial p}{\partial y} = 0 \quad (4.12)$$

Equations (4.11-4.12) indicate that the vertical velocity component (v) can be neglected, which is relatively small as compared to the horizontal component (u); the velocity varies generally in the vertical direction, the horizontal velocity derivative can be neglected and the pressure p can be considered constant in the vertical direction.

On the interface, the stress and the velocity are continuous across the interface (dynamic boundary conditions)³:

$$\begin{aligned} \mu_l \frac{\partial u_l}{\partial y} &= \mu_g \frac{\partial u_g}{\partial y}, \\ u_l &= u_g, \quad v_l = v_g. \end{aligned}$$

Considering the liquid boundary condition (4.4), yields:

$$(u_g, v_g)|_{y=h} = (0, \frac{\partial h}{\partial t}) \quad (4.13)$$

¹In this section, U denotes the initial vertical velocity of the drop, it is taken as the scale of the velocity.

²As mentioned in the book of Frene *et al.* [1997], generally, for a viscous thin film, ϵ is of the order of 10^{-3} and ϵRe_H is of the order of 10^{-4} .

³Strictly, the continuous conditions are applied in the tangential and normal direction. Since the interface is almost horizontal (α is small in Figure 4.1), we use x, y directions.

The solid substrate is no-slip:

$$(u_g, v_g)|_{y=0} = (0, 0) \quad (4.14)$$

We integrate equation (4.11) in the y -direction twice with the two boundary conditions (4.13 - 4.14) and obtain:

$$u_g = \frac{1}{2\mu_g} \frac{\partial p_g}{\partial x} (y^2 - hy) \quad (4.15)$$

Substitute u_g into the continuity equation (4.2), integrate it in the y -direction with the two boundary conditions (4.13 - 4.14) and obtain the incompressible Reynolds lubrication equation in the gas layer:

$$\frac{\partial h}{\partial t} = \frac{\partial}{\partial x} \left(\frac{1}{12\mu_g} \frac{\partial p_g}{\partial x} h^3 \right) \quad (4.16)$$

4.1.2 Characteristic lengths in the gas layer

When the drop approaches the substrate, the gas cushioning effect decelerates the bottom part of the drop continuously. At a certain moment, the interface comes to rest and the thickness of gas layer h_e is a characteristic length and it is close to the height of the central entrapped bubble. Here, h_e takes the value on the symmetry axis ($r = 0$, see Figure 4.2 (a)). The drop continues to fall and contacts the substrate. The radius of the first contact point r_e is another characteristic length and it is close to the radius of the central entrapped bubble (see Figure 4.2 (b)).

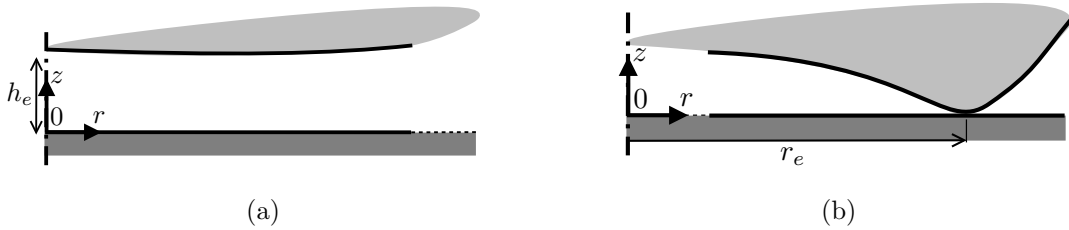


Figure 4.2: Characteristic lengths in the gas layer: (a) the thickness of the gas layer on the symmetry axis h_e and (b) the radius of the first contact point r_e .

In the gas layer, the lubrication equation (4.11) indicates that $-\frac{\partial p}{\partial x}$ has the same scale as $\mu \frac{\partial^2 u}{\partial y^2}$, then the lubrication pressure p_{lub} :

$$p_{lub} \sim \frac{\mu_g U D}{h_e^2} \quad (4.17)$$

In the drop, for a two-dimensional system, the governing equation (4.3) can be solved by a complex analytical method (see Smith *et al.* [2003]).

Rewrite equation (4.3) as:

$$\rho \frac{\partial u_l}{\partial t} = -\frac{\partial p_l}{\partial x}, \quad \rho \frac{\partial v_l}{\partial t} = -\frac{\partial p_l}{\partial y} \quad (4.18)$$

Since $\nabla^2 p_l \sim 0$ ⁴, we construct a holomorphic complex function $p_l + iq_l$ in the complex plane $z = x + iy$. Cauchy's integral theorem gives:

$$\frac{d}{dz}(p_l + iq_l) = \frac{1}{2\pi i} \int_{-\infty}^{\infty} \frac{[p_{l\xi}(\xi, 0, t) + iq_{l\xi}(\xi, 0, t)]d\xi}{(\xi - z)} \quad (4.19)$$

Evaluate the imaginary parts at $y = 0$,

$$\frac{\partial p_l}{\partial y}(x, 0, t) = \frac{1}{\pi} p.v. \int_{-\infty}^{\infty} \frac{p_{l\xi} d\xi}{(\xi - x)} = -\mathcal{H}\left(\frac{\partial p_l}{\partial x}\right) \quad (4.20)$$

where $p.v.$ is the Cauchy principal value.

Then, we can relate $\frac{\partial p_l}{\partial y}$ with $\frac{\partial p_l}{\partial x}$ by a Hilbert transform,

$$\rho \frac{\partial v_l}{\partial t} = \mathcal{H}\left(\frac{\partial p_l}{\partial x}\right) \quad (4.21)$$

thus, the liquid pressure can be estimated:

$$p_l \sim \frac{\rho_l U L}{\tau} \quad (4.22)$$

where $L = \sqrt{D h_e}$ is the local horizontal length scale at the bottom part of the drop, $\tau = h_e/U$.

To deform the drop interface (reverse the interface curvature), the lubrication pressure in the gas layer p_{lub} must be sufficient to decelerate the drop from a high impact velocity to zero, p_{lub} becomes comparable to the liquid pressure p_l . Then $p_{lub} \sim p_l$, we obtain the thickness of the gas layer:

$$h_e \sim D \cdot St^{\frac{2}{3}} \quad (4.23)$$

where

$$St = \frac{\mu_g}{\rho_l U D} \quad (4.24)$$

is the Stokes number. It compares the interaction between the gas viscous effect and the liquid inertial effect.

⁴Make the divergence on the two sides of equation (4.3): $\nabla \cdot (\rho_l \frac{\partial \mathbf{u}_l}{\partial t}) = -\nabla \cdot (\nabla p_l)$, then $\nabla^2 p_l \sim -\rho_l \frac{\partial(\nabla \cdot \mathbf{u}_l)}{\partial t}$. With the continuity equation (4.2), yields: $\nabla^2 p_l \sim 0$.

Suppose the substrate becomes “invisible” and the drop penetrates into the substrate, the radius of the first contact point r_e can be estimated as:

$$r_e \sim \sqrt{DU\tau} \quad (4.25)$$

where the time scale $\tau = h_e/U$.

Thus,

$$r_e \sim \sqrt{Dh_e} \sim D \cdot St^{\frac{1}{3}} \quad (4.26)$$

The area of the gas layer (or of the central entrapped bubble) can also be estimated:

$$S_e \sim h_e \cdot r_e \sim D^2 \cdot St \quad (4.27)$$

As shown in Figures 4.3(a), 4.4(a) and 4.5(a), in a large range of the Stokes number, the characteristic lengths of the gas layer take the same scale as predicted by the lubrication approximation ($h_e \sim St^{\frac{2}{3}}$, $r_e \sim St^{\frac{1}{3}}$, $S_e \sim St$). For extremely large or small viscosity ratios⁵, the characteristic lengths deviate from the prediction of the lubrication approximation.

Moreover, the variation of the characteristic lengths with the density ratio is slight (see Figures 4.3(b), 4.4(b) and 4.5(b)), which indicates that the gas inertial effect is possibly not a significant factor to the dynamics in the gas layer and the lubrication approximation is valid before contact. The deviation of the characteristic lengths from a constant is also observed for extremely large or small viscosity ratios.

It should be noticed that the characteristic lengths h_e, r_e are obtained before the ejection and the lift-up of the small jet, then the role of the gas viscous and inertial effects in these dynamics is not clear with the lubrication approximation.

⁵In simulations, the viscosity ratio $m = \mu_g/\mu_l$ and the density ratio $r = \rho_g/\rho_l$ are introduced, then the Stokes number: $St = \frac{m\mu_l}{\rho_l U D} = \frac{m}{Re} = 0.001m$. The viscosity ratio is proportional to the Stokes number.

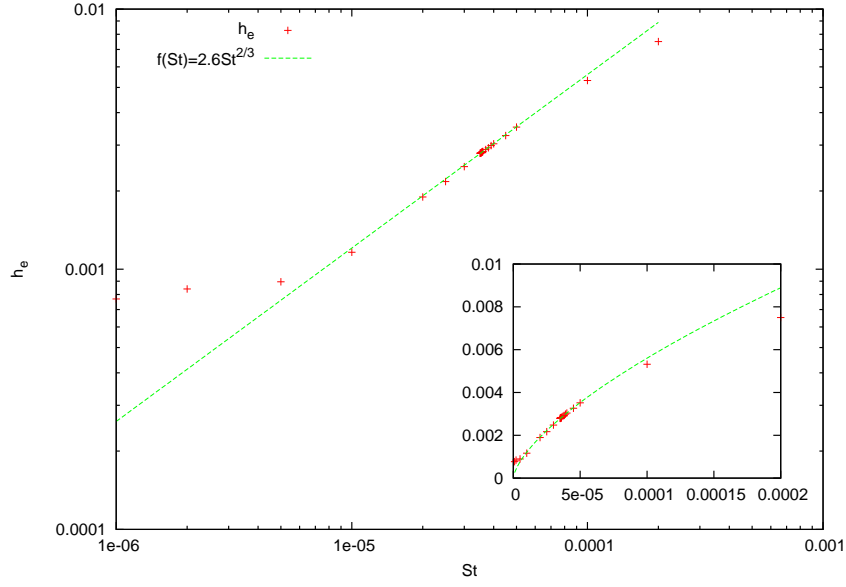
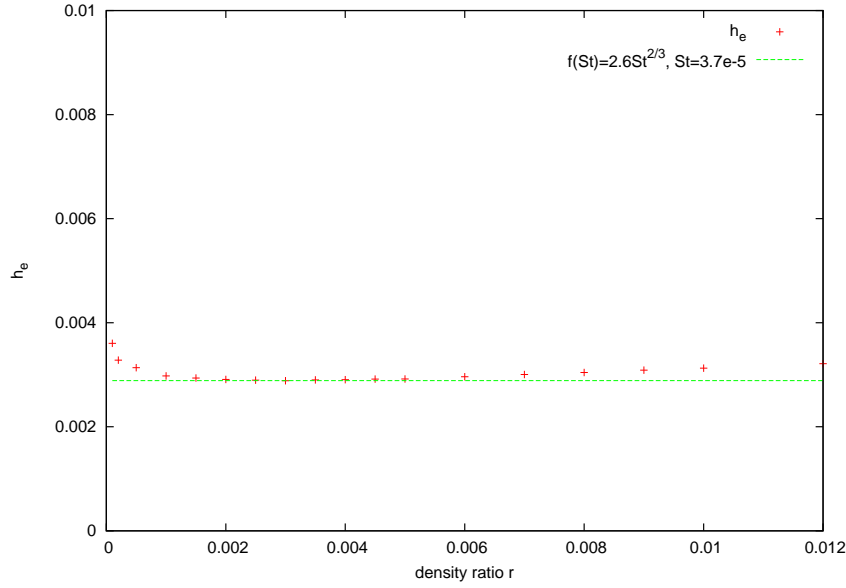
(a) h_e versus the Stokes number St (b) h_e versus the density ratio r

Figure 4.3: Thickness of the gas layer h_e . (a) h_e versus Stokes number St in the logarithmic scale. Symbols represents simulation results. Inset shows the normal scale. (b) h_e versus the density ratio r for $St = 3.7 \times 10^{-5}$. Dash line represents the scaling law $h_e = 2.6St^{\frac{2}{3}}$.

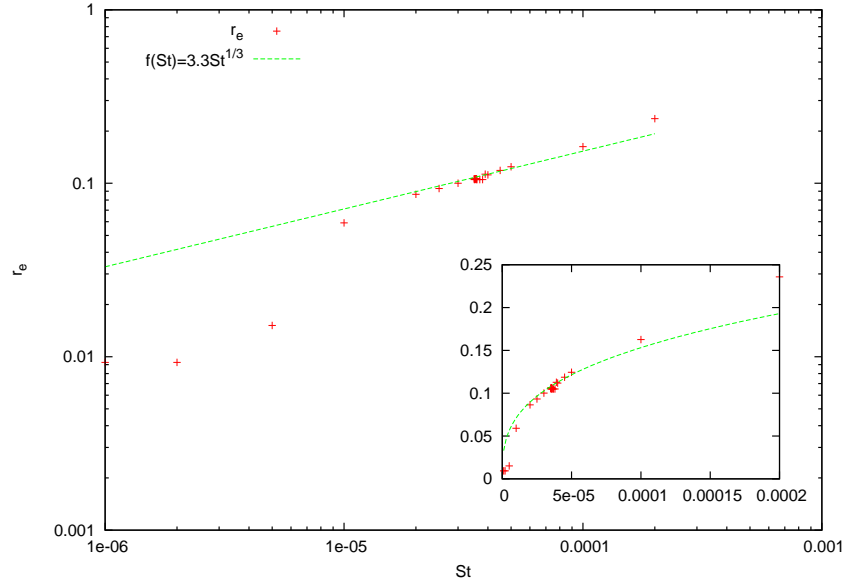
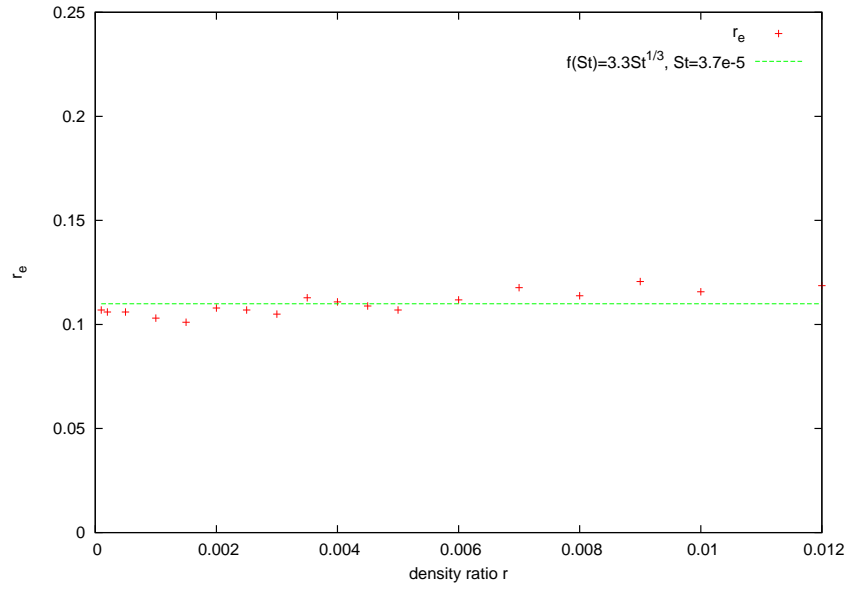
(a) r_e versus the Stokes number St (b) r_e versus the density ratio r

Figure 4.4: Radius of the first contact point r_e . (a) r_e versus Stokes number St in the logarithmic scale. Symbols represents simulation results. Inset shows the normal scale. (b) r_e versus the density ratio r for $St = 3.7 \times 10^{-5}$. Dash line represents the scaling law $r_e = 3.3St^{\frac{1}{3}}$.

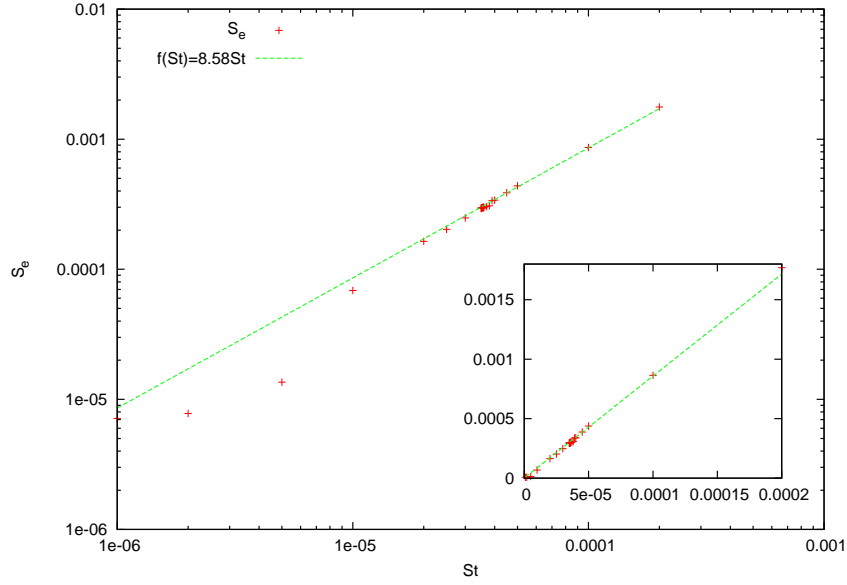
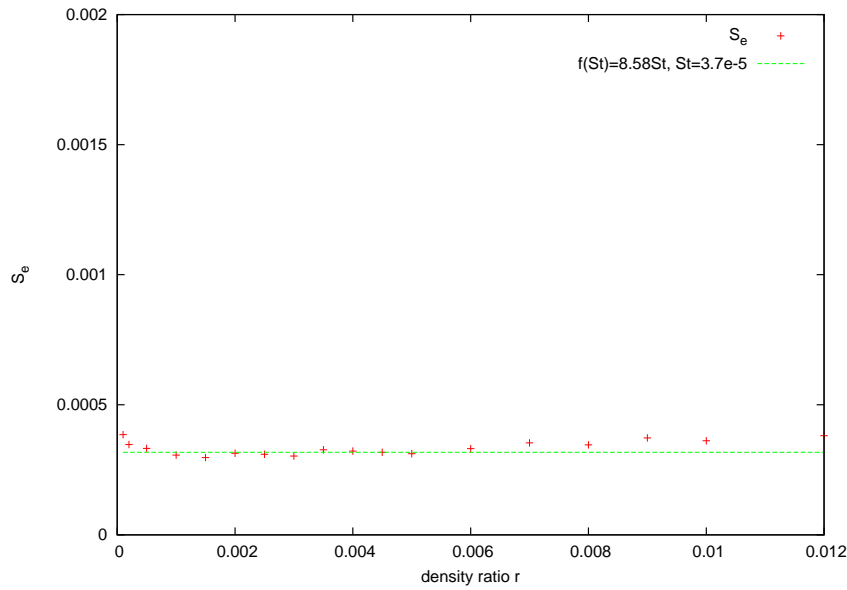
(a) S_e versus the Stokes number St (b) S_e versus the density ratio r

Figure 4.5: Area of the central entrapped bubble S_e . (a) S_e versus Stokes number St in the logarithmic scale. Symbols represents simulation results. Inset shows the normal scale. (b) S_e versus the density ratio r for $St = 3.7 \times 10^{-5}$. Dash line represents the scaling law $S_e = 8.58St$.

4.1.3 Ejection of the small jet

For a jet-splash, a small jet is ejected before the contact with the substrate and it is the origin of a splash. Under the lubrication approximation, the gas pressure is constant in the y -direction, then $p_g \sim p(x)$. As shown in Figure 4.6⁶, the maximum gas pressure is located in the smallest-thickness area and moves from the center to the corner-like interface zone.

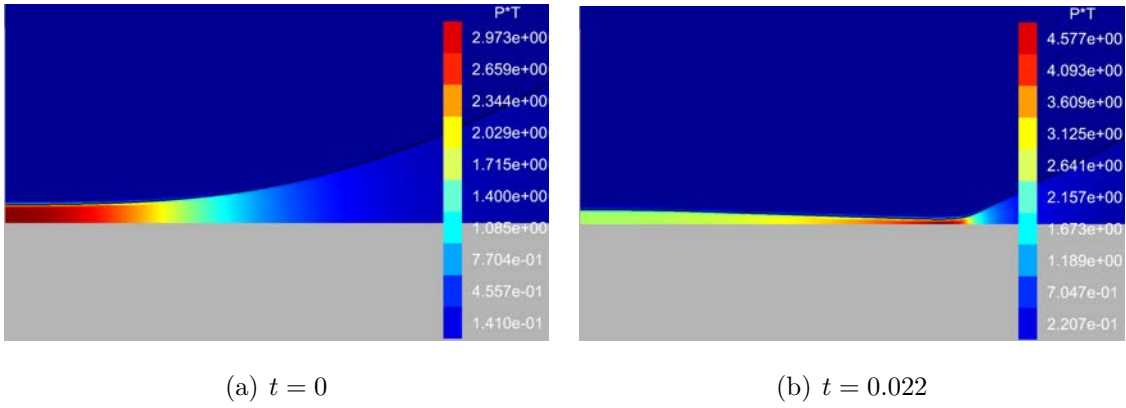


Figure 4.6: Snapshots of the gas pressure field, $r = 0.001, m = 0.15$.

We extract the pressure profile at the height of $h = 0.5h_{min}$ in the gas layer at different moments before the contact for different outcomes (see Figure 4.7). The location of p_{gmax} moves towards the outside.

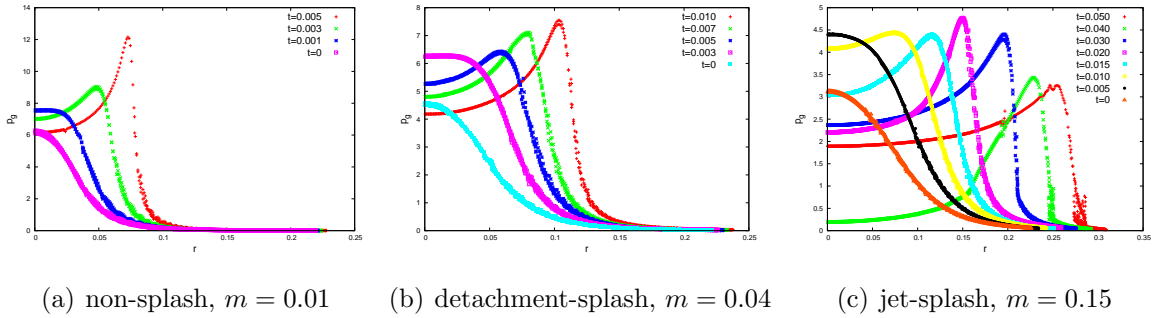


Figure 4.7: Pressure profile at the height of $h = 0.5h_{min}$ in the gas layer at different moments before contact for three types of outcomes: (a) non-splash, (b) detachment-splash and (c) jet-splash.

⁶With absence of gas, the drop contacts the substrate at $t_{th} = h_0/U_0 = 0.1$ in simulations, in the coming section, we rescale the time with $t_r = t - t_{th}$ and drop the subscript ' r '.

As discussed in the section §4.1.2, in the lubrication gas layer, the gas pressure takes the same scale as the liquid pressure,

$$p_g \sim p_l \sim \frac{\rho_l U L}{\tau} \sim \rho_l U^2 \sqrt{D} h_{min}^{-\frac{1}{2}} \sim h_{min}^{-\frac{1}{2}} \quad (4.28)$$

As shown in Figure 4.8, for a non-splash and a detachment-splash, p_{gmax} obeys the scaling law $p_{gmax} \sim h_{min}^{-\frac{1}{2}}$; whereas, for a jet-splash with a large viscosity ratio, the scaling $h_{min}^{-\frac{1}{2}}$ is only satisfied at the very beginning. p_{gmax} keeps nearly constant until the jet ejection and then it decreases. It implies that a part of the gas aerodynamic energy contributes to the jet ejection dynamics.

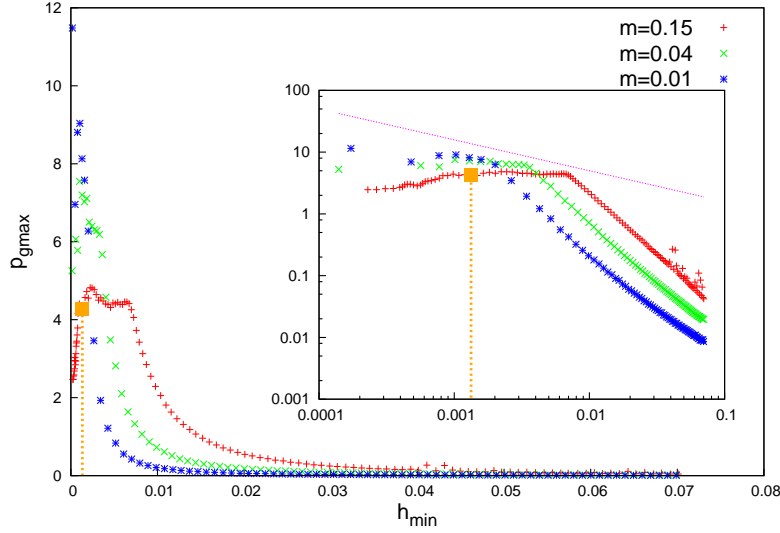


Figure 4.8: p_{gmax} as a function of h_{min} before the contact. Density ratio $r = 0.001$, three viscosity ratios $m = 0.01, 0.04, 0.15$ correspond to the regime of non-splash, detachment-splash and jet-splash respectively. Inset shows the logarithmic scale and the dotted line is the scaling $h_{min}^{-\frac{1}{2}}$. The vertical dotted line indicates the jet ejection for a jet-splash.

Figure 4.9 shows the velocity evolution at the h_{min} -point on the interface. When the drop approaches, the gas layer becomes thinner. As a matter of gas incompressibility and mass conservation, gas evacuates towards the outside. It accelerates the drop interface locally and supplies a large horizontal velocity component u to the drop; meanwhile, the drop is decelerated by the gas cushioning effect, the vertical velocity component v decreases continuously until zero. After the ejection of the small jet, the kinematic energy in the drop is transferred to the small jet, then the u component decreases too.

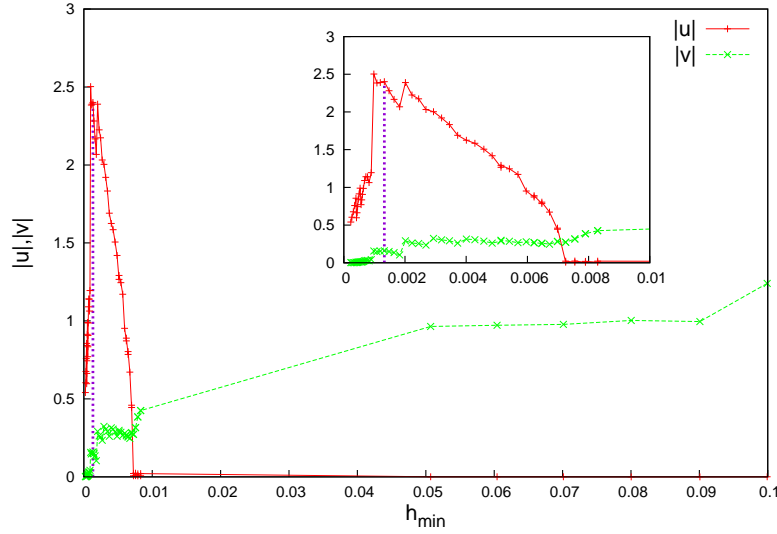


Figure 4.9: Absolute value of the velocity components u, v at the h_{min} -point as a function of h_{min} before the contact for a jet-splash case $r = 0.001, m = 0.15$. Inset shows a zoom near the contact moment. The vertical dotted line indicates the jet ejection.

As shown in Figure 4.10, at the theoretical contact moment $t = 0$, gas has a velocity four times larger than the initial drop velocity U , while the drop velocity remains at U and its horizontal component is small. After a short time interval $\Delta t = 0.022$, the liquid velocity becomes almost horizontal at the bottom of the drop and a velocity concentration is formed in the corner-like area.

In the corner-like area, the liquid moves fast towards the gas, instabilities (such as a Rayleigh-Taylor instability) exists probably on the interface. As shown in Figure 4.11, a large pressure gradient exists at the corner, it is favourable to the jet ejection. A possible resistance comes from the surface tension, the jet ejection can be considered as a competition between the surface tension and the pressure gradient.

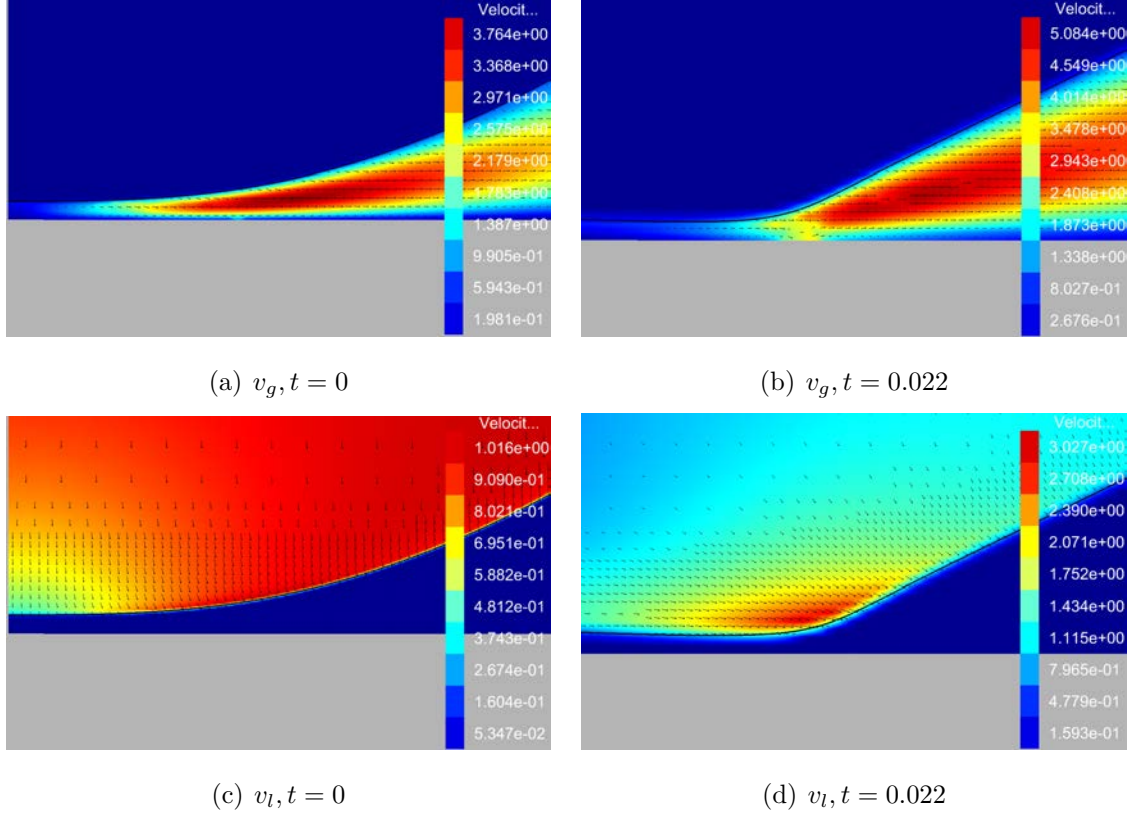


Figure 4.10: Snapshots of velocity fields. $r = 0.001, m = 0.15$.

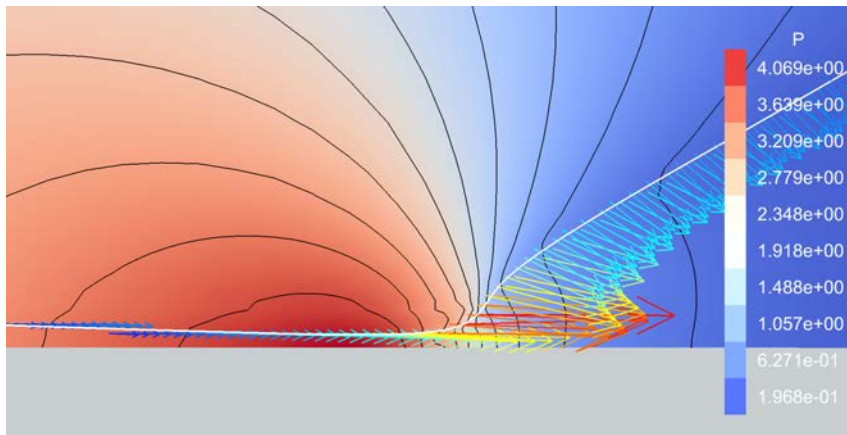


Figure 4.11: Pressure and velocity fields just before the small jet ejection. $t = 0.027, r = 0.001, m = 0.15$. Coloured arrows represent the velocity field on the interface, the color gradient of arrows represents the magnitude of the velocity. The isolines of pressure show that a strong pressure gradient exists at the corner, where the small jet will be ejected.

4.1.4 Lift-up of the small jet

Subsequent to the ejection, the small jet moves horizontally with a large velocity (see Figure 4.12) and gas along the two sides of the jet moves also fast, then instabilities (such as Kelvin-Helmholtz instability) exist probably on the fast-moving jet.

The jet can touch the substrate again or lift up. To lift up the jet, an opposing force is necessary, the only possible force of the jet bending is the gas aerodynamic force caused by the gas dynamic pressure $\rho_g v_g^2$ (see Figure 4.13). It should be mentioned that the lift-up of the jet occurs very quickly after the jet ejection, the time interval for the horizontal moving of the jet is quite small.

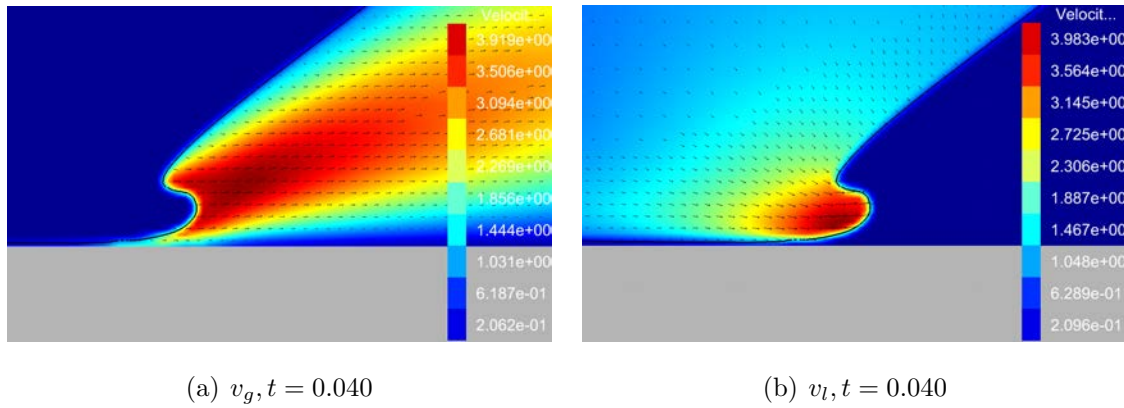


Figure 4.12: Snapshots of velocity fields. $r = 0.001, m = 0.15$.

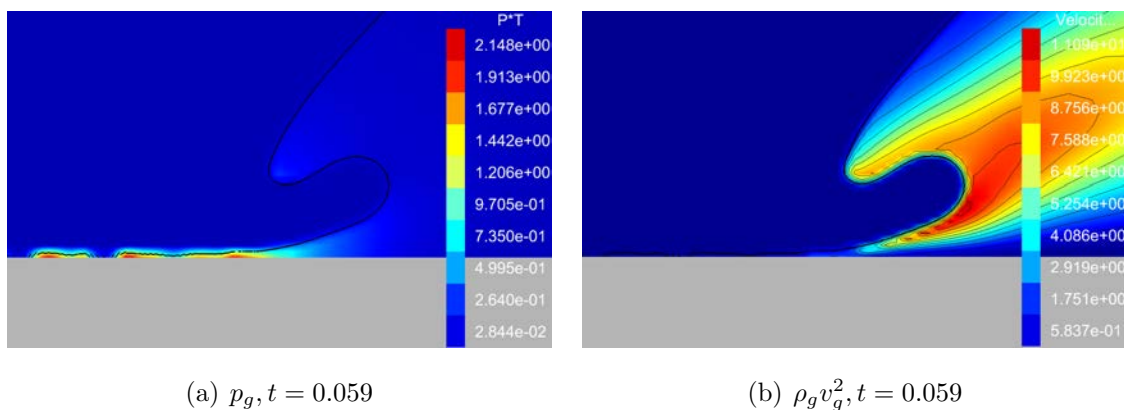


Figure 4.13: Snapshots of pressure fields. $r = 0.001, m = 0.15$. Isolines present the distribution of $\rho_g v_g^2$.

4.2 Post-contact dynamics

For both non-splash and detachment-splash cases, the drop contacts the substrate first. Subsequent to the direct contact, a fast-moving thin liquid sheet is ejected along the solid surface and the detachment of the thin liquid sheet originates the splash (see Figure 4.14).

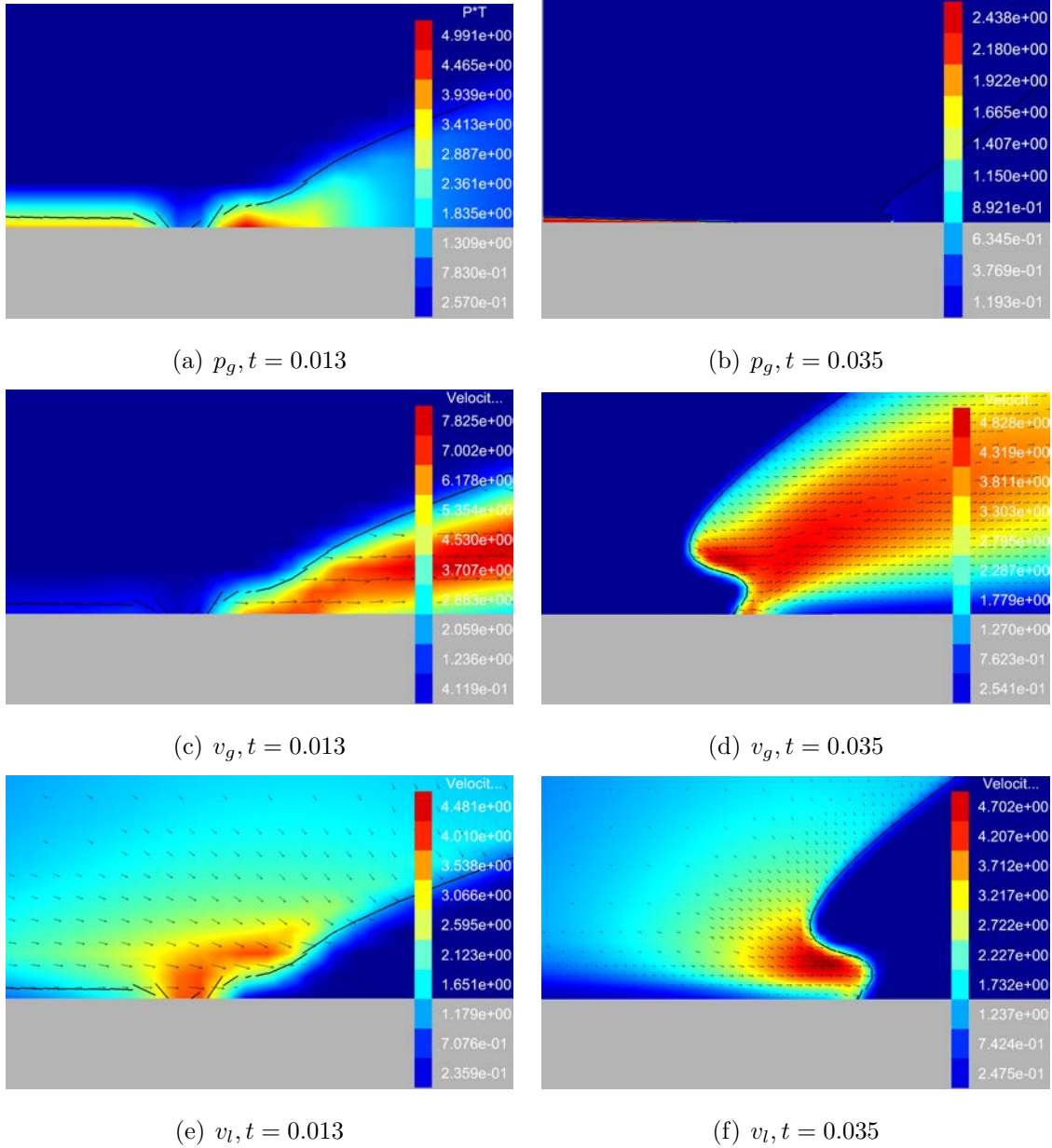


Figure 4.14: Snapshots of pressure and velocity fields of a detachment-splash case, $r = 0.001$, $m = 0.04$.

4.2.1 Central bubble entrapment

As a consequence of the direct contact, a bubble is formed under the drop in the center. Central bubble entrapment is often reported in the literature in the dynamics of the drop impact on solid [Duchemin and Josserand, 2012, Hicks and Purvis, 2010, Mehdi-Nejad *et al.*, 2003, Thoroddsen *et al.*, 2005, 2009]. As shown in Figure 4.15, it is observed in both non-splash and detachment-splash cases in our simulations ⁷. It should be noticed that the central bubble is far from the thin liquid sheet during the sheet detachment dynamics.



(a) Non-splash, $m = 0.01$



(b) Detachment-splash, $m = 0.04$

Figure 4.15: Snapshots of the central entrapped bubble at $t = 0.060$. $r = 0.001$. Colour gradient represents the gas pressure.

As shown in Figure 4.16, the height of the central bubble on the symmetry axis ($r = 0$) h_{r0} has a tendency of decreasing. For the non-splash, the fluctuation is “strong” at the beginning; whereas, for the detachment-splash, the viscous dissipation smooths the fluctuation. The variation of h_{r0} is negligible as compared to the thickness of the thin liquid sheet.

The radius of the central bubble has a small variation at the very beginning then becomes constant (see Figure 4.17). As shown in Figure 4.18, during the drop impact, the central bubble does not extend in the horizontal direction, a capillary wave is generated on the interface of the central bubble, but the oscillation is relatively small. The central

⁷In the jet-splash, a central entrapped bubble is also observed.

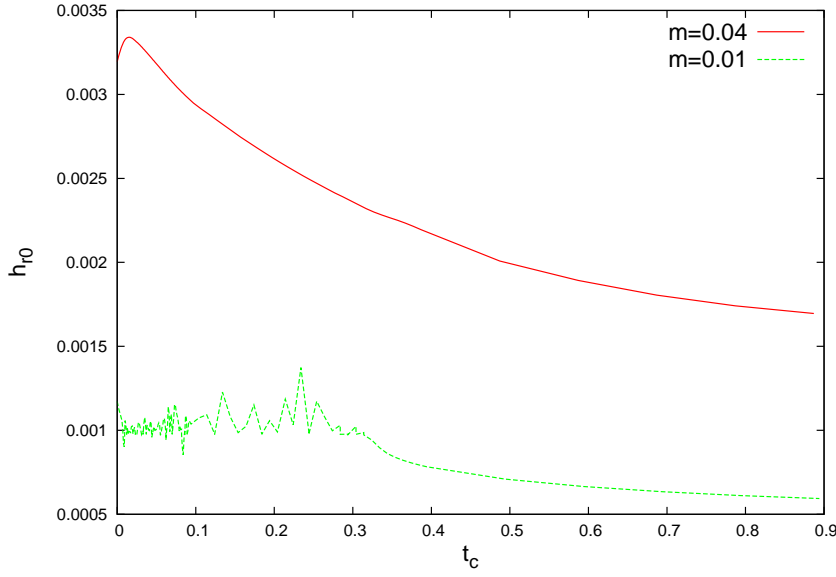


Figure 4.16: Height of the central entrapped bubble on the symmetry axis ($r = 0$) h_{r0} as a function of the rescaled time t_c , $r = 0.001$. Time is rescaled by $t_c = t - t'_c$, t'_c is the contact time in simulations: $m = 0.04, t'_c = 0.113$; $m = 0.01, t'_c = 0.106$.

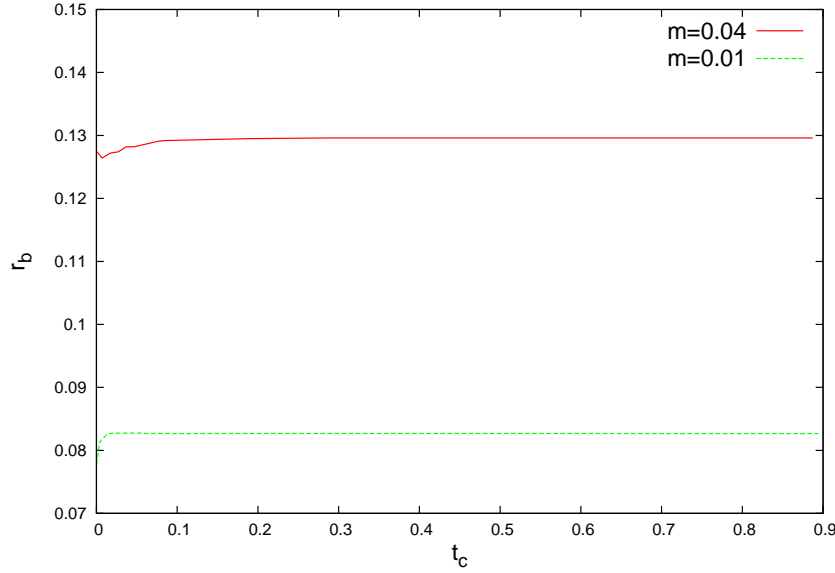
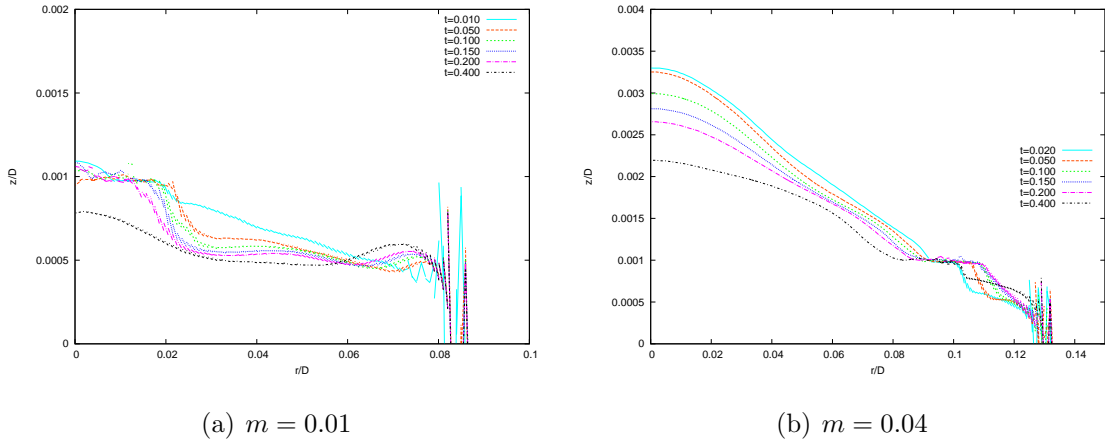
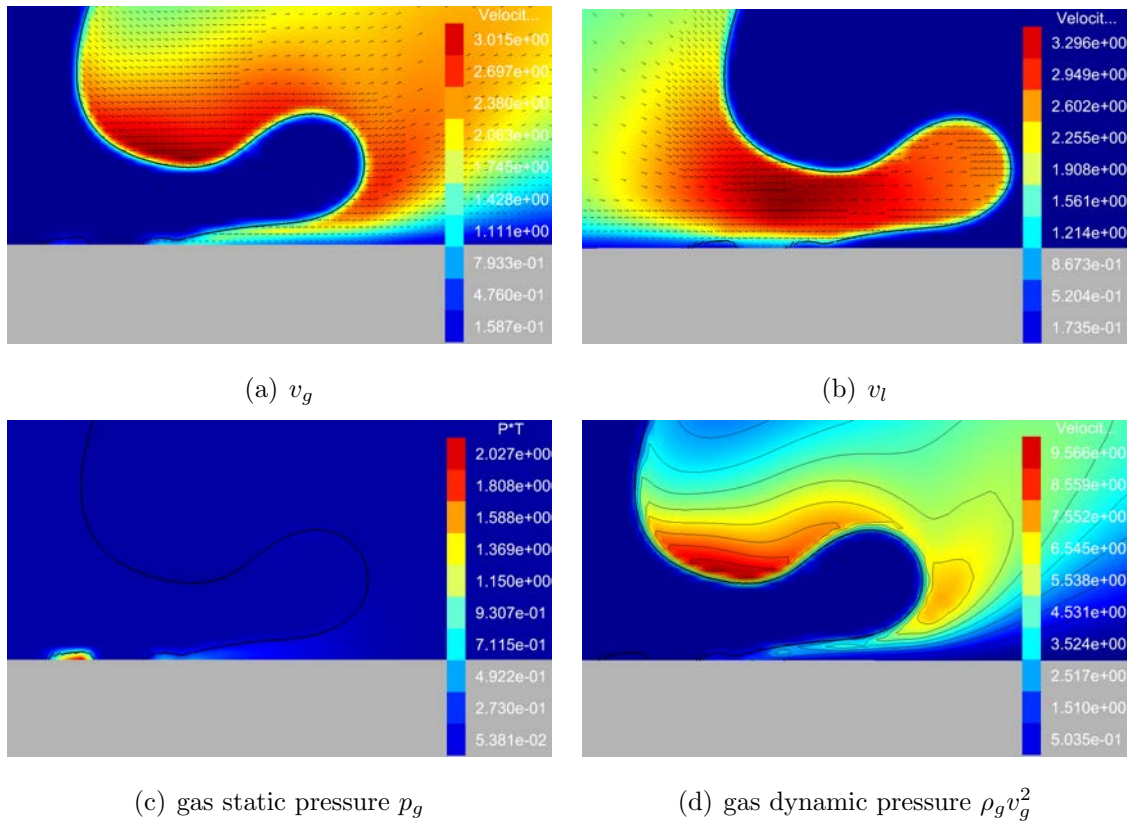


Figure 4.17: Radius of the central entrapped bubble r_b as a function of the rescaled time t_c , $r = 0.001$. Time is rescaled by $t_c = t - t'_c$, t'_c is the contact time in simulations: $m = 0.04, t'_c = 0.113$; $m = 0.01, t'_c = 0.106$.

bubble is trapped in the center and far from the sheet detachment zone, thus, it is probably not important to the splash formation and the dynamics at the rim of the thin liquid sheet is crucial.

Figure 4.18: Profile evolution of the central entrapped bubble, $r = 0.001$.

4.2.2 Detachment of the thin liquid sheet

Figure 4.19: Liquid sheet detachment caused by the gas aerodynamic force (scaled by the gas dynamic pressure $\rho_g v_g^2$) at $t = 0.09$, $r = 0.001$, $m = 0.04$.

As discussed in the section §4.2.1, the splash is probably related to the dynamics at the rim of the fast-moving sheet. The existence of the solid substrate creates a velocity

boundary layer in the sheet (see Figure 4.14 (f) and Figure 4.19 (b)). The upper part of the sheet moves fast and instabilities (such as a Rayleigh-Taylor instability) exists probably at the rim of the sheet.

A small salient can be formed at the upper corner of the rim, it can be considered that the rim of the jet is detached from the substrate. An opposite force is necessary to maintain the detached rim and lift up the rim opposite to the substrate. The only possible force is the gas aerodynamic force caused by the dynamic pressure (scaled by $\rho_g v_g^2$) (see Figure 4.19).

4.2.3 Gas entrainment around the contact line

An interesting phenomenon is observed in simulations for both detachment-splash and jet-splash. When the jet moves fast towards the outside, a part of the lower interface of the jet contacts again the substrate just in front of the contact line, an amount of gas is entrapped and a local contact is created (see Figure 4.20). Eventually, a series of small bubbles are formed behind the contact line.

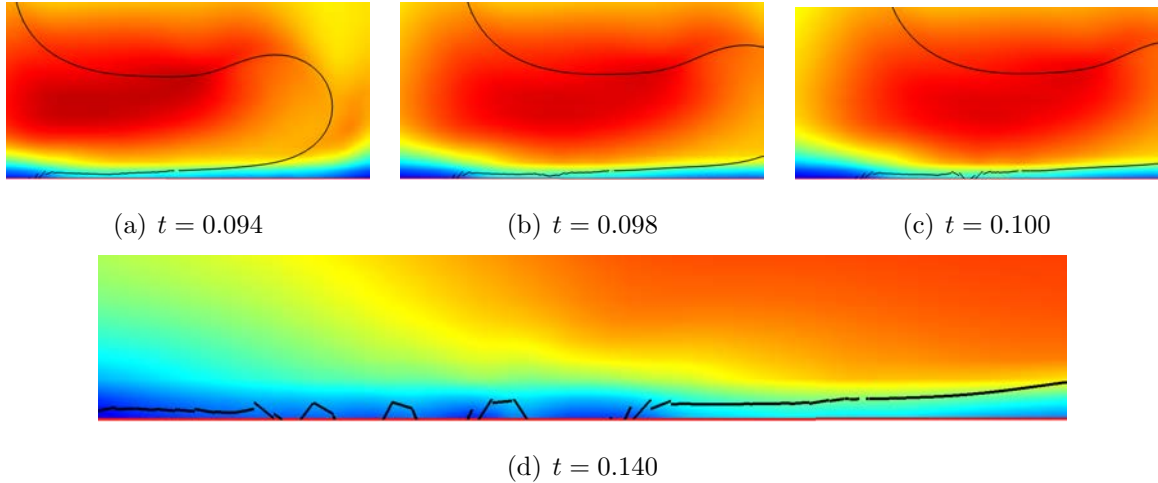


Figure 4.20: Snapshots of the gas entrainment at $r = 0.003, m = 0.037$. A part of the detached interface in front of the contact line touches the substrate again and an amount of gas is entrapped. Colour gradient represents the magnitude of the velocity. Red line denotes the solid surface.

The gas entrainment phenomenon is observed in experiments by Driscoll *et al.* [2010] (namely “bubble entrainment”) and Palacios *et al.* [2012] (namely “bubble entrapment”).

This phenomenon can be explained by the aerodynamic mechanism. As shown in Figure 4.20, gas has a small velocity under the jet in the zone of this dynamics. The gas aerodynamic force (scaled by $\rho_g v_g^2$) is not sufficient to support a part of the interface, then that part of the interface falls and touches the substrate again.

4.3 An aerodynamic splashing mechanism

As a matter of mass conservation, we obtain an approximation of the radius of the wetted area after impact $r_w = 1.2\sqrt{DUt}$, where D is the diameter of the drop and U is the impacting velocity.

Figure 4.21 shows the interface profile in a rescaled framework, where r is rescaled by $r - 1.2\sqrt{DUt}$. At the early stage of impact, the trajectory of the rim of the jet shows a similar behaviour as approximated by an exponential law (see the red dotted line in the right panel of Figure 4.21), it can be also considered as an approximation of the profile of the jet.

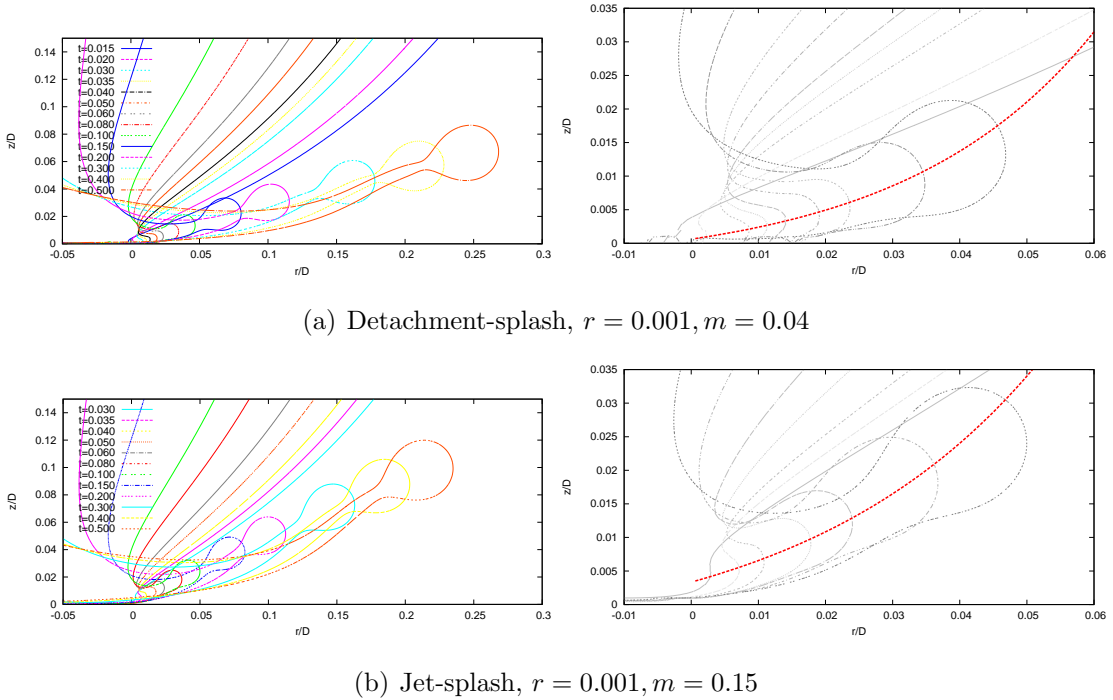


Figure 4.21: Rescaled interface profile for two types of splashes in time. r is rescaled by $r - 1.2\sqrt{DUt}$. Right panel shows approximations of the trajectory of the rim of the jet.

It can be concluded that the splash originates from the ejecta (the small jet of a jet-splash or the thin liquid sheet of a detachment-splash). Gas properties influence the dynamics of the ejecta and two mechanisms of splash exist. With a large gas density and viscosity, a small jet is formed before the contact and it is immediately lifted up by the gas aerodynamic force and forms a jet-splash (see Figure 4.22 (a)); by decreasing the gas density or viscosity, the drop contacts first the substrate and ejects immediately a fast-moving thin liquid sheet, then the sheet is detached from the substrate by the gas aerodynamic force and developed to a detachment-splash (see Figure 4.22 (b)); with further decreasing, the gas aerodynamic force is not sufficient, then the liquid sheet remains on the substrate and the splash is eliminated (see Figure 4.22 (c)).

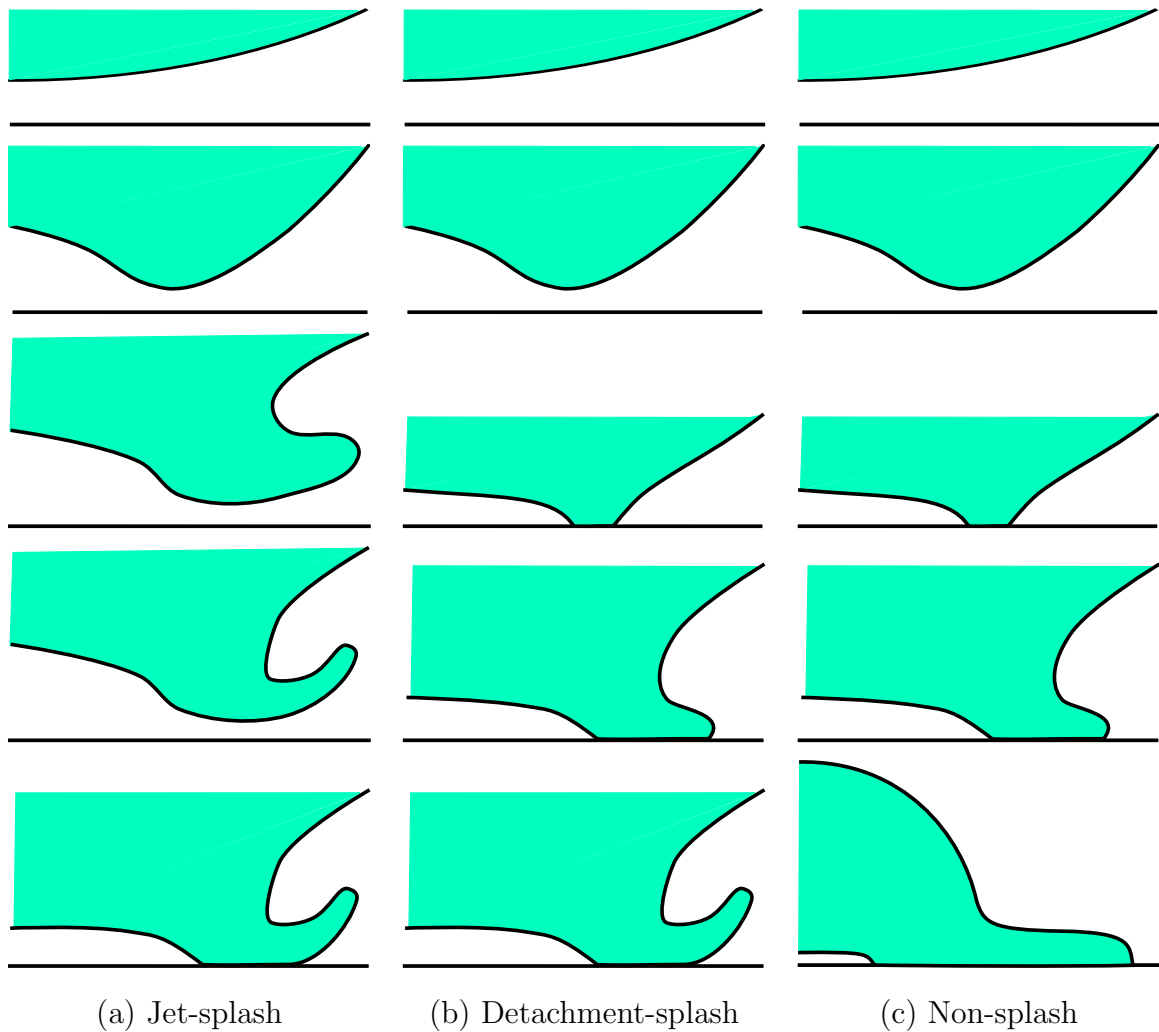


Figure 4.22: Sketch of the splash mechanism.

4.4 Other effects in the impact dynamics

Drop splashing is complex and a host of physical dynamics are involved. Here, we discuss the effect of the contact angle and the gas compressibility effect in order to verify the assumptions established in our aerodynamic mechanism.

4.4.1 Contact angle effect

Contact angle is a reflection of the coexistence of the three phases and it is associated to a triple-phase contact line. The contact angle discussed here is defined as the angle in the liquid phase between the liquid-gas interface and the solid substrate. The contact angle can take different values according to the state of the system. If the system is in an equilibrium state, we get a static contact angle θ_e (as illustrated in Figure 2.1) and it is a proper physical property of the triple-phase system; however, if the system is dynamic (for instance, a drop slipping on an inclined surface, drop evaporation), contact angles varies with many factors such as the velocity of the moving contact line. For a drop slipping on an inclined surface, a receding and an advancing contact angle are observed and they take different values. We should mention that all these angles are measured macroscopically, or saying they are apparent contact angles. The contact angle in a microscopic level can be different from the macroscopic angle as a result of the roughness of the substrate.

Solid substrates can be divided into two types by the value of the contact angle: hydrophobic substrate ($\theta > 90^\circ$) and hydrophilic substrate ($\theta < 90^\circ$). In Chapters §3 and §4, discussions are based on a threshold contact angle ($\theta = 90^\circ$) and we find that gas plays a crucial role in the drop impact, two mechanisms of splash are identified considering whether a jet is formed before the contact with the substrate. The contact angle is taken into account from the moment of contact, which implies that the value of the contact angle could influence the splashing dynamics.

Here, the effect of the contact angle on splashing is investigated, we take the same configuration as in Chapter §3 (see Figure 3.1) and impose a static contact angle on the solid surface. Impacts in the non-splash regime and two different splash regimes are simulated. A totally-nonwetable surface (super hydrophobic), a totally-wetable surface (super hydrophilic) and partially-wetable surfaces (including both hydrophobic and hydrophilic surfaces) are considered. We take six combinations of the density ratio

r and the viscosity ratio m : $(r, m) = (0.001, 0.01)$, $(r, m) = (0.004, 0.01)$ (non-splash at $\theta = 90^\circ$); $(r, m) = (0.001, 0.04)$, $(r, m) = (0.004, 0.04)$ (detachment-splash at $\theta = 90^\circ$); $(r, m) = (0.001, 0.15)$, $(r, m) = (0.004, 0.15)$ (jet-splash at $\theta = 90^\circ$).

The only difference with the simulations of $\theta = 90^\circ$ in Chapter §3 is the contact angle applied on the substrate, so the simulations with the same density and viscosity ratios perform same dynamics before the contact with the substrate. With absence of gas, the drop contacts the substrate at $t_{th} = h/U_0 = 0.1$, we rescale the time by $t = t - t_{th}$.

4.4.1.1 Impact on a totally-nonwetable surface ($\theta = 180^\circ$)

As shown in Figure 4.23, a jet-splash is always observed. On a super-hydrophobic surface, both liquid and substrate tend to prevent physical contacts. Even if a point-contact occurs, the contact is not stable and they separate from each other immediately.

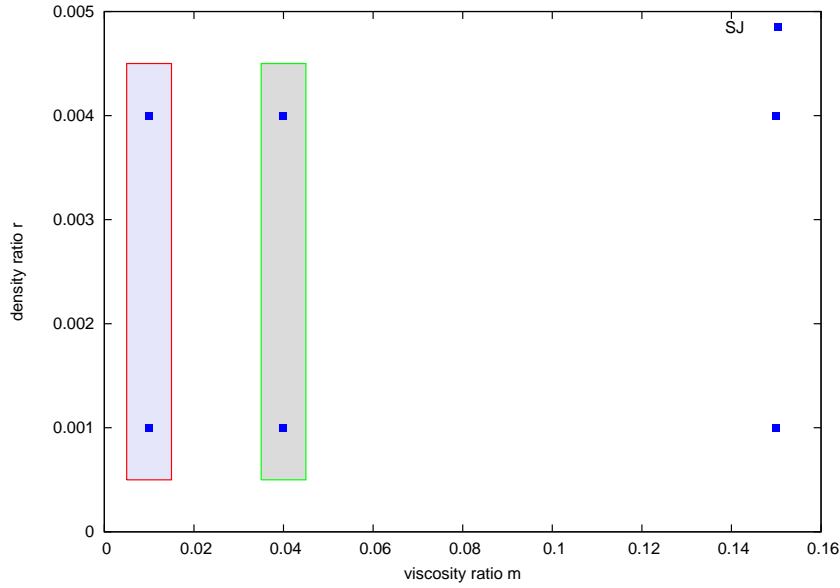


Figure 4.23: Impact outcomes for $\theta = 180^\circ$. A jet-splash is always observed. SJ denotes jet-splash. Cases highlighted by a red rectangle are non-splash at $\theta = 90^\circ$ and cases highlighted by a green rectangle are detachment-splash at $\theta = 90^\circ$.

Figure 4.24 shows the interface profile of the small jet at the early stage of the impact. A gas layer always exists between the drop and the substrate and a small jet is always ejected before contact. For a small density and viscosity ratio, the gas layer is thin and the thickness of the jet is small. A thin and flat jet with secondary droplets is observed

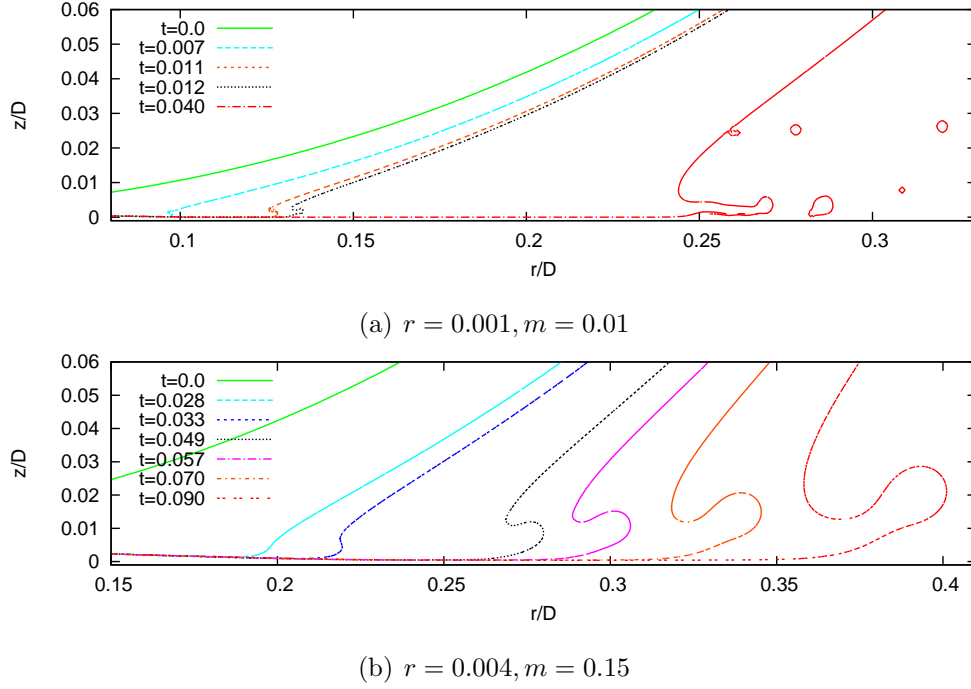


Figure 4.24: Interface profile of the small jet at the early stage of the impact for $\theta = 180^\circ$, (a) $r = 0.001, m = 0.01$ and (b) $r = 0.004, m = 0.15$.

after a time interval $\Delta t = 0.04$ from the ejection of the small jet (profile of $t = 0.040$ in Figure 4.24 (a)); for a big density and viscosity ratio, the jet is thicker and it is already lifted up after the same time interval (profile of $t = 0.070$ in Figure 4.24 (b))⁸.

With a longer time, the very thin and flat jet is finally lifted up and forms a splash. For a small density and viscosity ratio, the splash is delayed and the jet is lower. For a super-hydrophobic surface with $\theta = 180^\circ$, the gas layer exists all along the impact dynamics. The variation of gas properties influence the length and temporal scale of the jet (such as the height of the rim of the jet, the time of jet bending), but it does not change the nature of the dynamics. A jet-splash is always formed as a result of the hydrophobicity.

4.4.1.2 Impact on a totally-wettable surface ($\theta = 0^\circ$)

On a super-hydrophilic surface, the liquid drop spreads fast and will form a thin liquid film. It implies that a null contact angle restrains the detachment of the liquid film. As

⁸For a big density and viscosity ratio, the ejection of the small jet is delayed, as shown in Figure 4.24 (b), the jet starts to form at $t = 0.028$. So the interface profile at $t = 0.040$ in Figure 4.24 (a) is equivalent to the interface profile at $t = 0.070$ in Figure 4.24 (b).

shown in Figure 4.25, comparing to $\theta = 90^\circ$, the non-splash cases ($m = 0.01$) and the jet-splash cases ($m = 0.15$) do not change. As the gas is highly viscous for $m = 0.15$, a small jet has been formed long before the contact, the null contact angle does not affect the formation of the splash. For $m = 0.04$, the detachment-splash is eliminated for a small gas density ($r = 0.001$); whereas the detachment-splash still occurs for a larger gas density ($r = 0.004$).

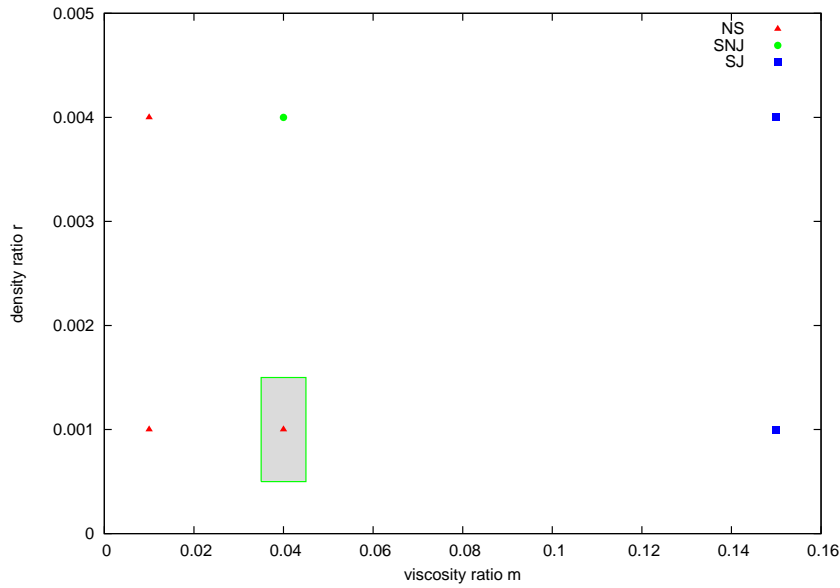


Figure 4.25: Impact outcomes for $\theta = 0^\circ$. Detachment-splash is eliminated for small density ratios as the case highlighted by a green rectangle. NS denotes non-splash, SNJ detachment-splash and SJ jet-splash.

Figure 4.26 (a) and (b) shows a comparison of the interface profile between $\theta = 0^\circ$ and $\theta = 90^\circ$. The contact angle changes the interface profile around the contact line. As shown in the insets, the null contact angle strongly restrains the detachment of the thin liquid sheet and keeps the sheet on the substrate. As discussed in the section §4.2.2, for a detachment-splash, the impulsion of the detachment of the thin liquid sheet is the aerodynamic force (scaled by $\rho_g U_g^2$). When the aerodynamic force is stronger comparing to the resistance caused by the null contact angle, the detachment of the thin liquid sheet occurs and develops to a splash (see Figure 4.26 (c) the case of $r = 0.004, m = 0.04$).

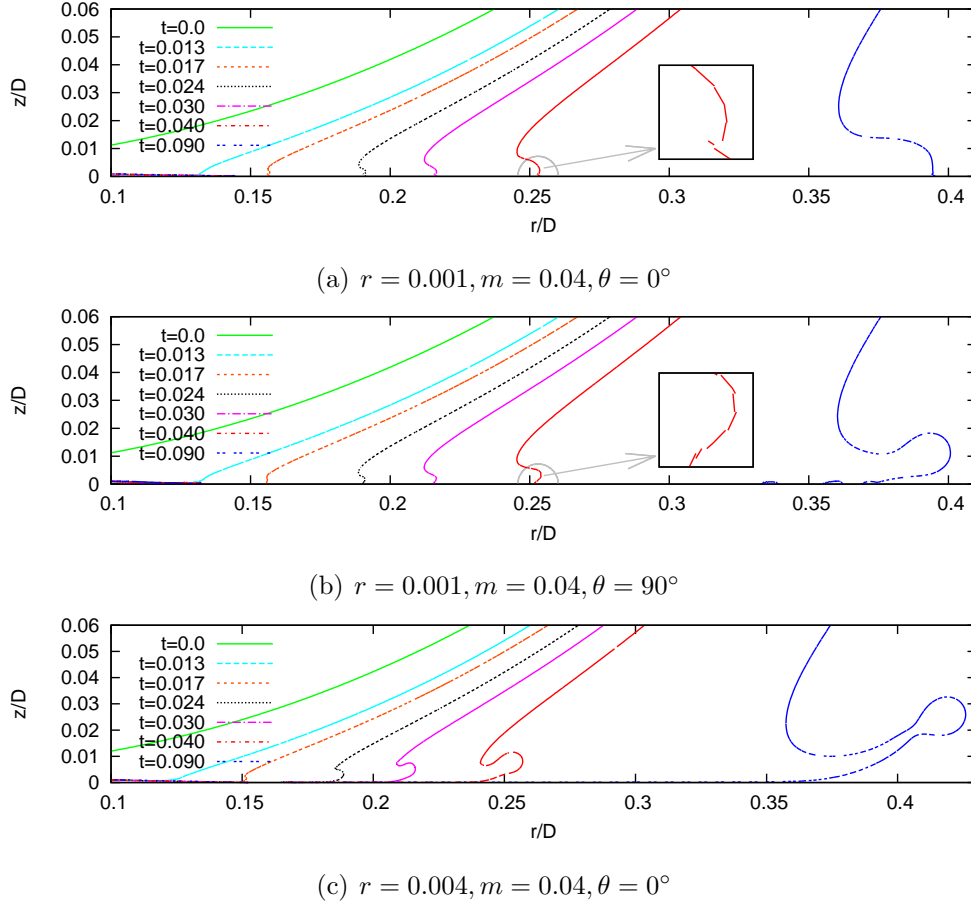


Figure 4.26: Interface profile at the early stage of the impact: (a) $r = 0.001, m = 0.04, \theta = 0^\circ$, (b) $r = 0.001, m = 0.04, \theta = 90^\circ$ (results from Chapter §3) and (c) $r = 0.004, m = 0.04, \theta = 0^\circ$. Insets show a zoom of the interface around the contact line at $t = 0.040$.

4.4.1.3 Impact on a partially-wettable surface ($\theta = 30, 60, 120, 150^\circ$)

As observed in the two extreme cases ($\theta = 0^\circ, 180^\circ$), a super-hydrophilic substrate restrains the detachment of liquid sheet and a super-hydrophobic substrate promotes the detachment. Indeed, a hydrophilic contact angle ($\theta < 90^\circ$) makes the interface close to the contact line curved towards the outside of the drop (see Figure 4.27 (a)), it is favourable to the ejection of the liquid sheet on the substrate. The rim of the liquid sheet is much thinner than the sheet and it restrains the detachment of the sheet. Whereas, a hydrophobic contact angle ($\theta > 90^\circ$) makes the interface close to the contact line curved towards the center of the drop (see Figure 4.27 (b)). The rim of the liquid sheet is already separated from the substrate which is favourable to the lift-up of the sheet.

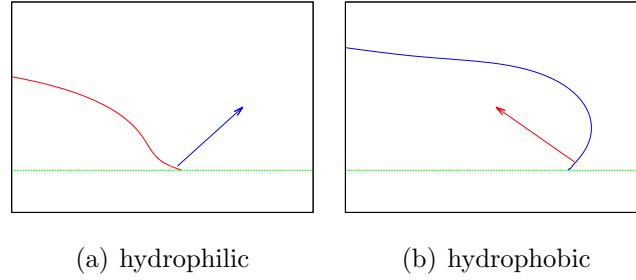


Figure 4.27: Sketch of the interface profile close to the contact line. The green dotted line represents the solid surface and the arrow indicates the curving direction of the interface.

Figure 4.28 shows the impact outcomes for different contact angles. As $m = 0.15$, the gas is highly viscous and the lubrication effect is strong. An ejected jet has been well developed before the contact with the substrate, the contact angle does not influence the splash formation and a jet-splash is always observed. The influence of the contact angle is observed for smaller viscous ratios. The detachment-splash is suppressed for hydrophilic contact angles at $m = 0.04$ and a detachment-splash is formed for a large hydrophobic contact angle ($\theta = 150^\circ$) at $m = 0.01$.

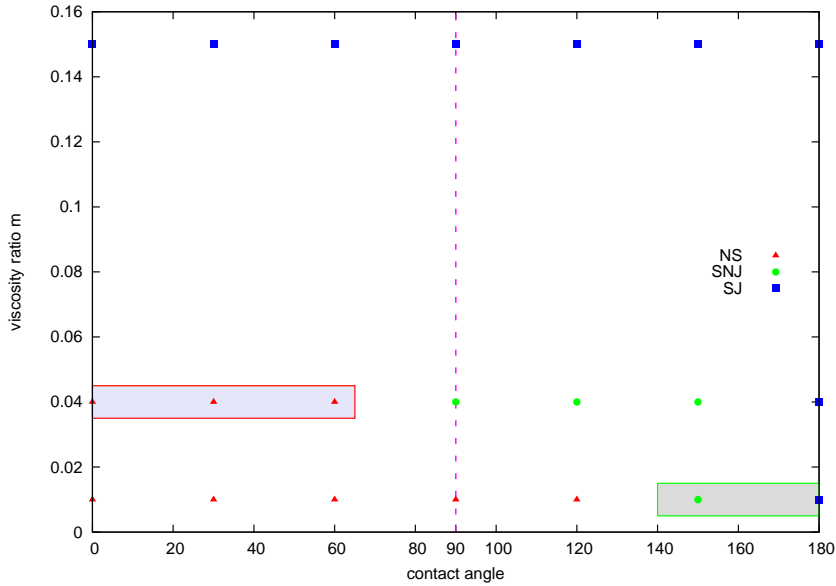


Figure 4.28: Impact outcomes for partially-wettable surfaces with different contact angles at $r = 0.001$. Results of $\theta = 0^\circ, 90^\circ, 180^\circ$ are added in the figure. NS denotes non-splash, SNJ detachment-splash and SJ jet-splash. The vertical dotted line indicates the case of $\theta = 90^\circ$, cases highlighted by a red rectangle are non-splash at $\theta = 90^\circ$ and cases highlighted by a green rectangle are detachment-splash at $\theta = 90^\circ$.

Figure 4.29 gives a clear vision of the influence of the contact angle. The contact angle takes no effect before the contact, the interface profile is identical at $t = 0$. For a larger hydrophobic contact angle ($\theta = 120^\circ, 150^\circ, 180^\circ$), the detachment of the jet occurs earlier and the rim of the jet is higher; whereas, the liquid sheet keeps on the substrate for hydrophilic contact angles ($\theta = 0^\circ, 30^\circ, 60^\circ$) and the splash is suppressed.

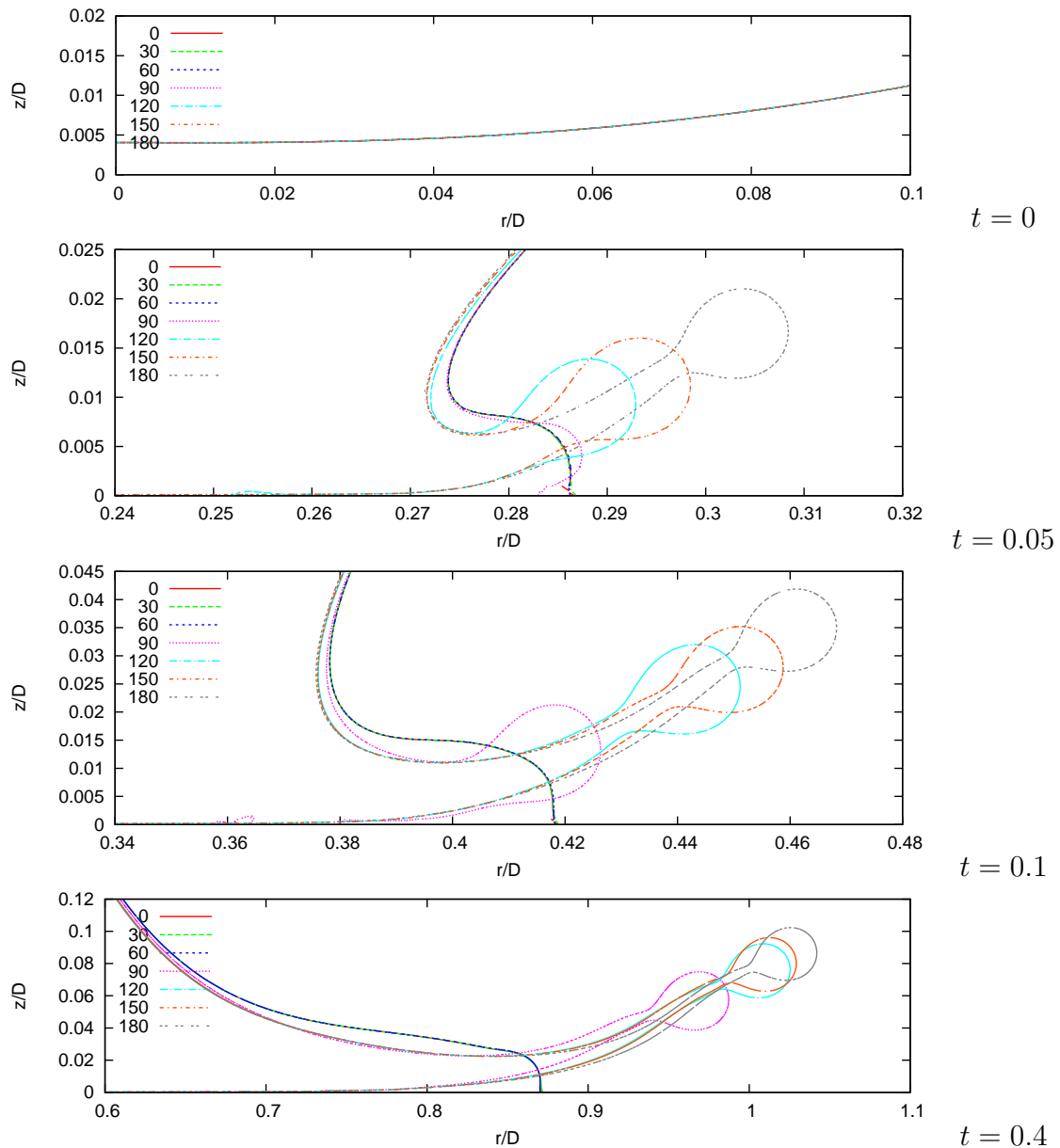


Figure 4.29: Comparison of the interface profile for different contact angles $\theta = 0^\circ, 30^\circ, 60^\circ, 120^\circ, 150^\circ, 180^\circ$ at $r = 0.001, m = 0.04$ at different moments $t = 0, 0.05, 0.1, 0.4$ from top to bottom. Results of $\theta = 90^\circ$ in Chapter §3 and results of $\theta = 180^\circ, 0^\circ$ in the sections §4.4.1.1 and §4.4.1.2 are also presented.

4.4.2 Gas compressibility effect

In fluid mechanics, the compressibility is measured by the Mach number

$$M = \frac{v}{c} \quad (4.29)$$

where v is the velocity of flow and c is the local sound speed.

For a perfect gas, the local sound speed

$$c = \sqrt{\left(\frac{\partial p}{\partial \rho}\right)_s} = \sqrt{\gamma \frac{R}{M_a} T} \quad (4.30)$$

where the subscript s means the derivative is taken adiabatically at constant entropy, γ is the adiabatic index, R is the gas molar constant, M_a is the molar mass and T is the Kelvin temperature.

To satisfy the incompressible assumption, the Mach number $M \ll 1$. In practice, $M < 0.1$ is an incompressible flow, $M < 0.3$ is a weak-compressibility flow. For $M < 0.3$, the incompressible assumption is confirmed.

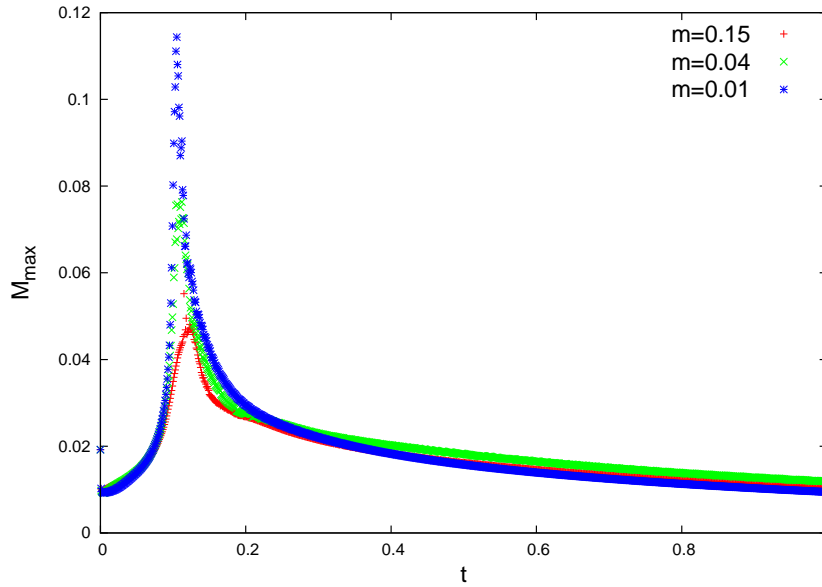


Figure 4.30: Temporal evolution of the maximum value of the Mach number in the gas phase at the density ratio $r = 0.001$ and the viscosity ratio $m = 0.01, 0.04, 0.15$.

In our simulations, we do not consider the influence of the temperature, so the density is regarded constant and the flow is isothermal. At the Standard Atmospheric Pressure (SAP $1.01325 \times 10^5 Pa$) and the ambient temperature ($20^\circ C$), the speed of sound is about

$340 \text{ m} \cdot \text{s}^{-1}$. Figure 4.30 shows the evolution of the maximum Mach number in the entire gas phase⁹. We do observe a significant increase of the Mach number as the impact occurs, but the maximum Mach number $M \sim 0.1$. Therefore, the incompressible assumption is satisfied in the entire calculation domain even in the gas layer during the impact dynamics.

4.5 Conclusion

In this chapter, we investigated systematically the drop impact dynamics. According to our investigations, gas compressibility effect is not important in our simulations. The surrounding gas takes effect on splashing in the incompressible regime. If we regard both the small jet and the thin liquid sheet as an ejecta, the splash originates from the creation and deflection of the ejecta at the very early stage of the impact.

For a large gas density and viscosity, a jet-splash is formed. The scaling law predicted by the lubrication theory is valid before the creation of the small jet in the gas layer: the thickness of the gas layer $h_e \sim St^{\frac{2}{3}}$, the radius of the central entrapped bubble $r_e \sim St^{\frac{1}{3}}$ and the maximum pressure in the gas layer $p_g \sim h_{min}^{-\frac{1}{2}}$. Subsequent to the ejection of the jet, it is immediately lifted up by the aerodynamic force scaled by $\rho_g v_g^2$. By decreasing the gas density or viscosity, the drop contacts the substrate without jet ejection. A thin liquid sheet is immediately ejected and moves fast on the substrate. It can be detached by a sufficient aerodynamic force scaled by $\rho_g v_g^2$, otherwise no splash is formed.

A central entrapped bubble is always observed in simulations and its profile can be considered invariant during the drop impact, then it is not a crucial factor for splashing. A series of small bubbles are also observed as a result of the creation of local contacts in front of the contact line. The contact angle influences the impact dynamics, a hydrophilic contact angle can eliminate a splash, while a hydrophobic contact angle can promote a splash.

⁹To calculate the corresponding dimensional gas velocity, we take a water drop with an initial velocity of $3 \text{ m} \cdot \text{s}^{-1}$.

Chapter 5

Drop impact on a highly-viscous liquid

Contents

5.1	Physical description	114
5.2	Numerical investigations	117
5.2.1	Wave-like period	118
5.2.2	Solidification period	121
5.2.3	Comparison with an impact on solid	124
5.3	Comparison with the experiments	127
5.4	Conclusion	131

Drop impact on a wetted surface, on a thin liquid layer or on a deep liquid pool is also often reported in the literature [Howison *et al.*, 2005, Josserand and Zaleski, 2003, Lampe *et al.*, 2005, Weiss and Yarin, 1999]. A major difference between an impact on solid and on liquid is the contact line. In experiments, the drop and the basin are usually of the same liquid or of two miscible liquids, therefore, the contact line between different liquid phases is generally not considered.

Regarding the outcomes of the impact, some similarities exist between a liquid/liquid impact and a liquid/solid impact. The study in Chapter §3.2 shows that the radius of the wetted area of a liquid/solid impact obeys the same law (equation 3.2) obtained from an analysis of the liquid/liquid impact [Josserand and Zaleski, 2003]. Indeed, solid can be considered as a liquid with an infinity viscosity and infinity density. Some common liquids

are highly viscous. For example, honey can be 10000 times more viscous than water. A similar performance for such highly viscous liquid comparing to a solid probably exists.

In the literature, experiments of the impact on liquid are generally reported on a low-viscosity liquid basin (such as water, alcohol) and the impact between a normal liquid drop and a highly-viscous liquid basin is not studied. Experiments of a normal liquid drop impacting on a highly-viscous liquid basin are executed in our group. Some inspiring results are found and a similarity to the impact on solid is observed. The highly-viscous basin (honey) performs as a solid during the drop impact dynamics. As the two liquids are miscible, the contact line is no longer considered. The experiments executed in our laboratory strongly motivate us to study this dynamics and find the connection between the impact on solid and the impact on liquid in order to further understand the splash mechanism.

In this chapter, a theoretical model is proposed to deal with the triple-phase impacting dynamics, of which a drop of normal liquid impacts on a highly viscous liquid basin. Numerical investigations are executed and comparisons between our simulations and the experimental results are also discussed.

5.1 Physical description

Some physical properties of water, ethanol and honey ¹ under the Standard Atmospheric Pressure (SAP $1.01325 \times 10^5 Pa$) and the ambient temperature ($20^\circ C$) are listed in Table 5.1:

Table 5.1: Physical properties of water, ethanol and honey

	density ρ ($kg \cdot m^{-3}$)	viscosity μ ($Pa \cdot s$)	surface tension γ ($N \cdot m^{-1}$)
water	998.2	1.002×10^{-3}	0.0728
ethanol	789	2.7×10^{-3}	0.0224
honey	1500	$10 \sim 100$	$0.055 \sim 0.068$

¹The physical properties of honey vary largely between different types of honey [Oroian, 2013, Rehman *et al.*, 2008]. Especially the viscosity and the surface tension have a strong dependency on the temperature and on the concentration. Here, we give a range of values reported in the literature.

As shown in Table 5.1, the density and the surface tension of honey take the same order of magnitude of water and ethanol, but the viscosity of honey is at least 10^4 times larger. Viscous effect is probably dominant as compared to the inertial and surface tension effects in the dynamics of impact on a honey basin.

The dynamics involves three phases: gas and two different liquids. We suppose the two liquids are Newtonian fluids. As viscous effect is dominant, the variation of density and of surface tension caused by the two different liquids can be neglected in a mixed area, we take an equal density for two liquids and an identical surface tension at the interface.

We introduce the first volumetric fraction $c_1(\mathbf{x}, t)$ to distinguish the gas and liquid phase, the viscosity of the system can be defined as:

$$\mu(c_1) = c_1\tilde{\mu}_l + (1 - c_1)\mu_g \quad (5.1)$$

where $\tilde{\mu}_l$ is the effective viscosity of liquid.

Then we introduce the second volumetric fraction $c_2(\mathbf{x}, t)$ to distinguish two liquid phases, the effective viscosity of liquid $\tilde{\mu}_l$ can be defined as:

$$\tilde{\mu}_l(c_2) = c_2\mu_{l2} + (1 - c_2)\mu_{l1} \quad (5.2)$$

where the subscripts $l1, l2$ denotes the two liquids.

Substituting equation (5.2) into equation (5.1), gives the viscosity of the system $\mu(c_1, c_2)$:

$$\mu(c_1, c_2) = c_1c_2\mu_{l2} + c_1(1 - c_2)\mu_{l1} + (1 - c_1)\mu_g \quad (5.3)$$

The density of the system is defined as:

$$\rho(c_1) = c_1\rho_l + (1 - c_1)\rho_g \quad (5.4)$$

Figure 5.1(a) shows the calculation domain. The calculation is axisymmetric, a symmetric boundary condition is applied on the left boundary. A semi-circular drop of normal liquid of diameter D falls with an initial velocity U_0 without gravity and a basin of highly-viscous liquid is at the bottom of the domain. The density of the two liquids is equal and the surface tension is uniform. The initial distance between the drop and the basin is $0.1D$ and the depth of the basin is $0.5D$.

To measure the viscosity deviation from a normal liquid, we introduce a liquid-viscosity ratio between two liquids m_l :

$$m_l = \frac{\mu_{l2}}{\mu_{l1}} \quad (5.5)$$

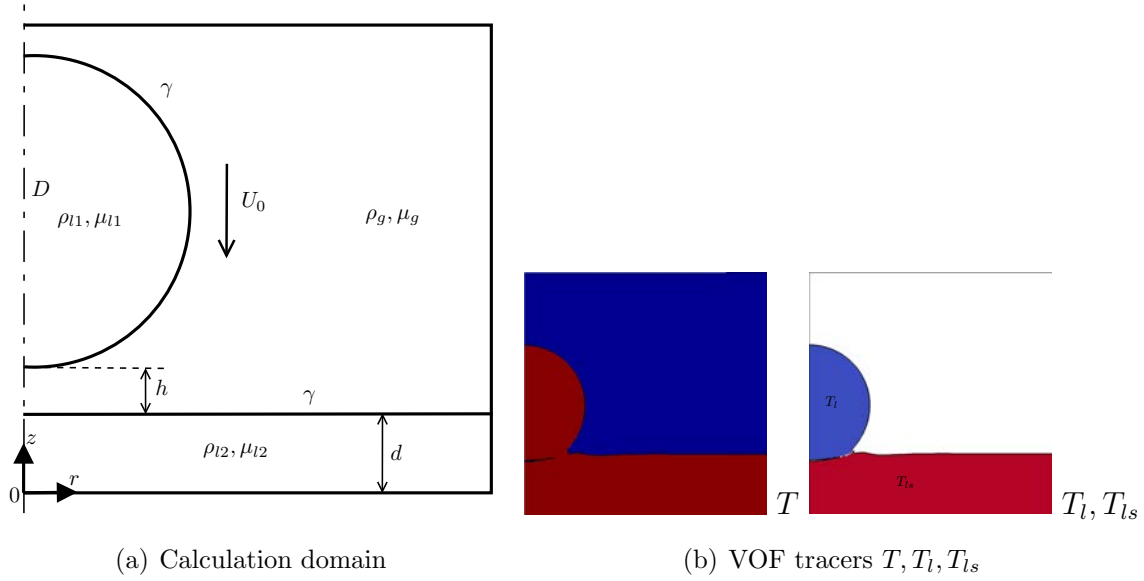


Figure 5.1: (a) Calculation domain. The domain is square. A semi circular drop of normal liquid 1 of diameter D , density ρ_{l1} and viscosity μ_{l1} falls with an initial velocity U_0 without gravity. A basin of highly-viscous liquid 2 of depth $d = 0.5D$, density ρ_{l2} and viscosity μ_{l2} is located at the bottom of the domain. The initial distance between the drop and the basin is $h = 0.1D$. Surrounding gas has a density ρ_g and a viscosity μ_g . A surface tension γ is applied in the domain and the density of the two liquids are equal ($\rho_{l1} = \rho_{l2}$). (b) Volume-of-Fluid (VOF) tracers. T is introduced to distinguish the liquid and the gas, T_l is to track the drop and T_{ls} is to track the liquid basin.

where μ_{l1} is the viscosity of the normal liquid. The density ratio $r = \rho_g/\rho_{l1}$ and the viscosity ratio $m = \mu_g/\mu_{l1}$ are used to control the properties of the normal liquid. The density ratio is fixed at $r = 0.001$ and the viscosity ratio is fixed at $m = 0.1$, it is a jet-splash case for the impact on solid ($\theta = 90^\circ$). Numerically, we introduce three VOF tracers (see Figure 5.1(b)). T is introduced to distinguish liquid and gas in global, T_l is set to track the drop and T_{ls} is set to track the liquid basin. Values of nondimensionlized physical parameters used in simulations are shown in Table 5.2.

Table 5.2: Values of nondimensionlized physical parameters in simulations

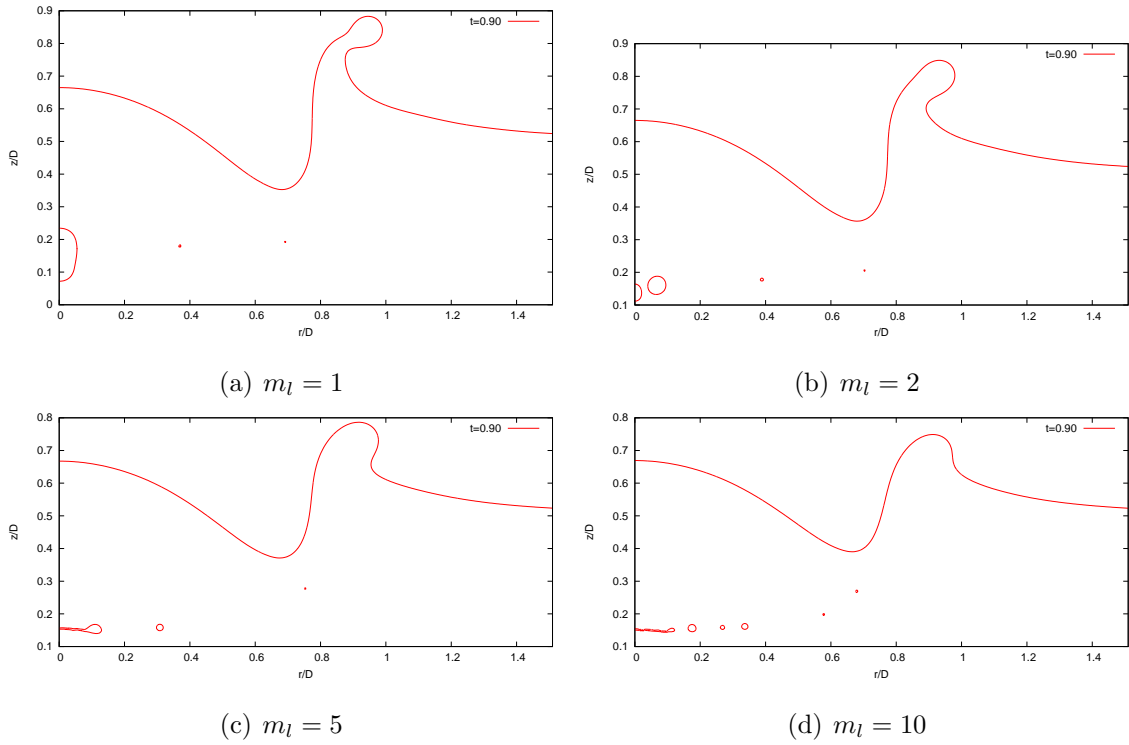
ρ_{l1}^*	ρ_{l2}^*	ρ_g^*	μ_{l1}^*	μ_{l2}^*	μ_g^*	γ^*	U_0^*	D^*	d^*	h^*
1	1	0.001	0.001	$0.001m_l$	1×10^{-4}	2.70×10^{-3}	1	1	0.5	0.1

5.2 Numerical investigations

Drop falls from a height $h = 0.1D$ to the liquid basin, with absence of gas, it contacts the basin at $t_{th} = h/U_0 = 0.1$. We rescale the time by $\tilde{t} = t - t_{th}$.

Figure 5.2 shows the interface profile at $\tilde{t} = 0.9$. At $m_l = 1$, it is an impact of a normal liquid as observed by Josserand and Zaleski [2003], a jet is formed and a central entrapped bubble is observed. With increase of the viscosity of the liquid basin, the jet becomes smaller, then it turns to a wave-like shape (see Figure 5.2(e), $m_l = 20$) and the central entrapped bubble becomes flat and collapses into small bubbles.

Subsequent to the wave-like cases, the jet is formed again and a series of bubbles form an “interface” between the drop and the basin (see Figure 5.2(g), $m_l = 100$). With further increase of the viscosity of the liquid basin, a gas layer is observed between the drop and the basin (see Figure 5.2(h), $m_l = 500$). The two liquids become “immiscible”. The maximum deviation of basin interface compared to the initial position decreases. At $m_l = 10000$, the liquid basin remains flat as a solid substrate (see Figure 5.2(l)).



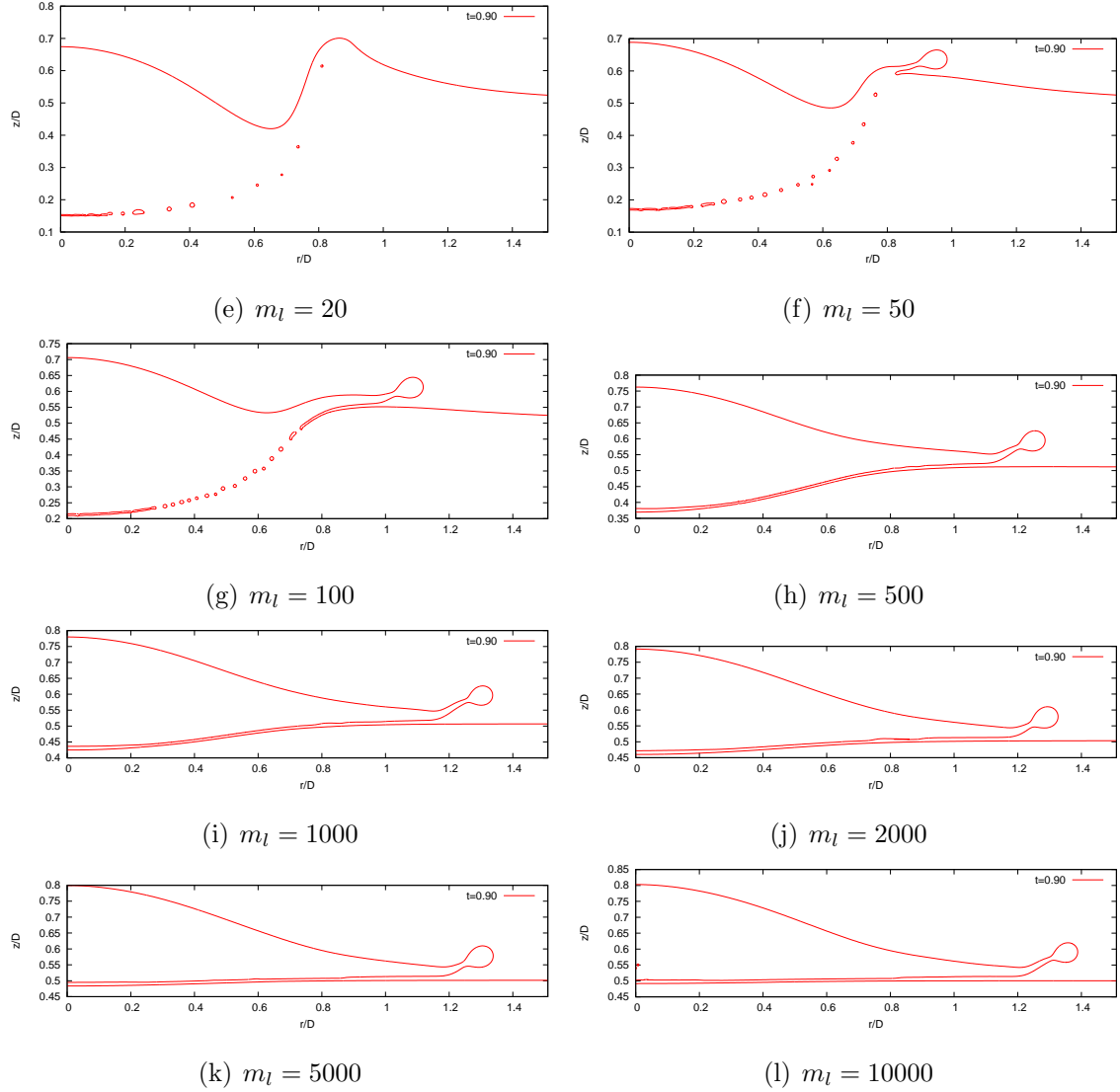


Figure 5.2: Interface profile for different liquid-viscosity ratios m_l at $\tilde{t} = 0.9$.

5.2.1 Wave-like period

To describe the impact dynamics in the wave-like period, we define four quantities (see Figure 5.3):

- h_{r0} : the central height of the top interface of the drop, it becomes the height of the entire liquid at the symmetry axis ($r = 0$) when the drop contacts the basin after impact.
- h_i : the central height of the bottom interface of the drop h_{id} and the central height of the highly-viscous liquid basin h_{ib} , we denote them as h_i . The difference between

h_{id} and h_{ib} represents the thickness of the gas layer between the drop and the basin before contact, then the thickness of the central entrapped bubble after contact.

- h_w : the height of the wave crest.
- r_w : the distance between the wave crest and the symmetry axis ($r = 0$), we define it as the radius of the wave crest r_w .

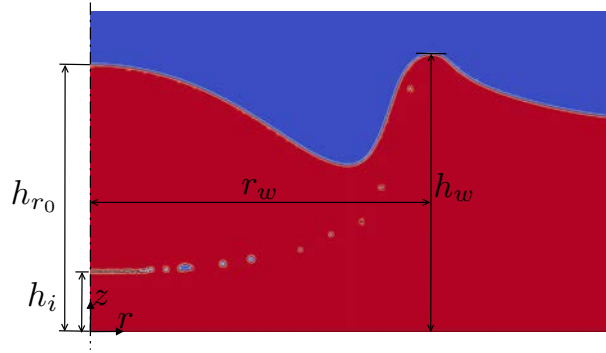


Figure 5.3: Sketch of the wave-like interface.

The wave crest propagates towards the outside, its height h_w and radius r_w both decrease with a larger viscosity of the basin as compared to an impact between a same normal liquid (see Figure 5.4). The kinematic energy transferred from the impacting drop is dissipated faster and the size of the wave crest declines in a more viscous basin.

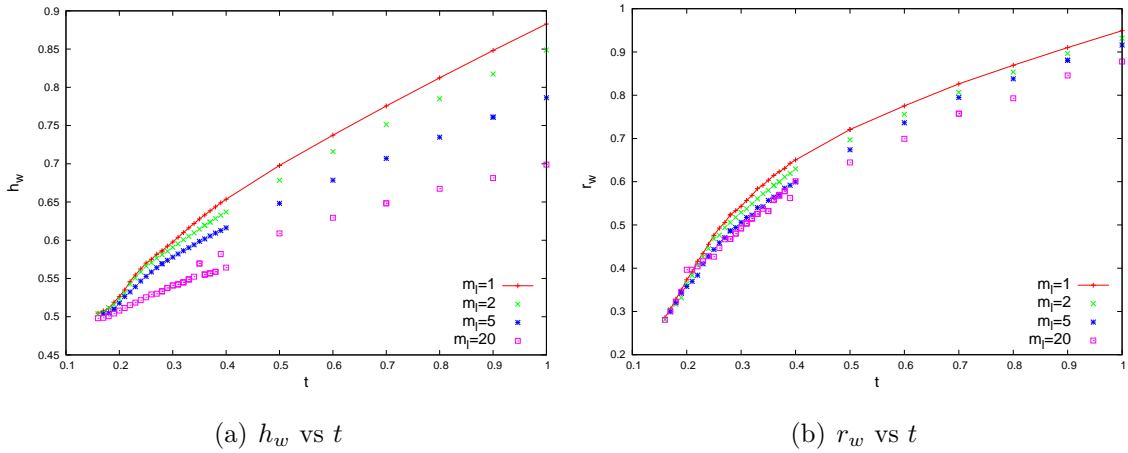


Figure 5.4: Temporal evolution of characteristic lengths of the wave crest. (a) The height of the wave crest h_w vs t ; (b) the radius of the wave crest r_w vs t . Case $m_l = 1$ is plotted as a reference.

The increase of the viscosity of the basin influences slightly the top interface (see Figure 5.5(a)), but the thickness of the central entrapped bubble decreases largely (see Figure 5.5(b)). As shown in Figure 5.6, the bubbles form an “interface” between the two liquids. As a “frontier” between the two liquids, the “bubble-interface” is first influenced by the increase of the viscosity of the basin. At $\tilde{t} = 0.9$, for an impact between the same normal liquid, the central bubble has already formed a shape of an olive, its vertical length is larger than its horizontal length (see Figure 5.6(a)). With the increase of m_l , the central bubble is broken into small bubbles and the central bubble remains flat.

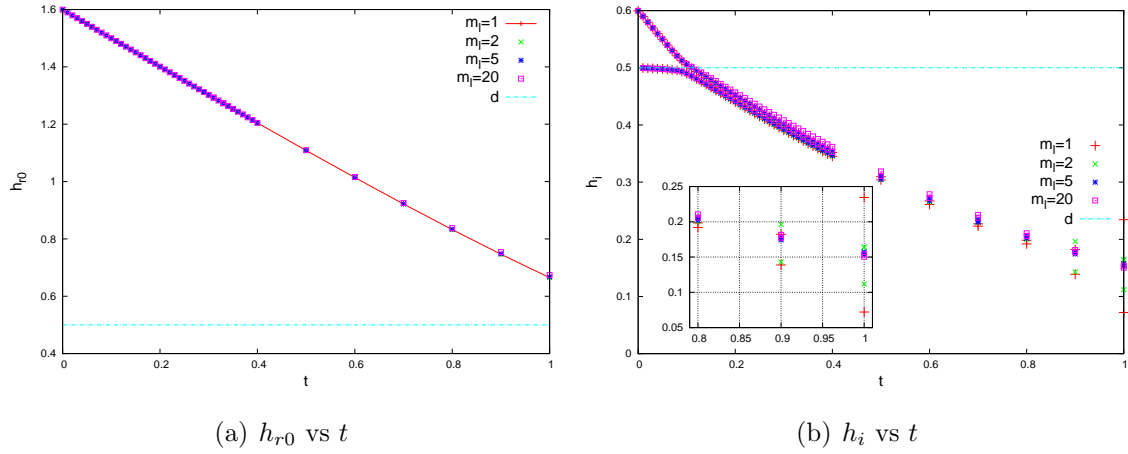
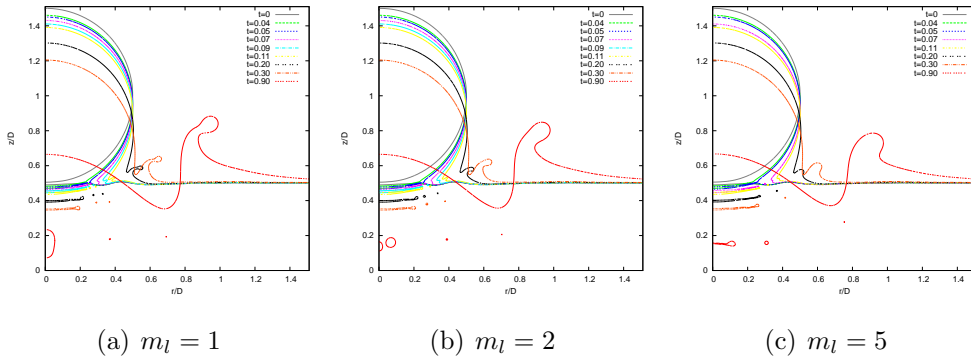


Figure 5.5: Temporal evolution of heights at the symmetry axis ($r = 0$). (a) The central height of the top interface of the drop h_{r0} vs t ; (b) the height of lower interfaces h_i vs t , inset shows a zoom at $t = [0.8, 1]$, the difference between the top and bottom points at a certain moment t is equal to the thickness of the central entrapped bubble. d denotes the initial position of the liquid basin. Case $m_l = 1$ is plotted as a reference.



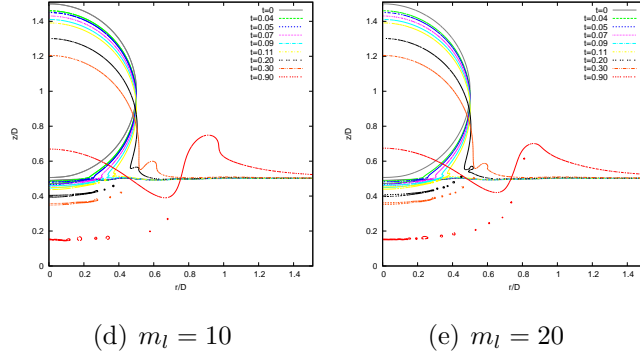


Figure 5.6: Temporal evolution of the interface profile for different liquid-viscosity ratios m_l in the wave-like period.

5.2.2 Solidification period

With further increase of the viscosity of the basin, the jet is formed again and the liquid basin becomes more and more resistant to the deformation. The liquid basin seems to be solidified, we name it a solidification period.

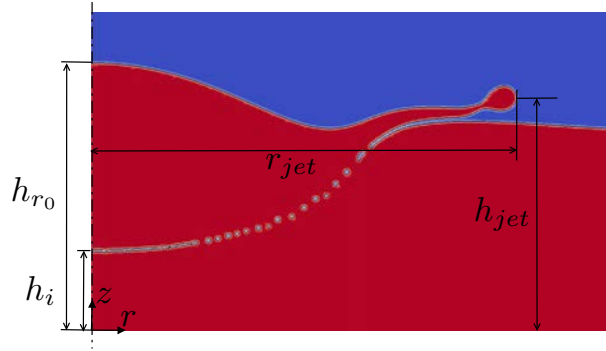


Figure 5.7: Sketch of the interface in the solidification period.

To describe the impact dynamics in the solidification period, we define four quantities (see Figure 5.7):

- h_{r0} : the central height of the top interface of the drop, it becomes the height of the entire liquid at the symmetry axis ($r = 0$) when the drop contacts the basin after impact.
- h_i : the central height of the bottom interface of the drop h_{id} and the central height of the highly-viscous liquid basin h_{ib} , we denote them as h_i . The difference between h_{id} and h_{ib} represents the thickness of the gas layer between the drop and the basin

before contact, then the thickness of the central entrapped bubble (or the gas layer) after contact.

- r_{jet} : the radius of the rim of the jet.
- h_{jet} : the height of the rim of the jet (the z-coordinate of the r_{jet} -point).

As shown in Figure 5.8, for a certain m_l , both h_{jet} and r_{jet} increase in time. With increase of the viscosity of the liquid basin, the height of the rim of the jet h_{jet} first decreases (from $m_l = 1$ to $m_l = 500$) then keeps nearly constant (from $m_l = 500$ to $m_l = 10000$), it is much smaller than h_{jet} of an impact between the same normal liquid ($m_l = 1$). The radius of the rim of jet r_{jet} increases with the viscosity of the liquid basin. It implies that the basin acts more and more as a solid and the jet expands much further toward the outside.

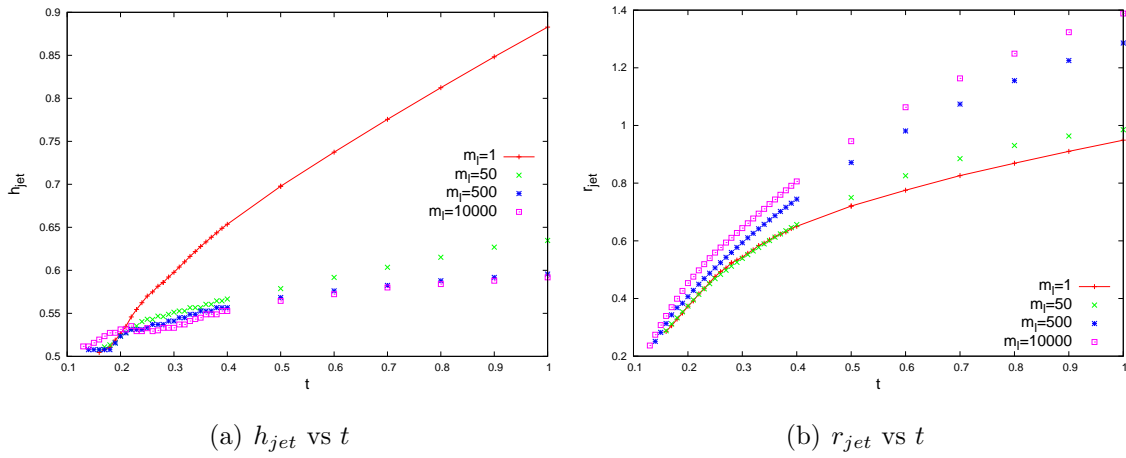


Figure 5.8: Temporal evolution of characteristic lengths of the jet. (a) The height of the rim of the jet h_{jet} vs t ; (b) the radius of the rim of the jet r_{jet} vs t . Case $m_l = 1$ is plotted as a reference.

When the basin becomes more viscous, the top interface is also influenced, h_{r0} increases (see Figure 5.9(a)). The deviation of the interface of the basin from the initial position declines. As the ratio m_l comes to the order of magnitude of honey, the interface of the basin remains at the initial position during the impact (see the case of $m_l = 10000$ in Figure 5.9(b)).

Figure 5.10 shows the temporal evolution of the interface. The central bubble keeps thin and flat. It becomes difficult for the drop to penetrate into the basin with increase

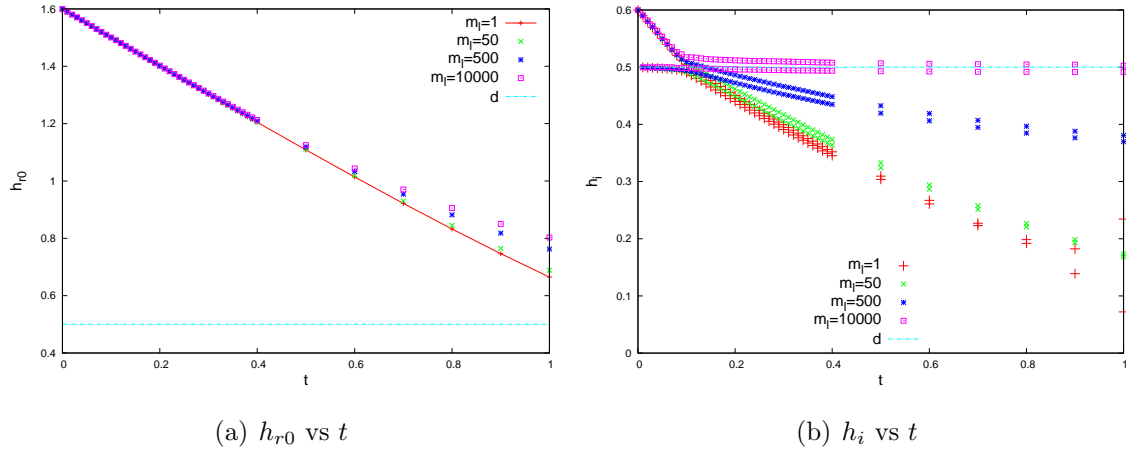


Figure 5.9: Temporal evolution of heights at the symmetry axis ($r = 0$). (a) The central height of the top interface of the drop h_{r0} vs t ; (b) the height of lower interfaces h_i vs t . d denotes the initial position of the liquid basin. Case $m_l = 1$ is plotted as a reference.

of m_l . When the viscosity of the basin becomes large ($m_l = 500, 1000, 5000, 10000$), a continuous gas layer is formed between the drop and the liquid basin. At $m_l = 5000$, the liquid basin performs already as a solid substrate (see Figure 5.10(e)).

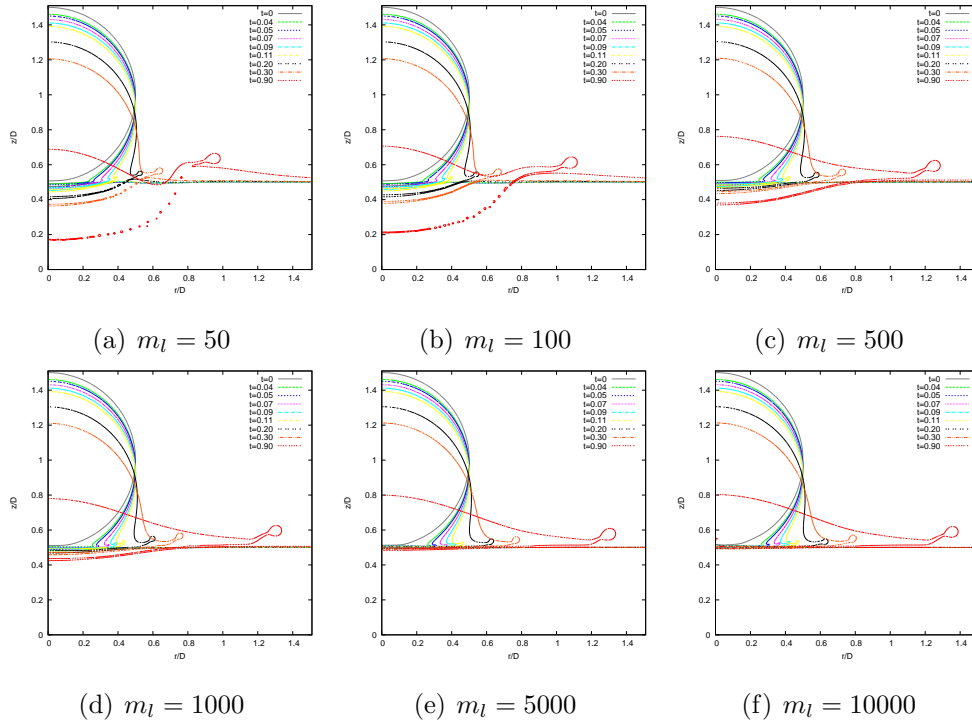


Figure 5.10: Interface evolution for different m_l in the solidification period.

5.2.3 Comparison with an impact on solid

Figure 5.11 shows an interface comparison for $m_l = 1, 20, 500, 10000$. At $\tilde{t} = 0$, for $m_l = 1$, the bottom interface of the drop keeps a parabola profile and a capillary wave is formed on the basin; whereas, for $m_l = 10000$, the basin keeps a flat surface and a capillary wave is observed at the bottom part of the drop. At $\tilde{t} = 0.07$, for $m_l = 10000$, a jet is already formed and lifted-up, a gas layer exists between the drop and the basin and a capillary wave can be still observed on the bottom interface of the drop. The thickness of the gas layer takes the same scale as the thickness of the jet.

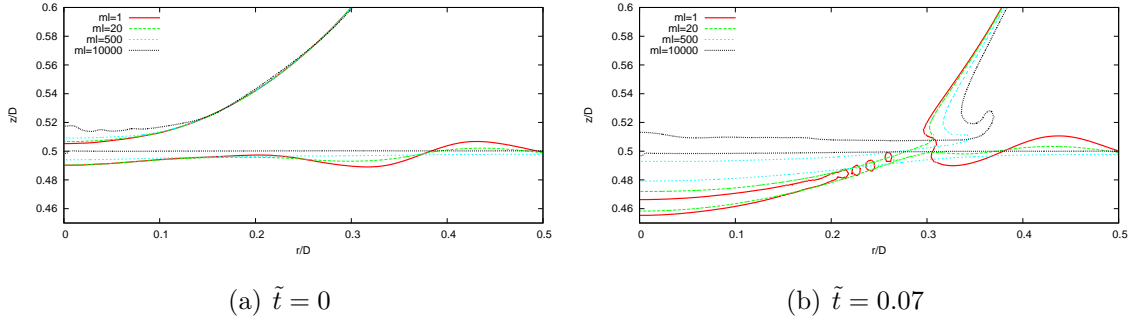
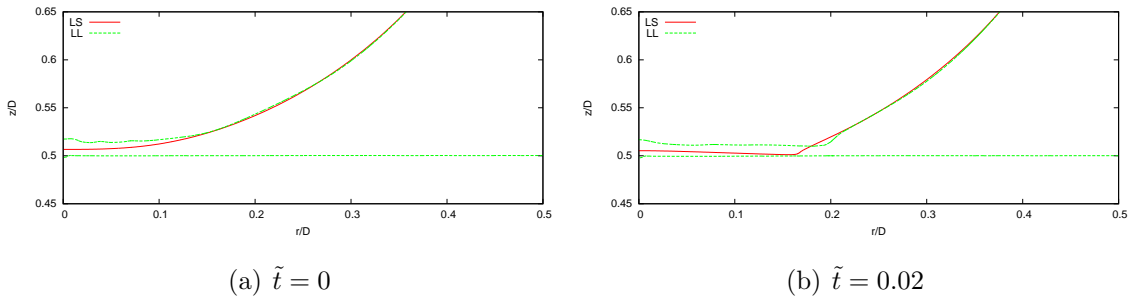


Figure 5.11: Interface comparison for $m_l = 1, 20, 500, 10000$ at (a) $\tilde{t} = 0$ and (b) $\tilde{t} = 0.07$.

Figure 5.12 shows the comparison between the impact on solid and the impact on highly-viscous liquid ($m_l = 10000$) with an equal density ratio $r = 0.001$ and an equal gas/liquid viscosity ratio $m = 0.1$. The impact on a highly-viscous liquid is a jet-splash.



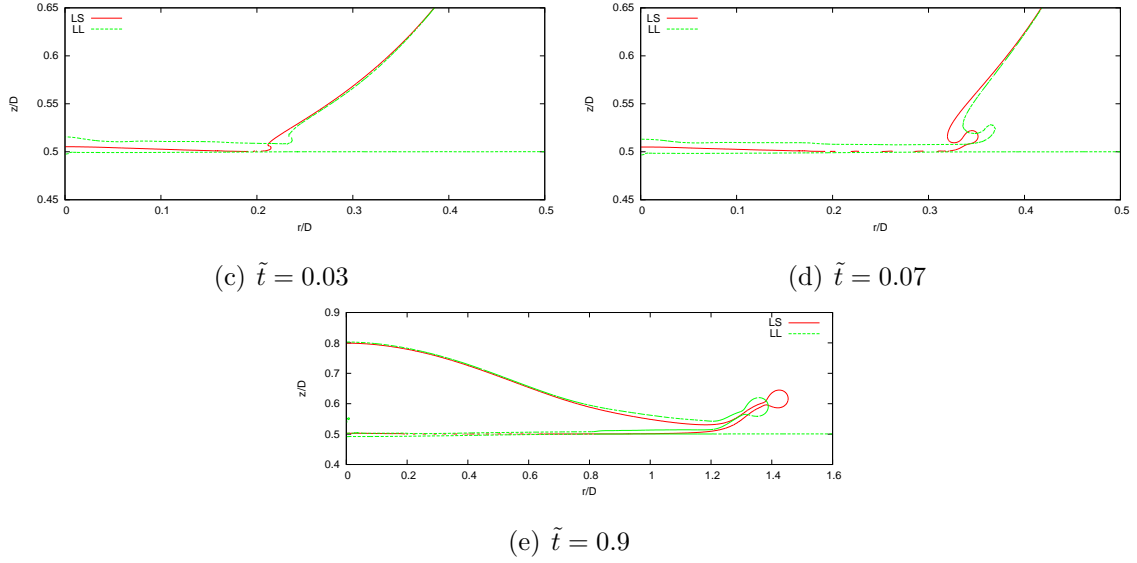


Figure 5.12: Interface comparison between the impact on a solid and the impact on a highly-viscous liquid ($m_l = 10000$) at $r = 0.001, m = 0.1$. The solid substrate is located at $z = 0.5$ for the impact on solid. LS denotes liquid/solid impact and LL denotes liquid/highly-viscous-liquid impact.

Since the thickness of the gas layer is largely enhanced, we can obtain a clear view of the jet-splash mechanism proposed in Chapter §4.

As shown in Figure 5.13, when the drop approaches the “solid”, the gas cushioning effect decelerates the drop and an amount of gas is trapped under the drop (see Figure 5.13(a)). A strong gradient of the velocity (vorticity) is found along the bottom interface of the drop, especially around the corner-like zone. Meanwhile, a capillary wave is created on the bottom interface of the drop². The wave propagates toward the outside (see Figure 5.13(b)). The corner-like part of the drop has a large velocity and the interface at the corner is not stable. A fast-moving thin liquid jet is then ejected and it is flat at the very beginning (see Figure 5.13(c)). Around the small liquid jet, the high velocity of the surrounding gas makes the inertial effect no longer negligible. The small jet is immediately³ lifted up by the aerodynamic force (scaled by $\rho_g v_g^2$) after its ejection (see Figure 5.13(d,e)).

²A capillary wave is also observed in the liquid/solid impact.

³The lift-up occurs in a time interval smaller than $\Delta t^* = 0.01$ (see Figures 5.13(c,d)), for a drop of diameter $D = 3 \text{ mm}$ with an initial velocity of $U_0 = 3 \text{ m} \cdot \text{s}^{-1}$, the corresponding dimensional time interval is $\Delta t = 10^{-6} \text{ s}$. The lift-up dynamics occurs really fast.

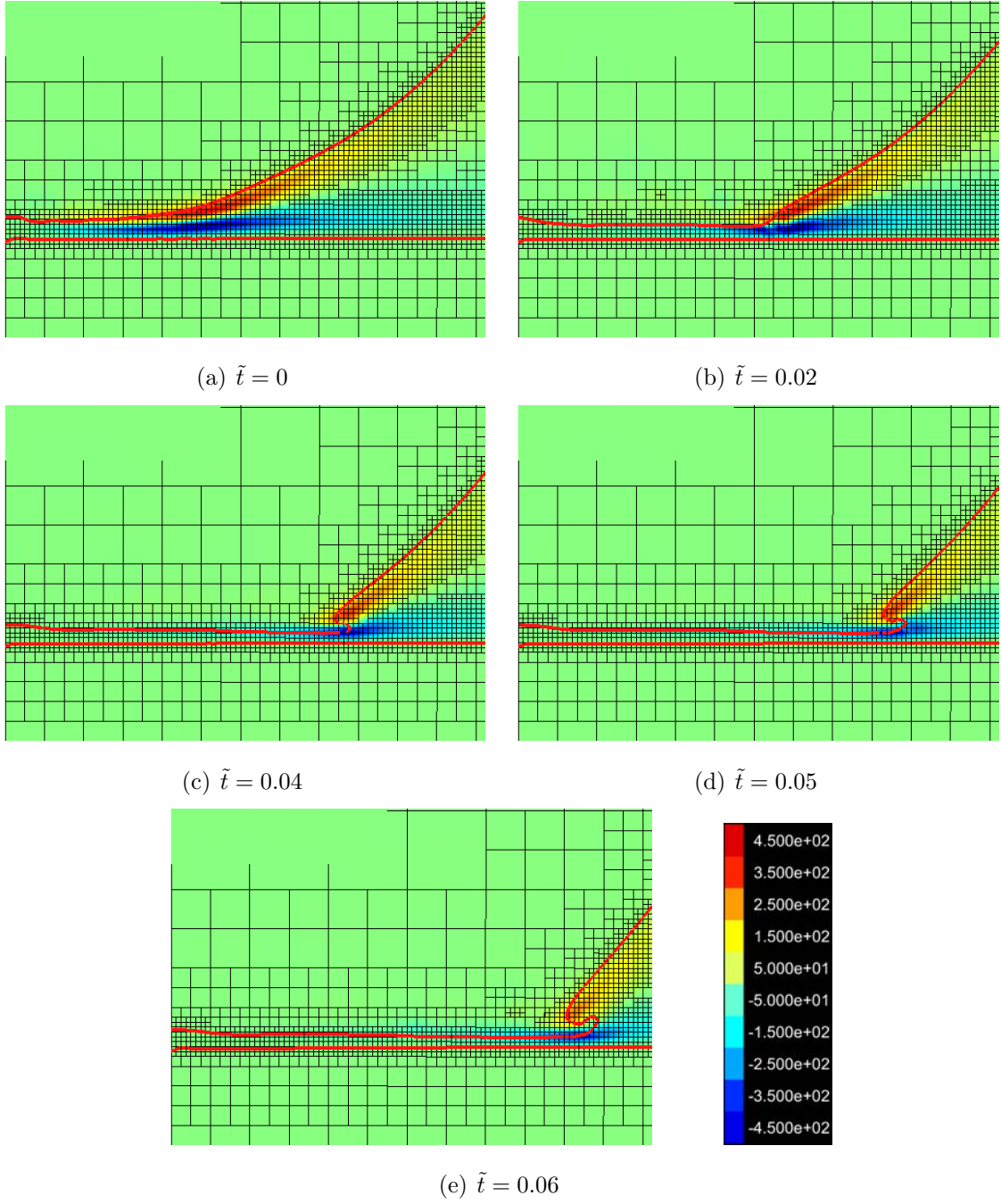


Figure 5.13: Snapshots of an impact on a highly-viscous liquid ($m_l = 10000$) at $r = 0.001$, $m = 0.1$. The color gradient represents the vorticity field, as indicated by the value legend, the green color in the major part of the snapshot represents a null-vorticity. The red curves denote the interface and the adaptive quad-tree meshes are also presented in black lines.

5.3 Comparison with the experiments

Our team has executed experiments of the drop impact on a highly viscous liquid (for instance, honey) which have not been reported in the literature so far as to our knowledge.

The drops were made of ethanol with a density $789 \text{ kg} \cdot \text{m}^{-3}$ and a viscosity $2.7 \times 10^{-3} \text{ Pa} \cdot \text{s}$. The liquid basin was made of a commercial honey - Honey of Acacia (“Miel d’Acacia” in French). Honey of Acacia is a monofloral honey with industrial treatments such as the rapid decrystallization. The viscosity of honey is $20 \text{ Pa} \cdot \text{s}$ at the ambient temperature 20°C and its density is $1398 \sim 1445 \text{ kg} \cdot \text{m}^{-3}$ [Meli, 2014].

Drops were generated by a syringe system, syringes of different diameters were used to create drops of different sizes and a stepping-motor system was employed to insure the reproducible diameter of drops with the same syringe. The drops were released from rest in a vacuum chamber, we controlled the impacting velocity by changing the initial falling height of the drop. The gas pressure in the vacuum chamber could be varied from the Standard Atmospheric Pressure (SAP $1.01325 \times 10^5 \text{ Pa}$) to low pressures (for instance, $2.1325 \times 10^4 \text{ Pa}$ - one fifth of the SAP) by a pump system. An ultra-high-speed camera (Photron FASTCAM SA5 model 1000K-M1 [Photron, 2012]) was used to record the drop impact dynamics. The record rate is 10000 fps which gives a temporal distinction of 0.1 ms ⁴.

Figure 5.14 shows experimental results under different background air pressures. The drop diameter is $d_0 = 3.6 \pm 0.1 \text{ mm}$, the impact velocity is $4 \pm 0.04 \text{ m} \cdot \text{s}^{-1}$ and the time interval between frames is 0.2 ms . In Case A, it is under the Standard Atmospheric Pressure (SAP $1.01325 \times 10^5 \text{ Pa}$). The first frame shows the drop profile just as it is about to impact on the honey basin. The drop has already a shape deformation before the impact, it is due to the surrounding gas during falling, but the deformation is slight as compared to a sphere. There is no apparent deformation of the honey basin. The honey performs as a solid substrate. The impact outcome is similar to the impact on a solid substrate reported by Xu *et al.* [2005]: drop splashes.

⁴Since the objective of experiments was to catch the dynamics of the drop impact, an ultra-high-speed camera of 10000 fps was chosen. As a compromise, the image resolution is not quite high in each frame.

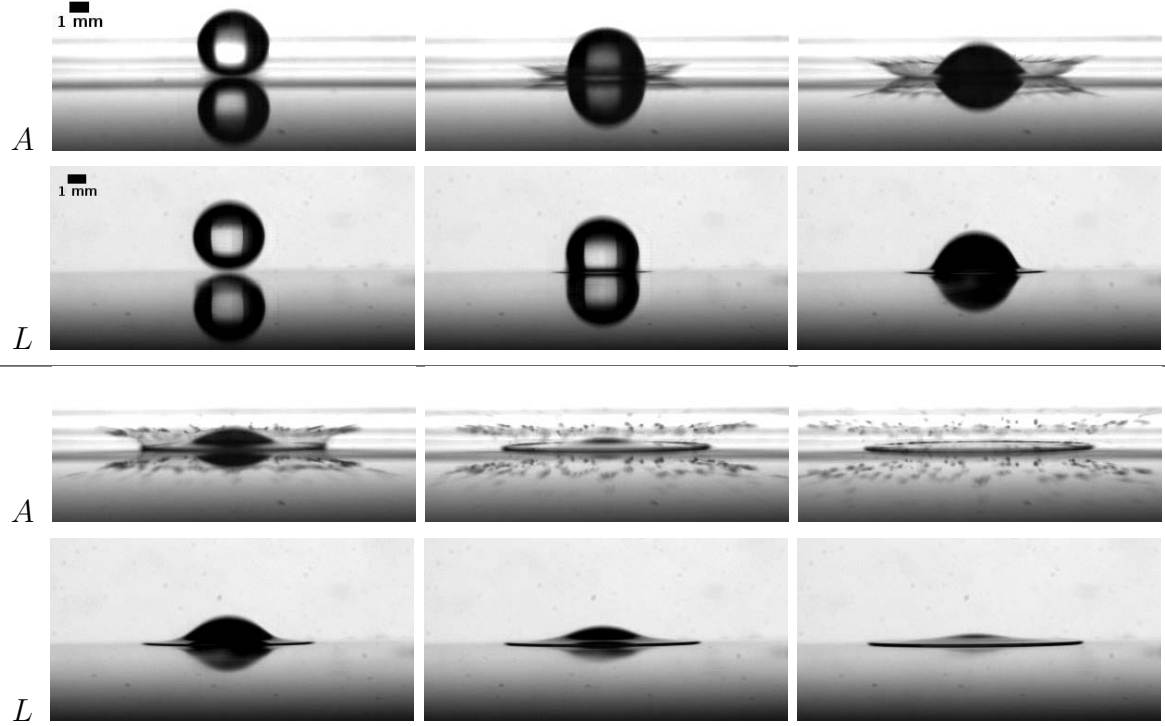


Figure 5.14: Photographs of an ethanol drop impacting on a honey basin (taken by Michon [2012]) under different background pressures of air. The drop diameter is $d_0 = 3.6 \pm 0.1 \text{ mm}$ and the impact velocity is $4 \pm 0.04 \text{ m} \cdot \text{s}^{-1}$. The first frame shows the drop just as it is about to impact on the honey basin and the black bar is the length scale of 1 mm . The time interval between frames is 0.2 ms . In Case *A*, under the Standard Atmospheric Pressure (SAP $1.01325 \times 10^5 \text{ Pa}$), drop splashes. In Case *L*, under an air pressure of $2.1325 \times 10^4 \text{ Pa}$ (one fifth of the SAP), splash is completely suppressed and the drop spreads flat on the basin.

The complete suppression of splash due to the decrease of the gas pressure reported by Xu *et al.* [2005] was also observed. In Case *L*, the air pressure is $2.1325 \times 10^4 \text{ Pa}$ (one fifth of the SAP). Under such low pressure, the splash is completely eliminated. The drop spreads on the basin fast, forms a flat thin sheet and has a shape of poached egg.

The comparison was done with an impact of a drop of diameter $d_0 = 3.6 \text{ mm}$ with an impact velocity $4 \text{ m} \cdot \text{s}^{-1}$. Physical parameters in simulations are listed in Table 5.3.

Table 5.3: Physical parameters in simulations*

	ρ_l	ρ_g	$\mu_{ethanol}$	μ_{honey}
R	$789 \text{ kg} \cdot \text{m}^{-3}$	$1 \text{ kg} \cdot \text{m}^{-3}$	$2.7 \times 10^{-3} \text{ Pa} \cdot \text{s}$	$20 \text{ Pa} \cdot \text{s}$ [Meli, 2014]
Dl	1	1.267×10^{-3}	2.376×10^{-3}	0.8802
	μ_g	γ	U_0	D
R	$1.8444 \times 10^{-5} \text{ Pa} \cdot \text{s}$	$2.24 \times 10^{-2} \text{ N} \cdot \text{m}^{-1}$	$4 \text{ m} \cdot \text{s}^{-1}$	3.6 mm
Dl	1.623×10^{-6}	4.929×10^{-4}	1	1

*: R denotes real parameters, Dl denotes dimensionless parameters.

Figure 5.15 compares photographs (taken by Jian *et al.* [2014]) with snapshots obtained from our simulations with the same physical parameters given in Table 5.3. Each column shows successive stages of drop deformation. In the photographs the drop is also seen reflected by the honey basin surface.

Similar to an impact on a solid substrate, the drop ejects a thin liquid sheet immediately after impact. Then the sheet is developed to a splash, assuming a crown-like shape. Drop shapes predicted by our simulations agree well with those observed in photographs. In the simulations, a slight deformation of the honey basin is observed. The deformation is difficult to see in the photographs because of the reflection of light and the resolution of photographs.

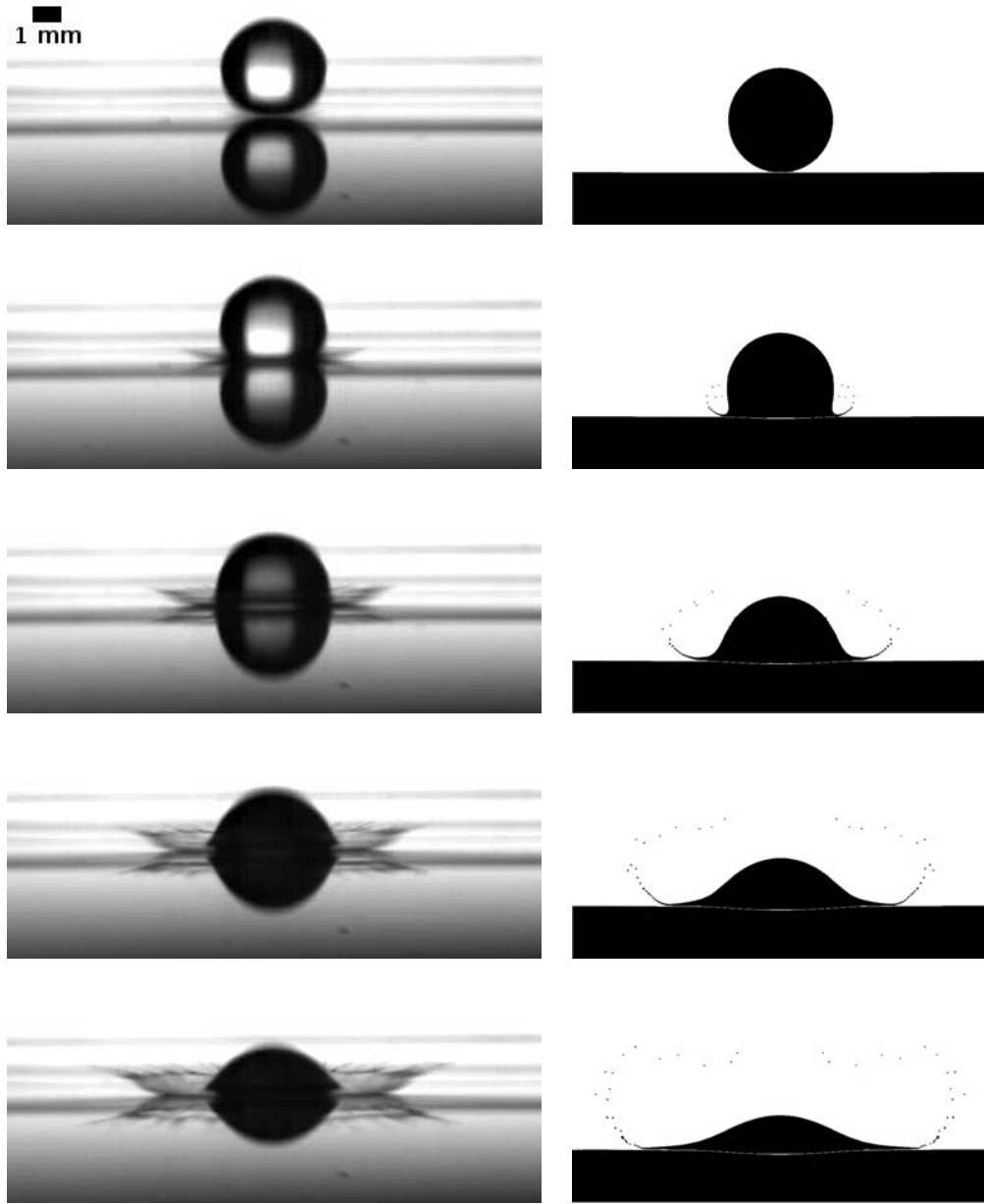


Figure 5.15: Comparison of photographs (taken by Jian *et al.* [2014]) with simulations of an ethanol drop impacting on a honey basin under the Standard Atmospheric Pressure (SAP $1.01325 \times 10^5 Pa$). The drop diameter is $d_0 = 3.6 \text{ mm}$ and the impact velocity is $4 \text{ m} \cdot \text{s}^{-1}$. The black bar in the first photograph is the length scale of 1 mm . The time interval between frames is 0.1 ms .

5.4 Conclusion

In this chapter, a theoretical model is proposed to deal with the three-phase impacting dynamics, of which a droplet of normal liquid impacts on a highly viscous liquid basin. Viscous effect is dominant as compared to the inertial and surface tension effects during the dynamics. The viscosity of the system is defined as $\mu(c_1, c_2) = c_1 c_2 \mu_{l2} + c_1 (1 - c_2) \mu_{l1} + (1 - c_1) \mu_g$ and a liquid viscosity ratio is introduced to measure the viscosity deviation from a normal liquid $m_l = \mu_{basin} / \mu_{droplet, normal}$. By increasing m_l , two regimes are identified: a wave-like regime, where the jet is eliminated and a wave-like interface is formed; a solidification regime, where the jet is formed again, the interface of the basin remains at the initial position and performs as a solid substrate. For highly-viscous liquid ($m_l > 5000$), a jet-splash is observed. With the enhanced gas layer, the jet-splash mechanism for the impact on solid is verified.

For the first time in the literature, we executed experiments of the drop impacting on a highly-viscous liquid (honey). The honey basin performed as a solid and the complete suppression of the splash was also observed by decreasing the gas pressure as reported for impacts on solid by Xu *et al.* [2005]. Comparison between photographs of experiments with snapshots of numerical simulations shows that drop shapes predicted by our model agree well with the experiments.

Conclusion and perspectives

Conclusion

Drop impact phenomenon is involved in a large number of processes in nature and in industry. When a drop impacts on a solid surface, dynamics produced by such tiny a droplet is rich and complicated. Under certain conditions, a crown-shape splash is formed. This dynamics has attracted the attention of researchers since more than a century, but there is still no crystal clear understanding of the splashing mechanism. Because of the large density and viscosity ratio between liquid and gas, gas has been generally neglected in the splashing mechanism. However, the experiments of Xu *et al.* [2005] demonstrated recently the crucial role of the gas in the splashing mechanism.

Motivated by these striking results, numerical and theoretical investigations were executed in this thesis in order to understand the gas effect in the splashing mechanism.

As observed in our simulations, the impact dynamics can be varied by changing the gas density or viscosity, transition frontiers between different outcomes in function of the density and viscosity ratio between gas and liquid are found. Two different mechanisms of splashing are identified. With a large density or viscosity ratio, a small jet is ejected before contact with the substrate and a “jet-splash” is formed; with a small density or viscosity ratio, the drop first contacts the substrate and ejects a thin liquid sheet, then the thin liquid sheet is detached and a “detachment-splash” is formed. Both gas inertial and viscous effect are crucial in the splashing formation.

A detailed study has been done on the dynamics before and after the drop contacts with the substrate. Dynamics in the gas layer before contact can be described by the lubrication approximation, but a modification with the gas inertial effect is necessary to

explain the splashing formation. We demonstrate that for both two splash mechanisms, the central entrapped bubble is probably not related to the splashing, the creation and the lift-up of the ejecta (the small jet for a jet-splash and the thin liquid sheet for a detachment-splash) is the origin of the splash and an aerodynamic force makes the lift-up occur. The variation of the aerodynamic force causes the gas entrainment in front of the contact line and produces a series of small bubbles (local contacts). With our discussion, gas compressibility effect should not be crucial in the splashing mechanism and all our studies are under the incompressible assumption. Besides, the value of the contact angle can influence the impact outcome, a hydrophilic contact angle can eliminate the splash while a hydrophobic contact angle can promote the splash.

Finally, the drop impact on a highly-viscous liquid was investigated. The viscous effect is dominant in the process, a theoretical model is proposed to deal with the dynamics with two different liquid phases. By increasing the viscosity of the liquid basin from the value of the drop to 10000 times more viscous than the drop, first the splash is suppressed and a wave-like interface is formed (the wave-like regime), then the splash appears again and the liquid basin performs more and more like a solid (the solidification regime). The experiments of an ethanol drop impacting on a highly-viscous liquid (honey) basin were executed. The honey basin performed as a solid and we observed the complete suppression of the splash by decreasing the gas pressure as reported for impacts on solid by Xu *et al.* [2005]. Drop shapes predicted by our simulations agree well with the experiments.

Perspectives

We wish that the contributions of this thesis are useful to understand the drop impact dynamics. Moreover, the following are ideas and suggestions for further investigations based on the current work.

- The current work fixes the Reynolds number and the Weber number and finds the transition frontiers in function of the gas density and viscosity. The transition frontier reported in the literature is generally for liquid properties in function of the Reynolds number and the Weber number as reviewed in the paper of Rein and Delplanque [2008]. One possibility is that we still keep the liquid and solid properties but vary the impact velocity to get a more general splashing mechanism.

- The dynamic contact angle effect in the drop impact. In this thesis, we have investigated the contact angle effect, but the dynamic contact angle is not considered. The study on the moving contact line would be useful to further understand the splashing process.
- Extension of the current work to three dimensions. Figure CP.1 shows snapshots of a drop impacting on solid in three dimensions. A splash is observed.

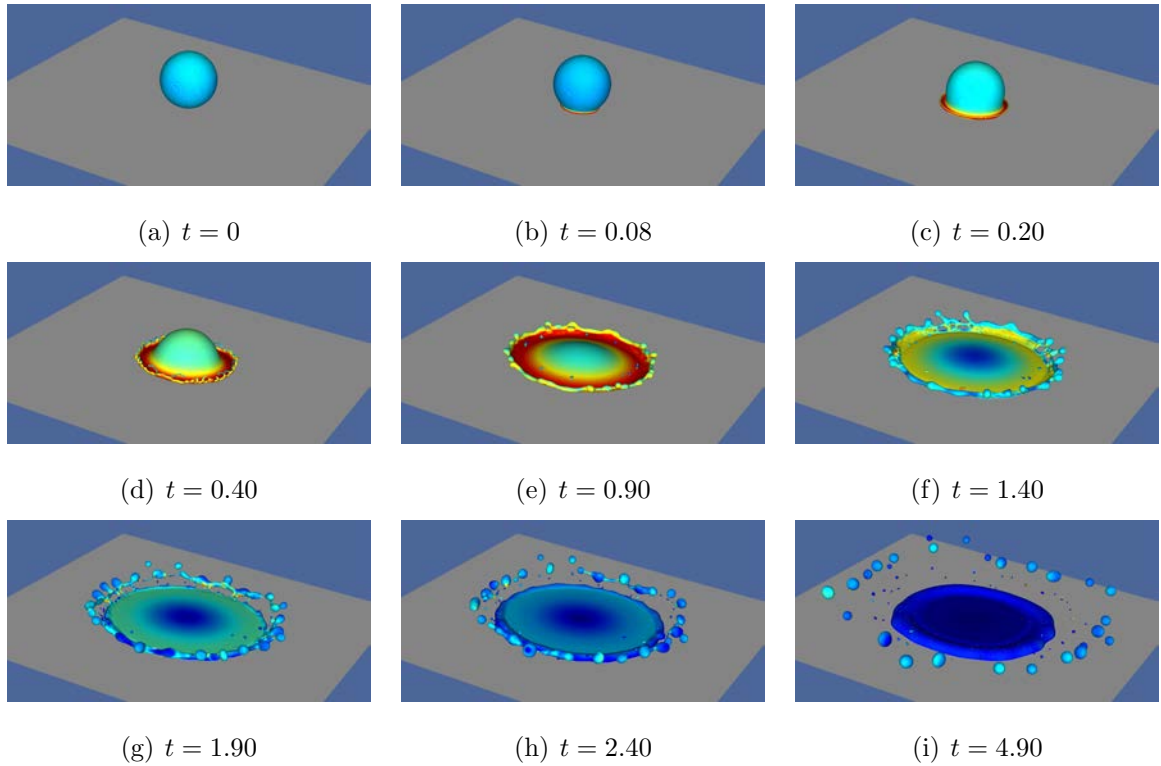


Figure CP.1: Snapshots of a drop impacting on solid in three dimensions. The initial height of the drop is $h = 0.1$ and the initial velocity is $U_0 = 1$. With absence of gas, the drop contacts the substrate at $t_{th} = 0.1$, the time is rescaled by $t = t - t_{th}$. A splash is observed. Colour gradient represents the magnitude of the velocity.

- The three-phase model for the impact on a highly-viscous liquid does not involve the variation of the surface tension and of the density between different liquids. A model involving these two factors especially the surface tension would be appreciated.

Appendix

Example of the GERRIS parameter file

In this section, we present an exemple of the GERRIS parameter file for the simulation of the drop impact on a solid substrate in Chapter §3. GERRIS has a predefined language to write the parameter file. Users do not need to master the numerical schemes to launch simulations. The parameter file is the interface between users and the numerical method.

To execute the simulation, first create a file of the format “gfs” (for instance, impact.gfs) and copy the code here in it; then launch the command “gerris2D impact.gfs | gfsview2D 0movie.gfv” in a terminal. “**GfsView**” is a visualization tool integrated in GERRIS to realise the on-the-fly or post-simulation visualization. The file “0movie.gfv” is a parameter file for the visualization configuration in “**GfsView**”. It can be easily created by “**GfsView**”.

```
1 0 GfsAxi GfsBox GfsGEdge { x = -0.5 y = 0.5 } {  
  
# Physical variables  
Global{  
/* refinement level*/  
#define LEVEL 11  
#define VAR(T,min,max) ((min + CLAMP(T,0,1))*(max - min))  
/* density ratio*/  
#define r 0.001  
/* liquid density*/  
#define Rhol 1.  
/* density*/  
#define RHO(T) VAR(T, Rhol, r*Rhol)
```

```
/* viscosity ratio*/
#define m 0.1
/* liquid viscosity*/
#define Mul 1.e-3
/* surface tension*/
#define Sigma 2.7e-3
/* initial velocity*/
#define U0 1.
/* diameter of drop*/
#define Dia 1.
/* position of drop center*/
#define Height (-0.1*Dia-0.5*Dia)
/* size of calculation domain*/
#define Length 2.
}

# Simulation time
Time { end = 1.}

# Calculation domain
PhysicalParams { L = Length }

# VOF tracer
VariableTracerVOF T
VariableFiltered T1 T 1
VariableCurvature K T

# Coordinates of the interface
VariablePosition PX T x
VariablePosition PY T y

# Drop initial position
RefineSurface 10 (ellipse(Height,0,0.5*Dia,0.5*Dia))
InitFraction T (ellipse(Height,0,0.5*Dia,0.5*Dia))

# Initial Velocity field
Init {} { U = (T < 1 ? U0:0) }

# Surface tension
```

```

SourceTension T Sigma K

# Viscosity
SourceViscosity 1./VAR(T1, 1./Mul, 1./(Mul*m)) { beta = 1 tolerance = 1e-3
}

# Density
PhysicalParams { alpha = 1./RHO(T1) }

### Mesh adaptation criteria
# Gradient
AdaptGradient { istep = 1 } { cmax = 0.01 maxlevel = LEVEL minlevel = (x >
-0.05 ? (LEVEL-2):0) } T
# Vorticity
AdaptVorticity { istep = 1 } { cmax = 0.05 maxlevel = LEVEL minlevel = (x
> -0.05 ? (LEVEL-2):0) }
# Interface curvature
AdaptFunction { istep = 1 } { cmax = 0.05 maxlevel = LEVEL minlevel = (x >
-0.05 ? (LEVEL-2):0) } (T > 0 && T < 1 ? fabs(K)*dL : 0)

# Parallel computation setup
#   EventBalance { istep = 100 } 0.1
#   OutputBalance { istep = 100 } stderr
#   OutputBalance { istep = 100 } Output.txt

### On-the-fly display
OutputTime { istep = 10 } stderr
OutputProjectionStats { istep = 10 } stderr
OutputDiffusionStats { istep = 10 } stderr
OutputSimulation { istep = 1 } stdout

OutputTime { istep = 10 } Output.txt
OutputProjectionStats { istep = 10 } Output.txt
OutputDiffusionStats { istep = 10 } Output.txt

### Save results
OutputSimulation { start = 0 step = 0.01 end = 0.07 } sim-%5.3f.gfs
OutputSimulation { start = 0 step = 0.01 end = 0.07 } Rv-%5.3f.txt {
    variables =T,PX,PY,U,V,P binary = 0 format = text }

```

```

OutputSimulation { start = 0.07 step = 0.001 end = 0.2 } sim-%5.3f.gfs
OutputSimulation { start = 0.07 step = 0.001 end = 0.2 } Rv-%5.3f.txt {
    variables =T,PX,PY,U,V,P binary = 0 format = text }

OutputSimulation { start = 0.2 step = 0.01 end = 0.5 } sim-%5.3f.gfs
OutputSimulation { start = 0.2 step = 0.01 end = 0.5 } Rv-%5.3f.txt {
    variables =T,PX,PY,U,V,P binary = 0 format = text }

OutputSimulation { start = 0.5 step = 0.1 } sim-%5.3f.gfs
OutputSimulation { start = 0.5 step = 0.1 } Rv-%5.3f.txt { variables
    =T,PX,PY,U,V,P binary = 0 format = text }

OutputSimulation { start = end } sim-%5.3f.gfs
OutputSimulation { start = end } Rv-%5.3f.txt { variables =T,PX,PY,U,V,P
    binary = 0 format = text }

### On-the-fly Data treatment
#
OutputScalarStats { start = 0 step = 0.001 } DPmaxS { v = P condition =
    (T < 1) }
OutputScalarStats { start = 0 step = 0.001 } DVmaxS { v = sqrt(U*U+V*V)
    condition = (T < 1) }
OutputScalarStats { start = 0 step = 0.001 } DHminS { v = fabs(PX)
    condition = (T > 0 && T < 1) }
OutputScalarStats { start = 0 step = 0.001 } DYmaxS { v = fabs(PY)
    condition = (T > 0 && T < 1) }
OutputScalarStats { start = 0 step = 0.001 } DXmaxS { v = PX condition =
    (T > 0 && T < 1) }
#
OutputScalarMaxima { start = 0 step = 0.001 } DPmaxM1 { v = P condition =
    (T < 1) } 1
OutputScalarMaxima { start = 0 step = 0.001 } DVmaxM1 { v = sqrt(U*U+V*V)
    condition = (T < 1) } 1
OutputScalarMaxima { start = 0 step = 0.001 } DHminM1 { v = fabs(PX)
    condition = (T > 0 && T < 1) } 1
OutputScalarMaxima { start = 0 step = 0.001 } DYmaxM1 { v = fabs(PY)
    condition = (T > 0 && T < 1) } 1

```

```
OutputScalarMaxima { start = 0 step = 0.001 } DXmaxM1 { v = PX condition
    = (T > 0 && T < 1) } 1

### Movie maker
GModule gfsview
OutputView { start = 0 step = 5e-3 } { ppm2mpeg > DShape.mpg } 0movie.gfv
}

#Boundary conditions
GfsBox {
    right = Boundary {
        BcDirichlet V 0
        BcNeumann T 0
    }
    bottom = Boundary
}
```


Bibliography

- Agbaglah, G. G. (2011). *Dynamique et instabilité des nappes liquides*. Ph.D. thesis, Univ. Paris 6.
- Alexander, F. J. and Garcia, A. L. (1997). The direct simulation monte carlo method. *Computers in Physics*, **11**(6), 588–593.
- Almgren, A. S., Bell, J. B., and Crutchfield, W. Y. (2000). Approximate projection methods: Part i. inviscid analysis. *SIAM Journal on Scientific Computing*, **22**(4), 1139–1159.
- Aulisa, E., Manservigi, S., Scardovelli, R., and Zaleski, S. (2007). Interface reconstruction with least-squares fit and split advection in three-dimensional cartesian geometry. *Journal of Computational Physics*, **225**(2), 2301–2319.
- Basaran, O. A., Gao, H., and Bhat, P. P. (2013). Nonstandard Inkjets. In Davis, SH and Moin, P, editor, *Annual Review of Fluid Mechanics, VOL 45*, volume 45 of *Annual Review of Fluid Mechanics*, pages 85–113. Annual Reviews, 4139 El Camino Way, Po Box 10139, Palo Alto, Ca 94303-0897 Usa.
- Bell, J. B., Colella, P., and Glaz, H. M. (1989). A second-order projection method for the incompressible navier-stokes equations. *Journal of Computational Physics*, **85**(2), 257–283.
- Blanchard, D. and Woodcock, A. (1957). Bubble formation and modification in the sea and its meteorological significance. *TELLUS*, **9**(2), 145–158.

- Brackbill, J., Kothe, D. B., and Zemach, C. (1992). A continuum method for modeling surface tension. *J. Comput. Phys.*, **100**, 335–354.
- Brennen, C. (2005). *Fundamentals of Multiphase Flow*. Cambridge University Press.
- Chen, S.-J. and Tseng, A. A. (1992). Spray and jet cooling in steel rolling. *International Journal of Heat and Fluid Flow*, **13**(4), 358 – 369.
- Chern, I.-L., Glimm, J., McBryan, O., Plohr, B., and Yaniv, S. (1986). Front tracking for gas dynamics. *Journal of Computational Physics*, **62**(1), 83–110.
- Chorin, A. J. (1969). On the convergence of discrete approximations to the navier-stokes equations. *Mathematics of Computation*, **23**(106), 341–353.
- Coantic, M. (1980). Mass transfert across the ocean-air interface : small scale hydrodynamic and aerodynamic mechanisms. *PhysicoChemical Hydrodynamics*, **1**, 249–279.
- Coantic, M. (1986). A model of gas transfer across air-water interfaces with capillary waves. *Journal of Geophysical Research: Oceans*, **91**(C3), 3925–3943.
- Courant, R., Friedrichs, K., and Lewy, H. (1928). Über die partiellen differenzengleichungen der mathematischen physik. *Mathematische Annalen*, **100**(1), 32–74.
- Courant, R., Friedrichs, K., and Lewy, H. (1967). On the partial difference equations of mathematical physics. *IBM journal of Research and Development*, **11**(2), 215–234.
- Crank, J. and Nicolson, P. (1947). A practical method for numerical evaluation of solutions of partial differential equations of the heat-conduction type. In *Mathematical Proceedings of the Cambridge Philosophical Society*, volume 43, pages 50–67. Cambridge Univ Press.
- De Gennes, P. G., Brochard-Wyart, F., and Quéré, D. (2005). *Gouttes, bulles, perles et ondes*. Belin.
- Deegan, R. D., Brunet, P., and Eggers, J. (2008). Complexities of splashing. *Nonlinearity*, **21**(1), C1–C11.
- Driscoll, M. M. and Nagel, S. R. (2011). Ultrafast Interference Imaging of Air in Splashing Dynamics. *Physical Review Letters*, **107**(15).

- Driscoll, M. M., Stevens, C. S., and Nagel, S. R. (2010). Thin film formation during splashing of viscous liquids. *Physical Review E*, **82**(3, 2).
- Duchemin, L. and Josserand, C. (2011). Curvature singularity and film-skating during drop impact. *Physics Of Fluids*, **23**(9).
- Duchemin, L. and Josserand, C. (2012). Rarefied gas correction for the bubble entrapment singularity in drop impacts. *Comptes Rendus Mecanique*, **340**(11-12), 797–803.
- Edgerton, H. (1999). *Exploring the Art and Science of Stopping Time*. MIT Press, Cambridge.
- Esmailizadeh, L. and Mesler, R. (1986). Bubble entrainment with drops. *Journal of Colloid and Interface Science*, **110**(2), 561 – 574.
- Ferziger, J. and Perić, M. (2002). *Computational Methods for Fluid Dynamics*. Springer London, Limited.
- Francois, M. M., Cummins, S. J., Dendy, E. D., Kothe, D. B., Sicilian, J. M., and Williams, M. W. (2006). A balanced-force algorithm for continuous and sharp interfacial surface tension models within a volume tracking framework. *Journal of Computational Physics*, **213**(1), 141–173.
- Frene, J., Nicolas, D., Degueurce, B., Berthe, D., and Godet, M. (1997). *Hydrodynamic Lubrication: Bearings and Thrust Bearings*. Elsevier.
- Granier, B., Lerat, A., and Wu, Z. (1996). An implicit centered scheme for steady and unsteady incompressible one and two-phase flows. *Comput. Fluide*.
- Grétar Tryggvason, R. S. and Zaleski, S. (2011). *Direct Numerical Simulations of Gas-Liquid Multiphase Flows*. Cambridge University Press.
- Gueyffier, D., Li, J., Nadim, A., Scardovelli, R., and Zaleski, S. (1999). Volume-of-fluid interface tracking with smoothed surface stress methods for three-dimensional flows. *Journal of Computational Physics*, **152**(2), 423–456.
- Hackbusch, W. (2003). *Multi-Grid Methods and Applications*. Springer Series in Computational Mathematics. Springer.

- Haile, J. M. (1997). *Molecular Dynamics Simulation: Elementary Methods*. A Wiley-Interscience publication. Wiley.
- Harvie, D. J., Davidson, M., and Rudman, M. (2006). An analysis of parasitic current generation in volume of fluid simulations. *Applied mathematical modelling*, **30**(10), 1056–1066.
- Heinzl, J. and Hertz, C. (1985). Ink-jet printing. *Adv Electronics Electron Physics*, **65**, 91 – 166.
- Hicks, P. and Purvis, R. (2010). Air cushioning and bubble entrapment in three-dimensional droplet impacts. *J. Fluid Mech.*, **649**, 135–163.
- Hirt, C. W. and Nichols, B. D. (1981). Volume of fluid (vof) method for the dynamics of free boundaries. *Journal of computational physics*, **39**(1), 201–225.
- Ho, C. C., Murata, K., Steingart, D. A., Evans, J. W., and Wright, P. K. (2009). A super ink jet printed zinc-silver 3D microbattery. *Journal Of Micromechanics And Microengineering*, **19**(9). 8th International Workshop on Micro and Nanotechnology for Power Generation and Energy Conversion Applications, Tohoku Univ, Sendai, JAPAN, NOV 09-12, 2008.
- Howison, S., Ockendon, J., Oliver, J., Purvis, R., and Smith, F. (2005). Droplet impact on a thin fluid layer. *J. Fluid. Mech.*, **542**, 1–23.
- Jennings, S. (1988). The mean free path in air. *Journal of Aerosol Science*, **19**(2), 159 – 166.
- Jian, Z., Michon, G.-J., Josserand, C., Zaleski, S., and Ray, P. (2014). Numerical and experimental investigation of droplet impact on a highly viscous liquid basin. In *23rd International Conference on Discrete Simulation of Fluid Dynamics (DSFD)*, July 28th – August 1st, 2014, Paris, France.
- Josserand, C. and Zaleski, S. (2003). Droplet splashing on a thin liquid film. *Phys. Fluids*, **15**, 1650–1657.
- Kamphoefner, F. (1972). Ink jet printing. *Electron Devices, IEEE Transactions on*, **19**(4), 584–593.

- Kolev, N. (2002). *Multiphase Flow Dynamics 1: Fundamentals*. Engineering Online Library. Springer-Verlag GmbH.
- Kolinski, J. M., Rubinstein, S. M., Mandre, S., Brenner, M. P., Weitz, D. A., and Mahadevan, L. (2012). Skating on a film of air: Drops impacting on a surface. *Phys. Rev. Lett.*, **108**, 074503.
- Lafaurie, B., Nardone, C., Scardovelli, R., Zaleski, S., and Zanetti, G. (1994). Modelling merging and fragmentation in multiphase flows with SURFER. *J. Comput. Phys.*, **113**, 134–147.
- Lampe, J., DiLalla, R., Grimaldi, J., and Rothstein, J. P. (2005). Impact dynamics of drops on thin films of viscoelastic wormlike micelle solutions. *Journal of non-newtonian fluid mechanics*, **125**(1), 11–23.
- Le, H. (1998). Progress and trends in ink-jet printing technology. *Journal Of Imaging Science And Technology*, **42**(1), 49–62.
- Lesser, M. and Field, J. (1983). The impact of compressible liquids. *Annu. Rev. Fluid Mech.*, **15**, 97.
- Li, J. (1995). Calcul d’interface affine par morceaux (piecewise linear interface calculation). *C. R. Acad. Sci. Paris, série IIb, (Paris)*, **320**, 391–396.
- Mandre, S. and Brenner, M. P. (2012). The mechanism of a splash on a dry solid surface. *Journal Of Fluid Mechanics*, **690**, 148–172.
- Mandre, S., Mani, M., and Brenner, M. (2009). Precursors to splashing of liquid droplets on a solid surface. *Phys. Rev. Lett.*, **102**, 134502.
- Marengo, M., Antonini, C., Roisman, I. V., and Tropea, C. (2011). Drop collisions with simple and complex surfaces. *Current Opinion in Colloid & Interface Science*, **16**(4), 292 – 302.
- Mehdi-Nejad, V., Mostaghimi, J., and Chandra, S. (2003). Air bubble entrapment under an impacting droplet. *Phys. Fluids*, **15**(1), 173–183.

- Meli (2014). Product specifications - honey of acacia. http://www.meli.be/Portals/0/productfiches/Honing%20Acacia%20EN%2030-07-12%20_A4.pdf. www.meli.be.
- Michon, G.-J. (2012). Unpublished experimental results. Institute Jean Le Rond d'Alembert, Univ. Pierre and Marie Curie, Paris, France.
- Mohamad, A. (2011). *Lattice Boltzmann Method: Fundamentals and Engineering Applications with Computer Codes*. SpringerLink : Bücher. Springer.
- Muller, E., Heide, K., and Zanutto, E. (1993). Molecular structure and nucleation in silicate glasses. *Journal of Non-Crystalline Solids*, **155**(1), 56 – 66.
- Nakamura, M., Nishiyama, Y., Henmi, C., Iwanaga, S., Nakagawa, H., Yamaguchi, K., Akita, K., Mochizuki, S., and Takiura, K. (2008). Ink Jet Three-Dimensional Digital Fabrication for Biological Tissue Manufacturing: Analysis of Alginate Microgel Beads Produced by Ink Jet Droplets for Three Dimensional Tissue Fabrication. *Journal Of Imaging Science And Technology*, **52**(6).
- Oroian, M. (2013). Measurement, prediction and correlation of density, viscosity, surface tension and ultrasonic velocity of different honey types at different temperatures. *Journal of Food Engineering*, **119**(1), 167 – 172.
- Osher, S. and Fedkiw, R. P. (2001). Level set methods: An overview and some recent results. *Journal of Computational Physics*, **169**(2), 463 – 502.
- Osher, S. and Sethian, J. A. (1988). Fronts propagating with curvature-dependent speed: algorithms based on hamilton-jacobi formulations. *Journal of computational physics*, **79**(1), 12–49.
- Palacios, J., Hernández, J., Gómez, P., Zanzi, C., and López, J. (2012). On the impact of viscous drops onto dry smooth surfaces. *Experiments in Fluids*, **52**(6), 1449–1463.
- Palacios, J., Hernández, J., Gómez, P., Zanzi, C., and López, J. (2013). Experimental study of splashing patterns and the splashing/deposition threshold in drop impacts onto dry smooth solid surfaces. *Experimental Thermal and Fluid Science*, **44**(0), 571 – 582.

- Photron (2012). Fastcam sa5. http://www.photron.com/datasheet/FASTCAM_SA5.pdf.
<http://www.photron.com>.
- Popinet, S. (2003). Gerris: a tree-based adaptive solver for the incompressible euler equations in complex geometries. *Journal of Computational Physics*, **190**(2), 572–600.
- Popinet, S. (2009). An accurate adaptive solver for surface-tension-driven interfacial flows. *Journal of Computational Physics*, **228**(16), 5838–5866.
- Popinet, S. and Zaleski, S. (1999). A front tracking algorithm for the accurate representation of surface tension. *Int. J. Numer. Meth. Fluids*, **30**, 775–793.
- Pp, S., Gupta, S., and Foster, G. (1995). Raindrop-induced soil detachment and sediment transport from interrill areas. *Soil Science Society Of America Journal*, **59**(3), 727–734.
- Rehman, S., Khan, Z. F., and Maqbool, T. (2008). Physical and spectroscopic characterization of pakistani honey. *Ciencia e Investigación Agraria*, **35**(2), 199–204.
- Rein, M. (1993). Phenomena of liquid drop impact on solid and liquid surfaces. *Fluid Dyn. Res.*, **12**, 61.
- Rein, M. and Delplanque, J.-P. (2008). The role of air entrainment on the outcome of drop impact on a solid surface. *Acta Mechanica*, **201**(1-4), 105–118.
- Renardy, Y. and Renardy, M. (2002). Prost: a parabolic reconstruction of surface tension for the volume-of-fluid method. *Journal of Computational Physics*, **183**(2), 400–421.
- Rioboo, R., Marengo, M., and Tropea, C. (2001). Outcomes from a drop impact on solid surfaces. *Atomization and Sprays*, **11**, 155–165.
- Rubinstein, S., Cohen, G., and Fineberg, J. (2004). Detachment fronts and the onset of dynamic friction. *Nature*, **430**(7003), 1005–1009.
- Scardovelli, R. and Zaleski, S. (2003). Interface reconstruction with least-square fit and split eulerian–lagrangian advection. *International Journal for Numerical Methods in Fluids*, **41**(3), 251–274.
- Schroll, R. D., Josserand, C., Zaleski, S., and Zhang, W. W. (2010). Impact of a Viscous Liquid Drop. *Physical Review Letters*, **104**(3).

- Schwarz, G. (1995). *The hodge decomposition*. Springer.
- Shyy, W., Udaykumar, H., Rao, M. M., and Smith, R. W. (1996). *Computational fluid dynamics with moving boundaries*. Taylor and Francis, London.
- Sirringhaus, H., Kawase, T., Friend, R., Shimoda, T., Inbasekaran, M., Wu, W., and Woo, E. (2000). High-resolution inkjet printing of all-polymer transistor circuits. *Science*, **290**(5499), 2123–2126.
- Smith, F., Li, L., and Wu, G. (2003). Air cushioning with a lubrication/inviscid balance. *Journal Of Fluid Mechanics*, **482**, 291–318.
- Smith, G. D. (1985). *Numerical Solution of Partial Differential Equations: Finite Difference Methods*. Oxford University Press.
- Tao, W. (2000). *Advances in Computational Heat Transfer (in Chinese)*. Science Press, China.
- Tao, W. (2001). *Numerical Heat Transfer (Second Edition) (in Chinese)*. Xi'an Jiaotong University Press CO. LTD.
- Thoroddsen, S. (2002). The ejecta sheet generated by the impact of a drop. *J. Fluid Mech.*, **451**, 373.
- Thoroddsen, S., Etoh, T., and Takehara, K. (2008). High-speed imaging of drops and bubbles. *Ann. Rev. Fluid Mech.*, **40**, 257–285.
- Thoroddsen, S. T., Etoh, T. G., and Takehara, K. (2003). Air entrapment under an impacting drop. *Journal of Fluid Mechanics*, **478**, 125–134.
- Thoroddsen, S. T., Etoh, T. G., Takehara, K., Ootsuka, N., and Hatsuki, A. (2005). The air bubble entrapped under a drop impacting on a solid surface. *Journal of Fluid Mechanics*, **545**, 203–212.
- Thoroddsen, S. T., Takehara, K., and Etoh, T. G. (2009). Dewetting at the center of a drop impact. *Modern Physics Letters B*, **23**(3), 361–364. 2nd International Symposium On Physics Of Fluids, Jiuzhaigou, Peoples R China, Jun 09-12, 2008.

- Tryggvason, G., Bunner, B., Esmaeeli, A., Juric, D., Al-Rawahi, N., Tauber, W., Han, J., Nas, S., and Jan, Y.-J. (2001). A front-tracking method for the computations of multiphase flow. *Journal of Computational Physics*, **169**(2), 708–759.
- Versteeg, H. K. and Malalasekera, W. (2007). *An Introduction to Computational Fluid Dynamics: The Finite Volume Method*. Pearson Education.
- Watkins, D. (2007). *The Matrix Eigenvalue Problem: GR and Krylov Subspace Methods*. Other titles in applied mathematics. Society for Industrial and Applied Mathematics.
- Weiss, D. and Yarin, A. (1999). Single drop impact onto liquid films: neck distortion, jetting, tiny bubble entrainment, and crown formation. *J. Fluid Mech.*, **385**, 229–254.
- Worthington, A. (1908). *A Study of Splashes*. London, New York, Bombay, Calcutta : Longmans, Green, and Co.
- Worthington, A. M. (1876a). On the forms assumed by drops of liquids falling vertically on a horizontal plate. *Proceedings of the Royal Society of London*, **25**(171-178), 261–272.
- Worthington, A. M. (1876b). A second paper on the forms assumed by drops of liquids falling vertically on a horizontal plate. *Proceedings of the Royal Society of London*, **25**(171-178), 498–503.
- Worthington, A. M. (1881). On pendent drops. *Proceedings of the Royal Society of London*, **32**(212-215), 362–377.
- Worthington, A. M. (1882). On impact with a liquid surface. *Proceedings of the Royal Society of London*, **34**(220-223), 217–230.
- Worthington, A. M. and Cole, R. S. (1899). Impact with a liquid surface, studied by the aid of instantaneous photography. paper ii. *Proceedings of the Royal Society of London*, **65**(413-422), 153–154.
- Xu, L., Zhang, W., and Nagel, S. (2005). Drop splashing on a dry smooth surface. *Phys. Rev. Lett.*, **94**, 184505.
- Yarin, A. L. (2006). Drop impact dynamics: Splashing, spreading, receding, bouncing... *Annu. Rev. Fluid Mech.*, **38**, 159.

- Zhao, F., Lai, M.-C., and Harrington, D. (1999). Automotive spark-ignited direct-injection gasoline engines. *Progress in Energy and Combustion Science*, **25**(5), 437 – 562.
- Zienkiewicz, O. C., Taylor, R. L., and Zhu, J. (2005). *The Finite Element Method: Its Basis and Fundamentals: Its Basis and Fundamentals*. Butterworth-Heinemann.